Lawrence Berkeley National Laboratory
LBL Publications

Title

X-Ray Absorption Spectroscopy on the Calcium Cofactor to the Manganese Cluster in Photosynthetic Oxygen Evolution

Permalink

https://escholarship.org/uc/item/36z3v852

Author

Cinco, Roehl M, Ph.D. Thesis

Publication Date

1999-12-01

Copyright Information

This work is made available under the terms of a Creative Commons Attribution License, available at https://creativecommons.org/licenses/by/4.0/

eScholarship.org Powered by the California Digital Library
University of California

LBNL-44753

ERNEST ORLANDO LAWRENCE
BERKELEY NATIONAL LABORATORY

X-Ray Absorption Spectroscopy on the Calcium Cofactor to the Manganese Cluster in Photosynthetic Oxygen Evolution

Roehl M. Cinco

Physical Biosciences Division

December 1999

Ph.D. Thesis

REFERENCE COPY
Does Not
Circulate
Copy 1
Bldg. 50 Library - Ref.
Lawrence Berkeley National Laboratory

DISCLAIMER

This document was prepared as an account of work sponsored by the United States Government. While this document is believed to contain correct information, neither the United States Government nor any agency thereof, nor the Regents of the University of California, nor any of their employees, makes any warranty, express or implied, or assumes any legal responsibility for the accuracy, completeness, or usefulness of any information, apparatus, product, or process disclosed, or represents that its use would not infringe privately owned rights. Reference herein to any specific commercial product, process, or service by its trade name, trademark, manufacturer, or otherwise, does not necessarily constitute or imply its endorsement, recommendation, or favoring by the United States Government or any agency thereof, or the Regents of the University of California. The views and opinions of authors expressed herein do not necessarily state or reflect those of the United States Government or any agency thereof or the Regents of the University of California.

LBNL-44753

X-ray Absorption Spectroscopy on the Calcium Cofactor to the Manganese Cluster in Photosynthetic Oxygen Evolution

Roehl Marave Cinco

Ph.D. Thesis

Department of Chemistry
University of California, Berkeley
and
Physical Biosciences Division
Lawrence Berkeley National Laboratory
Berkeley, CA 94720-5230

Fall 1999

This work was supported by the Director, Office of Science, Office of Basic Energy Sciences, Division of Energy Biosciences of the U.S. Department of Energy (DOE) under Contract DE-AC03-76SF00098, and the National Institutes of Health (NIH Grant GM55302).

X-ray Absorption Spectroscopy on the Calcium Cofactor to the Manganese Cluster in Photosynthetic Oxygen Evolution

by

Roehl Marave Cinco

B.S. (University of California, Irvine) 1991

A dissertation submitted in partial satisfaction of the
requirements for the degree of

Doctor of Philosophy
in
Chemistry

in the
GRADUATE DIVISION
of the
UNIVERSITY OF CALIFORNIA, BERKELEY

Committee in charge:
Professor Kenneth Sauer, Chair
Professor Sung-Hou Kim
Professor Anastasios Melis

Fall 1999

Abstract

X-ray Absorption Spectroscopy on the Calcium Cofactor to the Manganese Cluster in Photosynthetic Oxygen Evolution

by

Roehl Marave Cinco

Doctor of Philosophy in Chemistry
University of California, Berkeley
Professor Kenneth Sauer, Chair

Along with Mn, calcium and chloride ions are necessary cofactors for oxygen evolution in Photosystem II (PS II). To further test and verify whether Ca is close to the Mn cluster, we substituted strontium for Ca and probed from the Sr point of view for any nearby Mn. The extended X-ray absorption fine structure (EXAFS) of Sr-reactivated PS II indicates major differences between the intact and NH_2OH-treated samples. In intact samples, the Fourier transform of the Sr EXAFS shows a Fourier peak that is missing in inactive samples. This peak II is best simulated by two Mn neighbors at a distance of 3.5 Å, confirming the proximity of Ca (Sr) cofactor to the Mn cluster. In addition, polarized Sr EXAFS on oriented Sr-reactivated samples shows this peak II is dichroic: large magnitude at 10° (angle between the PS II membrane normal and the x-ray electric field vector) and small at 80°. Analysis of the dichroism yields the relative angle between the Sr–Mn vector and membrane normal (23° ± 4°), and the isotropic coordination number for these layered samples.

X-ray absorption spectroscopy has also been employed to assess the degree of similarity between the manganese cluster in PS II and a family of synthetic manganese complexes containing the distorted cubane [Mn_4O_3X] core (X = benzoate, acetate, methoxide, hydroxide, azide, fluoride, chloride or bromide). In addition, Mn_4O_3Cl complexes containing three or six terminal Cl ligands at three of the Mn were included in this study. The EXAFS method detects the small changes in the core structures as X is varied in this series, and serves to exclude these distorted cubanes of C_{3v} symmetry as a topological model for the Mn catalytic cluster.

The sulfur K-edge x-ray absorption near-edge structure (XANES) spectra for the amino acids cysteine, methionine, their corresponding oxidized forms cystine and methionine sulfoxide, and glutathione show distinct differences between the thiol and disulfide forms. Sulfur XANES is also used to detect changes (within 5%) of the thiol-to-disulfide ratio in whole human blood, plasma, and erythrocytes.

X-Ray Absorption Spectroscopy on the Calcium Cofactor to the Manganese Cluster in Photosynthetic Oxygen Evolution

Copyright © 1999

by

Roehl Marave Cinco

The U.S. Department of Energy has the right to use this document
for any purpose whatsoever including the right to reproduce
all or any part thereof.

To my parents, and to my brothers Raoul and Danny

Table of Contents

Table of Contents iv
List of Figures and Tables vi
List of Abbreviations viii
Acknowledgments ix

Chapter 1 — Introductory Section 1

Chapter 2 — Strontium EXAFS Reveals the Proximity of Calcium to the Manganese Cluster of Oxygen-Evolving Photosystem II 8
- Introduction 9
- Experimental Section 14
  - Sr^{2+}-reactivated PS II Sample Preparation 14
  - Sr-PS II Sample Preparation by Removal of Excess Sr 15
  - Oxygen-Evolution Assays 15
  - EPR Spectroscopy 16
  - Metals Quantitation 16
  - EXAFS Measurements 17
  - Data Analysis 18
- Results 22
  - Oxygen-Evolving Activity Data 22
  - EPR Spectroscopy 24
  - Metals Analysis 24
  - Sr EXAFS of Intact and Inactive Sr-PS II in the S_1 State 27
  - Curve Fitting of Sr EXAFS Data 32
- Discussion 39

Chapter 3 — Orientation of the Calcium Cofactor in Oxygen Evolution Probed by Polarized Strontium EXAFS on Layered Photosystem II Membranes 45
- Introduction 46
- Experimental Section 50
  - Sample Preparation 50
  - Metals Quantitation 50
  - EPR Spectroscopy 51
  - Mosaic Spread Determination by EPR 51
  - EXAFS Data Collection 52
  - EXAFS Data Analysis 53
  - Theory of Polarized EXAFS 53
- Results 58
  - Mosaic Spread 58
  - Polarized Sr EXAFS on Oriented Samples 58

Fourier Transform (FT) of Polarized Sr EXAFS....60
EXAFS Curve Fitting....66
Determination of ϕ....72
Discussion....77
Error Analysis....77
Implications of the Polarized Sr EXAFS Results....79

Chapter 4 — Comparison of the Manganese Cluster in Oxygen-Evolving Photosystem II with Distorted Cubane Manganese Compounds through X-ray Absorption Spectroscopy....86
Introduction....87
Experimental Section....94
Sample Preparation....94
X-ray absorption spectroscopy....95
Data Analysis....95
Results....103
Mn XANES....103
Mn EXAFS....105
Discussion....125
Mn XANES Spectra....125
Mn EXAFS and FT....126

Chapter 5 — Sulfur K-edge X-ray Absorption Spectroscopy Examines the Redox State of Biologically Relevant Sulfur Compounds....132
Introduction....133
Experimental Section....137
Sample Preparation....137
Sulfur XANES Data Collection....137
Results....142
Sulfur-containing Amino Acids....142
Erythrocytes....146
Plasma....148
Whole blood....148
Discussion....152

Chapter 6 — Conclusions and Future Directions....154
The Case of the Missing Sr-altered Multiline Signal....156
Improved Mosaic Spread Determination....157
Improvements to Sulfur XAS....158
Ca EXAFS Experiments to Probe the Cofactor Directly....158
Background....158
Proposed Experiments....159
References....165
Appendices....183

List of Figures and Tables

Figure 1.1..................Experimental setup for synchrotron radiation studies..........7
Table 2.1..................O_2 Activity Data..........23
Figure 2.1..................EPR Spectra of Sr- and Ca-reactivated PS II..........26
Figure 2.2..................k^3-Weighted Sr EXAFS data of intact and inactive Sr-PS II..........29
Figure 2.3..................Fourier transforms of Sr EXAFS for intact and inactive Sr-substituted PS II..........31
Figure 2.4..................Sr EXAFS curve fitting for peak II..........34
Table 2.2..................Sr EXAFS Fitting Results for peak II..........36
Figure 2.5..................Sr EXAFS curve fitting for peak II..........38
Figure 2.6..................Proposed model for the active site of the oxygen-evolving complex..........44
Figure 3.1..................Scheme for the vectors and angles involved in x-ray absorption linear dichroism..........55
Figure 3.2..................Polar plot of calculated EXAFS amplitude (N_{app})..........57
Figure 3.3..................EPR Signal II spectrum of layered PS II to estimate mosaic spread..........59
Figure 3.4..................k^3-weighted Sr EXAFS of oriented Sr-PS II membranes..........62
Figure 3.5..................Fourier transforms of k^3-weighted EXAFS from oriented Sr-PS II..........65
Figure 3.6..................Fourier-isolated EXAFS of peak II from oriented Sr-PS II samples..........68
Table 3.1..................Oriented Sr EXAFS Fitting Results for Peak II..........69
Figure 3.7..................EXAFS curve fitting for the $\theta = 10°$ data..........71
Figure 3.8..................Simulation of Napp for Different Mosaic Spread..........73
Table 3.2..................Corrected N_{app} values for $\Omega = 15°$..........75
Figure 3.9..................Polar plot of the x-ray absorption linear dichroism from oriented Sr-PS II..........76
Figure 3.10..................Linear Plot of polarized Sr EXAFS Data..........78
Figure 3.11..................Revised working model for the Mn cluster of the OEC and its Ca cofactor..........85
Figure 4.1..................Possible core structures for the active site of the OEC in PS II..........90
Figure 4.2..................Core structures of tetranuclear Mn cubane complexes..........93
Figure 4.3..................Normalized Mn K-edge X-ray absorption near-edge structure (XANES) spectra..........100
Figure 4.4..................Second derivatives of the edge region of the samples in Fig. 4.3..........102
Table 4.1..................Mn K-Edge Rising Edge Inflection Point (Edge Position)..........104

Table 4.1S ....Minimum, Maximum, and Width of k for Forward Fourier Transforms 106
Figure 4.5..................Background-subtracted k-space EXAFS from PS II and model compounds..109
Figure 4.5S ....Raw k^3-weighted Mn EXAFS of PS II and Mn model compounds...111
Figure 4.6..................Fourier transform spectra of raw k-space Mn EXAFS from PS II and model compounds 113
Table 4.2....................Least-Squares Best Fits Of Filtered Peak I-II-(III) from Mn Cubanes 116
Figure 4.7..................Simulation of Fourier transform peaks I, II and III......... 119
Figure 4.8..................Simulation of Fourier transform peaks I, II and III......... 121
Figure 4.9..................Simulation of Fourier transform peaks I, II and III......... 124
Table 4.3....................Best Fits Of Filtered Peak II for the "O" Cubanes and PS II 131
Figure 5.1..................Normalized S K-edge X-ray absorption spectra 141
Table 5.1....................Sulfur K-edge inflection point energies............................ 143
Figure 5.2..................Normalized S K-edge X-ray absorption spectra 145
Figure 5.3..................Normalized S K-edge X-ray absorption spectra of erythrocytes 147
Figure 5.4..................Normalized S K-edge X-ray absorption spectra of blood plasma..149
Figure 5.5..................Normalized S K-edge X-ray absorption spectra of whole blood...150
Figure 5.6..................Normalized S K-edge X-ray absorption spectra of whole blood...151
Figure 6.1..................EPR Multiline signal (MLS) for Sr-reactivated PS II before and after Chelex treatment...................................163
Figure 6.2..................Calibration line relating mosaic spread to EPR Signal II ratio...164
Appendix 1 ....Light intensity dependence of oxygen activity 184
Appendix 2 ....Mn EXAFS of Isotropic and Oriented Sr-reconstituted PS II...186
Appendix 3 ....Normalized Mn K-edge XANES from three tetranuclear Mn model compounds with bipyridine ligands 188

List of Abbreviations

Chl	chlorophyll
cyt	cytochrome
EPR	electron paramagnetic resonance
EXAFS	extended x-ray absorption fine structure
FT	Fourier transform
GSH	glutathione reduced form
GSSG	glutathione oxidized form
HPCE	high-performance capillary electrophoresis
HPLC	high performance liquid chromatography
ICP-AES	inductively coupled plasma and atomic emission spectroscopy
IPE	inflection point energy
LHC II	light harvesting complex II
MLS	multi-line signal
NMR	nuclear magnetic resonance
OBz	benzoate
OEC	oxygen-evolving complex
PS II	Photosystem II
RC	reaction center
Sr-PS II	strontium-reactivated Photosystem II
SSRL	Stanford Synchrotron Radiation Laboratory
XANES	x-ray absorption near-edge structure
XAS	x-ray absorption spectroscopy

Acknowledgments

The research described in this dissertation would not have been possible without the help of many individuals, organization and agencies. All of these are now acknowledged here, not necessarily in any particular order.

My thanks go to my advisers, Professor Kenneth Sauer and Dr. Melvin Klein, whose support and encouragement have enabled me to accomplish the various research problems noted in the following chapters. Their intellectual heft, and guidance and direction have been crucial in my development as a chemist and as a scientist. Vittal Yachandra has given me day-to-day and hands-on direction and advice, and mentored me early in my career. He has spurred my growth and grasp of this research field. Thanks go to him for this patience and perseverance in dealing with me. I appreciate the efforts of my dissertation committee, Professors Anastasios Melis and Sung-Hou Kim, who, along with Ken Sauer and Mel, have read through my dissertation.

I am grateful to the Ford Foundation for a predoctoral fellowship at the start of my graduate career, and to the various agencies for funding: the Director, Office of Science, Office of Basic Energy Sciences, Division of Energy Biosciences of the U.S. Department of Energy (DOE) under Contract DE-AC03-76SF00098, and the National Institutes of Health (NIH Grant GM55302 to Vittal Yachandra). Synchrotron radiation facilities were provided by the Stanford Synchrotron Radiation Laboratory (SSRL) which is operated by the Department of Energy, Office of Basic Energy Sciences. The SSRL Biotechnology Program is supported by the National Institutes of Health, National Center of Research Resources, Biomedical Technology Program, and by the Department of Energy, Office of Health and Environmental Research.

Over the course of my time in the Calvin Laboratory, I have been privileged to work with outstanding members of the Klein and Sauer research group. I thank Matthew Latimer for getting me started on the strontium/calcium project and on x-ray absorption spectroscopy. Joy Andrews helped me get started with the orientation of PS II samples. The past members of the Klein/Sauer group, Wen Liang and Theo Roelofs, are thanked for their advice and transferred knowledge.

My co-workers for Chapter 2 included John Robblee, Annette Rompel, and Carmen Fernandez. Professor Hubert Schmidbaur and Michael Schmidt kindly provided the Sr-amino acid complexes mentioned. Dr. Matthew Latimer, Dr. Wa On Yu and Joanne Miura also helped with the data collection and sample preparation.

For Chapter 3, I thank John H. Robblee, Johannes Messinger, Henk Visser, and Carmen Fernandez for help in data collection. In Chapter 4, my thanks go to Annette Rompel for pushing this work forward, to Henk Visser, Matthew J. Latimer and John H. Robblee for help with XAS data collection, and to Professor George Christou and Guillem Aromí (Indiana University) for providing the studied Mn compounds. Co-workers involved in Chapter 5 included: Annette Rompel (the driving force behind this work), Matthew Latimer (who constructed the low-Z, liquid helium flow cryostat), Ann E. McDermott (Columbia University), R. D. Guiles (University of Maryland at Baltimore), Alexandre Quintanilha (University of Oporto, Portugal), and Dr. Ronald M. Krauss (Life Sciences Division, Lawrence Berkeley National Laboratory). Additionally, Joy Andrews, Gary Olsen, John Robblee and Henk Visser helped with XAS data collection. Dr. Diane L. Tribble and Lillie Taat (LBNL) collected the biological samples for use in XAS.

As the preceding paragraphs have shown, XAS data collection is a team effort and so I express my gratitude to the (mostly) current team of Karen McFarlane, John Robblee, Shelly Pizarro, Henk Visser, Emanuele Bellacchio, Johannes Messinger, Elodie Anxolabehere-Mallart, and Carmen Fernandez, for their energy, effort and enthusiasm, which have benefited me and have been transferred to me. The technical support personnel and staff at LBNL and SSRL also deserve recognition for their help in making the experiments listed in the forthcoming chapters practical and possible.

I express my deepest gratitude to my parents, and brothers, who have patiently provided emotional, familial and physical support and encouragement. Finally, the years at the University of California, Berkeley, have been made worthwhile by my interactions with the students, faculty and staff of the Chemistry Department and with the assorted denizens of Calvin Lab. To all of them go my sincerest thanks, respect and appreciation.

Chapter 1 — Introductory Section

Three elements that are important in biology are manganese, calcium and sulfur. of these, Mn and Ca play an especially vital role in bioinorganic chemistry in general[1,2] and photosynthesis in particular.[3,4] Sulfur is ubiquitous in proteins and serves as a ligand in catalytic centers of some metalloenzymes.[5] All three are the focus of the studies described in this dissertation: strontium, substituting for the Ca cofactor in oxygen-evolving photosynthesis, manganese in the catalytic center of water-splitting, and sulfur in redox-regulation in animals.

The key thread binding these seemingly disparate topics is the technique of x-ray absorption spectroscopy (XAS). As will be described in more detail later, XAS has many advantages for probing Sr (Ca), Mn and S in biology.[6-8] Among these is the element-specificity and ability to detect dilute concentrations. One experimental setup is shared by the four major investigations presented here, and this is presented in Figure 1.1. All data were collected at the Stanford Synchrotron Radiation Laboratory (SSRL) on beamlines VII-3 (Sr and Mn) and VI-2 (S).

The basic approach is to irradiate the sample with x-rays at the K-edge of the element, to ionize the core 1*s* electron, and then monitor the absorption spectra. Analysis of the spectra allow us to uncover structural and chemical information that would be otherwise unavailable. The radiation source in this case is the electron storage ring (called SPEAR). The beamline port provides the outlet for the synchrotron radiation produced by the circulating electrons inside the ring. After collimation by slits, the polychromatic beam enters the monochromator to select the particular energy of the K-edge x-rays for the element of interest (about 2.5 keV for S, 6.5 keV for Mn and 16.1 keV for Sr). Another slit collimates the monochromatic x-ray beam before its incident intensity is measured by a gas ionization chamber

(I_0). The sample is positioned at 45° to the irradiating x-ray beam and typically kept frozen at 10 K inside a cryostat. While the transmitted intensity (I_1) can be recorded, the more useful quantity is the x-ray fluorescence of the absorbing element (I_F) which is at a unique energy for each element. I_F is measured by a solid-state, multi-element Ge detector (for Sr and Mn) or a gas-filled Lytle detector (for S), positioned 90° to the x-ray beam. A reference transmission spectrum (using I_1 and I_2) of a known compound such as $KMnO_4$ or $SrCO_3$ serves as an internal energy calibration. Normally, fluorescence excitation spectra are obtained by scanning the K-edge region (and beyond) with the monochromator while monitoring the fluorescence. Here, the absorbance is obtained by normalizing the observed fluorescence (I_F) by the incident intensity (I_0). The x-ray absorption near-edge structure (XANES) or the region within 50 eV of the K-edge holds information about the oxidation state of the element, while the extended x-ray absorption fine structure (EXAFS) stretches up to several hundred eV above the K-edge. The extended region provides structural information: distances, identities, and numbers of scattering neighbors to the absorber.

The common technique of XAS is applied in the following sections to various problems in biology. In Chapter 2, the important cofactor calcium is substituted with strontium so that Sr EXAFS studies can performed on Photosystem II (PS II). This is because the higher atomic number of Sr, makes it a better scatterer and more "visible" to x-rays. At the time of this experiment, Ca EXAFS was not practical and was fraught with difficulties, leaving Sr EXAFS as the obvious approach. Therefore, the study indirectly addresses the calcium cofactor's binding site through substitution with strontium. Sr EXAFS confirms the proximity of Sr, and therefore Ca, to the

Mn cluster (within 3.5 Å), and show that together, these metals form a Mn–Ca heteronuclear cluster as the active site of oxygen evolution.

Chapter 3 goes a step further by applying polarized Sr EXAFS to layered (partially ordered), Sr-substituted PS II membranes. From the orientation dependence (dichroism) of the Sr EXAFS, we determine the relative angle between the just-confirmed Sr–Mn vector and the membrane normal. This angular information allows us to refine the model for the Mn–Ca heteronuclear cluster.

Chapter 4 addresses the entity to which the Ca cofactor is linked: the Mn cluster itself. Although Mn XAS has helped to formulate model for this catalytic site, other alternative structures have been proposed. We compare one alternative class, of distorted cubane Mn model compounds, to the native cluster in PS II by means of Mn XAS. Major differences between the XANES and EXAFS from each case are found. Enough contrast exists to exclude the distorted cubane as a possible structure for the Mn cluster of the oxygen-evolving complex.

The subject of Chapter 5 deals with sulfur XAS as a tool to probe the redox state of important biological molecules: the amino acids cysteine and methionine, along with their oxidized forms cystine and methionine sulfoxide. The sulfur XANES reveals distinct differences between the reduced and oxidized forms of these building blocks, as well as between oxidized and reduced glutathione, an important thiol in regulating redox balance in animal cells. These spectra were used to simulate the sulfur XANES from whole human blood, and its components plasma and erythrocytes. The goal was to identify and quantify the amounts or thiol and disulfide sulfur present *in vivo*. The relatively low energy of the sulfur K-edge (about 2.5 keV) compared to Mn and Sr presented practical difficulties for this experiment.

However, our success in addressing these challenges, which showed the efficacy of sulfur XAS in biology, paves the way for other "low energy" XAS work (such as Ca in PS II).

Finally, future avenues for research are discussed in Chapter 6. Chief among these is Ca EXAFS, the foundations for which were prepared by the experience with sulfur XAS. Because of the lessons learned from those studies, Ca EXAFS on PS II, long considered unrealistic, can become a practical reality. We can then probe the native cofactor and avoid the risks and treatments involved in Sr substitution. The following chapters illustrate the successful application of x-ray absorption spectroscopy to these biologically important elements Sr (for Ca), Mn and S, which are present in such diverse areas as photosynthesis and human physiology.

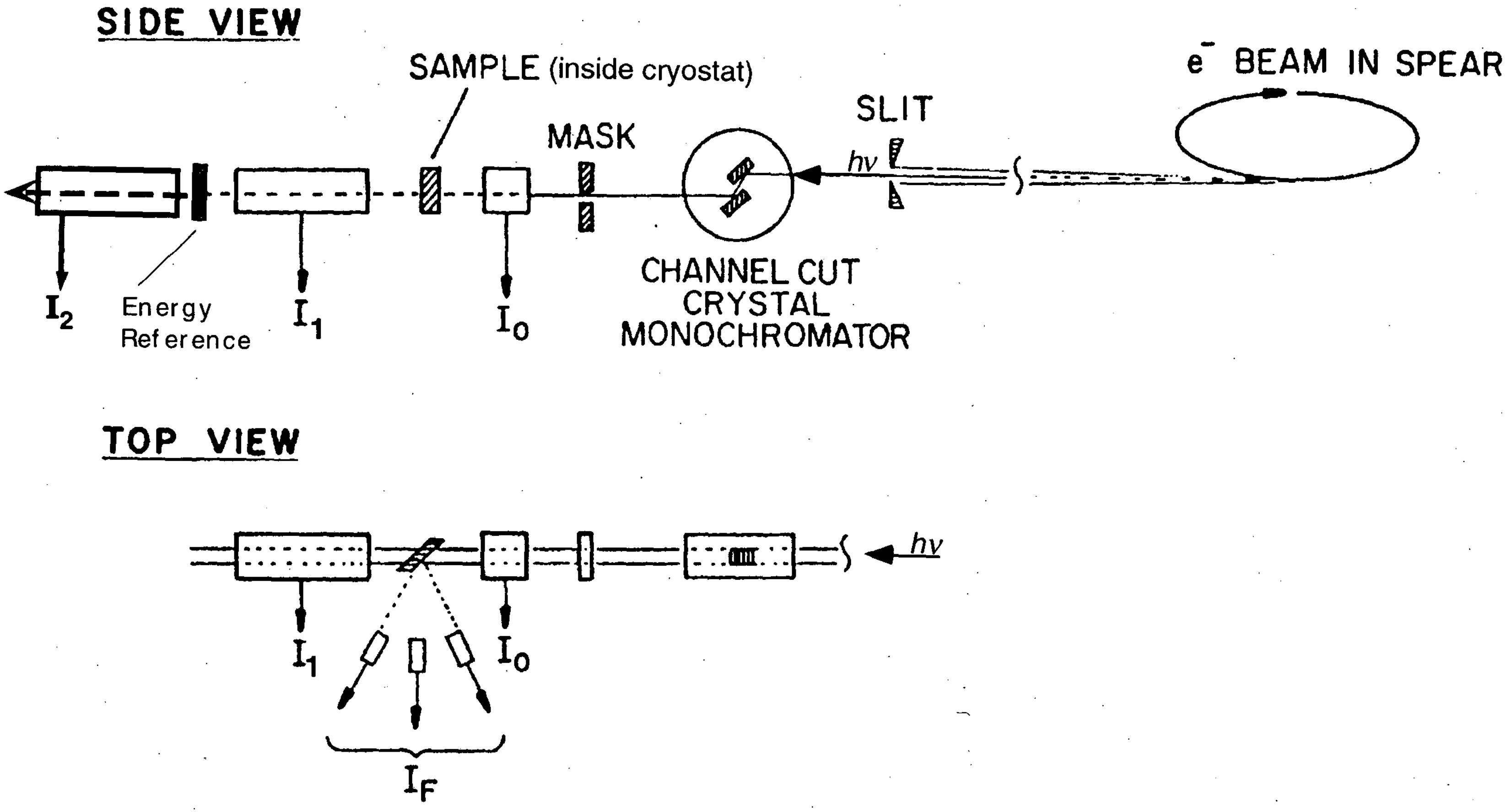
SIDE VIEW
SAMPLE (inside cryostat)
e⁻ BEAM IN SPEAR
SLIT
hν
MASK
I_2
Energy Reference
I_1
I_0
CHANNEL CUT CRYSTAL MONOCHROMATOR
TOP VIEW
hν
I_1
I_0
I_F

Absorbance = I_F/I_0

Figure 1.1 Schematic of experimental setup common for the four synchrotron radiation studies presented in this volume. This diagram is applicable to the experiments conducted at SSRL. The side view shows the entire length of the setup while the top view focuses on the fluorescence detection system. The top view shows that the sample is typically positioned 45° to the x-ray beam so that I_F can be measured by a Ge detector (or Lytle detector), located 90° to the beam. See text for further description.

Chapter 2 — Strontium EXAFS Reveals the Proximity of Calcium to the Manganese Cluster of Oxygen-Evolving Photosystem II

Introduction

Green plants, algae and cyanobacteria supply almost all the dioxygen in the biosphere as a byproduct of photosynthesis, through the light-driven oxidation of water:

$$2H_2O \rightarrow O_2 + 4H^+ + 4e^- \qquad (2.1)$$

This crucial reaction is catalyzed by the Oxygen-Evolving Complex (OEC), which is located at the donor side of Photosystem II (PS II), an intrinsic thylakoid membrane protein assembly that, along with Photosystem I, helps accomplish the net reaction:

$$H_2O + CO_2 \rightarrow O_2 + \text{carbohydrates} \qquad (2.2)$$

Comprising the OEC are four manganese atoms, along with essential cofactors Ca^{2+} and Cl^-.[3,9,10] Without X-ray crystallographic information about PS II (due to the lack of suitable crystals), most of the structural knowledge about the oxygen-evolving complex has resulted from biochemical, spectroscopic and kinetic studies targeting the catalytically active site.[11-13] By these studies the active site of the complex is known to consist of a tetranuclear manganese cluster that cycles through five intermediates S_i (i= 0-4), accumulating oxidizing equivalents serially until releasing dioxygen in the transition from S_4 to S_0.[14,15] In this manner the complex couples the one-electron photooxidation of the reaction center chlorophyll P_{680} with four-electron water oxidation without generating damaging intermediates. Much has been learned about the catalytic Mn cluster, and a working model has been proposed[11,16-18] based mainly on X-ray absorption spectroscopy (XAS) and electron paramagnetic resonance (EPR) studies. Both X-ray absorption near-edge structure (XANES) and extended X-ray absorption fine structure (EXAFS) experiments have focused on the Mn atoms of the OEC to obtain oxidation states,[19,20] and structural information about this active site.[21-26]

Along with manganese and chloride, Ca is an essential cofactor in oxygen evolution.[3,9,27,28] Depleting this cofactor suppresses OEC activity, which can be restored (up to 90%) by replenishing with Ca^{2+}. Partial reactivation (up to 40%) results from addition of strontium to Ca-depleted PS II membranes[29,30] and no other metal ions (except VO^{2+}, vanadyl ion[31]) can restore activity, making this requirement highly specific for calcium.[32-34]

Although Sr^{2+} replenishes the Ca-depleted centers to a similar extent as added Ca^{2+}, the slower kinetics of the OEC turnover yields an overall lower steady-state rate[35] (40%) at saturating light intensities. Substitution of Ca with Sr also alters the EPR multiline signal (MLS) from the S_2 state, giving narrower hyperfine splitting and different intensity patterns.[30,36-38] Most researchers addressing the stoichiometry of the Ca cofactor in PS II now conclude that functional water oxidase activity requires one essential Ca^{2+}, which can be removed by low-pH/citrate or 1.2 M NaCl wash.[32,39-42] In higher plants, another more tightly bound Ca is associated with the light-harvesting complex (LHC II) and requires harsher treatments for its removal.[43-45]

There is some debate about the environment of the Ca cofactor binding site and its function. Several investigations have involved substitution of various metals into this binding site, followed by EXAFS studies on the Mn cluster. One set of experiments using EXAFS on Sr-reactivated PS II membranes was interpreted to indicate a 3.4-3.5 Å distance between the Ca (Sr) and the Mn cluster.[46] This conclusion was based on the observation of increased amplitude in the Fourier transform peak at 3.3 Å upon replacement of Ca with Sr, a heavier atom and better X-ray scatterer. This close link is also supported by FTIR spectroscopic work[47,48] that is consistent with a carboxylate bridge between Mn and Ca. Analysis of EXAFS spectra from purified PS II membrane preparations indicated a Mn–Ca interaction at slightly longer distance[49] (~3.6-3.7 Å). Ca depletion by NaCl-washing of PS II membranes removed the 16 and 23 kDa extrinsic proteins[50] and led to a reduced amplitude for this 3.6 Å feature.[26] Because of the lower X-ray scattering ability of sodium, this result was interpreted as possible Na^+ substitution for Ca^{2+} at this distance.[26]

However, another Mn EXAFS study[51] did not detect any changes in the Fourier peak at 3.3 Å when Ca was replaced with Sr^{2+} or Dy^{3+} in PS II reaction center complexes lacking the 16 and 23 kDa extrinsic polypeptides. These authors found no evidence of an EXAFS-detectable Mn–Ca interaction at about 3.3 Å and, therefore, no Ca within the vicinity (≤4 Å) of the Mn cluster. Other Mn EXAFS experiments on terbium(III)-substituted PS II, where Tb^{3+} displaced Ca^{2+} from its binding site without prior depletion, supported this alternative view.[52] Because Tb^{3+} is a competitive inhibitor of Ca^{2+} binding, the oxygen evolving activity was suppressed in these samples, but the Mn EXAFS exhibited no change from the substituting lanthanide. Tb^{3+} was not needed to fit the ~3.4 Å distance in the Mn EXAFS spectrum, implying a Ca binding site that is at least 4 Å away from the Mn.[52] More support came from EPR-based experiments involving Mn^{2+} substitution in Ca-depleted (inactive) PS II membranes, which indicated that the Mn^{2+}-occupied Ca binding site was outside the first coordination region of the catalytic cluster[53] (beyond 4 Å).

Given this uncertain situation and to further test whether a Ca binding site is close to the Mn cluster, we decided to embark on a different approach:

to use strontium EXAFS methods to probe from the Sr cofactor point-of-view for nearby Mn within 4 Å. This is the reverse of the previously described Mn EXAFS studies that concentrated on the Mn cluster,[46,51] and probed for nearby Ca or Sr neighbors. Several factors favor Sr as the better cofactor for this XAS study. First, the X-ray energies involved (16 keV for the K-edge) are more penetrating and not attenuated by air. The higher X-ray absorption cross-section and fluorescence yield of Sr also make the experiment practicable. This study then constitutes, to our knowledge, the first application of Sr EXAFS methods to biological systems. Materials science examples of Sr EXAFS techniques[54-58] are known, dealing mainly with minerals containing Sr.

Without spectroscopic handles for Sr, such as UV-Vis, EPR or Mößbauer, XAS is a valuable tool[8], because XAS is element specific and sensitive when coupled with fluorescence detection.[59,60] The technique has been widely used to probe the active sites of metalloproteins[7,61,62] in non-crystalline samples. In particular, EXAFS gives information about the averaged local structure (within ~4 Å) around the absorbing metal center: radial distribution of distances, identities and number of neighbors. Scatterers can be distinguished if they have non-proximate atomic number (Z). Distances and coordination numbers can be determined with respective accuracies of 2% and 30%.[7,8,62] The Sr EXAFS-based experiment requires PS II samples with Sr substituted for Ca while maintaining oxygen-evolving activity and a stoichiometry of 1 Sr per PS II, to focus on the functional cofactor binding site. Along with reactivated Sr-PS II, we can prepare an inactivated sample by treating with hydroxylamine (NH_2OH) to disrupt the Mn cluster and suppress water oxidase activity.[63-65] A comparison can then be drawn between the coordination environments of Sr in functional and in inactivated PS II to derive insight into the location of the original Ca cofactor in native PS II. From these Sr substitution experiments, EXAFS provides further evidence that the Ca (Sr) cofactor is near the Mn catalytic cluster, at ~3.5 Å. The finding indicates that the active site of oxygen evolution is a heteronuclear Ca-Mn complex.

Experimental Section

Sr^{2+}-reactivated PS II Sample Preparation

PS II-enriched membranes were prepared by Triton X-100 (Sigma) extraction of thylakoids from spinach.[66,67] The oxygen-evolving enzyme activity ranged from 300 to 400 μmol O_2/mg chlorophyll (Chl)/h. These native PS II samples were stored and frozen in Buffer A: 0.4 M sucrose, 50 mM 2-(N-morpholino)ethanesulfonic acid (MES), 30 mM NaCl, 5 mM $MgCl_2$, pH 6.5 at -20°C. Glassware, utensils and plasticware were acid-washed and rinsed thoroughly with deionized water, whereas the Ca-free buffers were treated with Chelex-100 resin (Bio-Rad) to remove Ca contamination. Biochemical sample handling was done in the dark with safe green light at 4°C. Ca-depletion followed the low-pH protocol of Ono and Inoue:[32] PS II membranes were quickly but thoroughly resuspended to 0.5 mg Chl/mL in Buffer B containing 10 mM citrate (pH 3.0), 0.4 M sucrose, 20 mM NaCl and incubated for 5 min while stirring. Addition of 1/10th volume of 0.5 M morpholinopropanesulfonic acid (MOPS) buffer (Buffer C, with 0.4 M sucrose, 30 mM NaCl, pH 7.5) returned the mixture to pH 6.5.[68,69] After stirring for 2 min, the membranes were collected by centrifugation (10 min at 40000 *g*). Incidentally, this protocol retains the 16 and 23 kDa extrinsic polypeptides.[70] The resulting pellets were reconstituted with $SrCl_2$ or $CaCl_2$ (40 mM, with 25 mM MES and 30 mM NaCl at pH 6.5) by homogenizing slowly under room light for 4 min.[30,46] Sucrose was omitted from the divalent cation buffers to speed metals reconstitution and 2.5% ethanol (v/v) was added to minimize the g= 4.1 EPR signal from spinach PS II preparations.[71] After centrifugation, the samples were washed with Buffer F (25 mM MES, 30 mM NaCl, 2 mM

$MgCl_2$ and 2.5% ethanol at pH 6.5) and pelleted again for 15 min at 40000 *g* to yield Sr-reactivated and Ca-reactivated PS II.

Sr-PS II Sample Preparation by Removal of Excess Sr

To remove the weakly bound, non-essential Sr or Ca, we used the direct Chelex treatment of PS II.[42,44,72] The Sr- or Ca-reactivated samples were resuspended in sucrose-free Buffer F at a concentration of 0.25 mg Chl/mL. Two grams of Chelex-100 per mg Chl was added and the mixture was stirred gently for 1 h. Chelex can increase the pH of the buffer,[72] so the pH was adjusted to 6.5 before mixing with PS II. After 1 h of stirring, the suspension was filtered to separate the resin from the PS II particles. Centrifugation (10 min, 40000 *g*) was followed by resuspension in Buffer F (with 2.5% ethanol, v/v). One final pelleting step was done in an ultracentrifuge (Beckman) using a Ti-60 rotor (160000 *g*, 1.5 h). The Chelex-treated pellets, designated Sr-PS II or Ca-PS II, were transferred to Mylar-backed Lucite sample holders designed to fit in EPR and XAS cryostats. These *intact* Sr- and Ca-PS II samples were dark-adapted for 1 h (at 4°C) to poise them in the S_1 state before freezing and storage in liquid nitrogen. The *inactive* Sr-PS II was prepared by adding 30 μL of a stock solution (100 mM) of NH_2OH to the intact Sr-PS II pellet. After incubation for 20 min, and without further washing or centrifugation, the NH_2OH-saturated material was transferred to Mylar-backed sample holders and frozen in liquid nitrogen. All samples were maintained at 77 K except during transfer to and from the EPR or XAS cryostats.

Oxygen-Evolution Assays

Enzyme activity for the six different types of samples (PS II, Ca-depleted, Sr/Ca-reactivated, Sr/Ca-PS II) was assayed under saturating white light using a Clark-type oxygen electrode (Yellow Springs Instruments).[25,46] The respective divalent cations (Sr or Ca, 20 mM) were added to the Sr- or Ca-containing PS II samples to achieve maximum activity, but the Ca-depleted sample received no added cations. Chlorophyll assays were done on 80% acetone extracts[73] using updated extinction coefficients.[74] Actual concentrations used for the activity assays were 10-15 μg Chl/mL.

EPR Spectroscopy

X-band (9.2 GHz) EPR spectra were acquired on PS II samples inside XAS Lucite holders using a Varian E-109 system equipped with a standard TE_{102} cavity and a Heli-tran liquid helium cryostat (Air Products). Low temperature (8 K) spectra to monitor EPR-detectable Mn^{2+} were collected on samples before and after exposure to X-rays to check that no significant sample damage had occurred. The Ca- and Sr-treated, and untreated PS II samples were poised in the S_2 state by illumination for 4 min at 200 K (dry ice/ethanol bath) using a 400 W tungsten lamp (General Electric) and an aqueous $CuSO_4$ filter (5% w/v, 7 cm path). EPR data were displayed as difference (light-minus-dark) spectra. The multiline signal in the S_2 state was used to characterize the Sr- and Ca- reactivated samples and the turnover of the OEC. For Ca-depleted PS II, illumination for 2 min at 0°C produced the characteristic split S_3' EPR signal, centered at $g = 2$ with a 164 G width.[36,75,76]

Metals Quantitation

PS II samples were first digested in boiling, concentrated ultra pure HNO_3 (Optima brand, Fisher), then diluted to 10 mL with deionized water. Elemental analysis of Mn and Sr in the ppb range were carried out at the Microanalytical Lab in the U. C. Berkeley College of Chemistry using inductively coupled plasma and atomic emission spectroscopy (ICP-AES). The amounts of PS II per sample were calculated from the chlorophyll assays, assuming 200 Chl per PS II.[41,42,77]

EXAFS Measurements

Sr K-edge EXAFS experiments resembled those previously described for Mn.[46] They were conducted at the Stanford Synchrotron Radiation Laboratory (SSRL) on Beamlines VII-3 and IV-3 in unfocused mode using a Si[220] double crystal monochromator, and a Canberra Instruments 13-element, energy-resolving Ge detector.[7] The storage ring operated at 3 GeV energy and current of 65-100 mA. Tantalum slits at the beam exit port kept the beam size at ~ 2 × 12 mm. An Oxford Instruments CF 1208 liquid helium flow cryostat maintained the temperature at 10 ± 1 K, and the EXAFS data were recorded as fluorescence excitation spectra by monitoring the Sr fluorescence peak at 14.2 keV as we scanned from 16.0 to 17.0 keV. Amplifier shaping times were set at 0.1 μs and the total incoming count rates (ICR) were kept below 100 kHz, within the linear region of fluorescence vs. ICR curve. Single-channel analyzer windows were set to collect the Sr K_α peak. No subsequent electronic dead-time corrections to the data were required. Absorption was equated[78] to fluorescence (F) divided by the incident flux (I_0), which was measured by a nitrogen-filled ion chamber. For energy calibration, we simultaneously measured the absorption spectrum of solid strontium acetate, whose edge peak was assigned the value 16.120 keV, near the reference value for elemental Sr (16.105 keV).[79] Detuning the monochromator by 50% at 17.0 keV achieved harmonic rejection. Spectra were collected with 3 eV steps in the pre-edge region (15970 - 16070 eV), 1 eV steps from 16070 to 16134 eV, and 0.075 Å^{-1} steps from k = 2.0 - 13.5 Å^{-1}. Five sets of data from four separately prepared intact Sr-PS II and inactive Sr-PS II samples were collected and analyzed (up to fifty 20-min scans averaged for each set).

Data Analysis

To analyze Sr EXAFS data, we followed a procedure similar to that used for Mn data.[21,46,78] A linear function was first subtracted to achieve a flat background in the pre-edge region. The post-edge region was divided by the free-atom absorption of Sr and normalized to a unit edge jump as determined by extrapolating a quadratic fit of the post-edge absorption to an energy near the edge peak. A smooth background absorption curve (polynomial fit of post-edge region) was then subtracted to give the net EXAFS. Spectra were converted from energy scale into photoelectron wave vector (Å^{-1}) with the equation:[78]

$$k = (2\pi / h)[2m_e(E - E_0)]^{1/2} \qquad (2.3)$$

where m_e is the electron mass, h is Planck's constant, E is the X-ray energy and E_0 is the ionization threshold, chosen as 16.120 keV. After weighting by k^3, k-space background removal was achieved by subtracting a four-domain cubic spline to minimize peaks at apparent distance 'R'$\leq$ 1 Å in the Fourier transform. The data were then truncated near the zero crossings (k = 3.6 - 13.2 Å^{-1}) before the Fourier transform was applied.

Fourier filtering is commonly used to simplify curve-fitting of EXAFS data and works for well-separated peaks.[62,78,80,81] It allows analysis of the contributions from single peaks or frequency components. Here, we focus on the important long-range interactions at 'R'$\geq$ 3 Å. To isolate a single peak, a Hanning window function is applied to the first and last 15% of the range, while leaving the middle 70% untouched. The back-transformed, Fourier-isolated data in *k*-space were then subjected to curve fitting, using *ab initio* phase and amplitude functions calculated using the program FEFF 5.05.[82,83] The EXAFS amplitude, $\chi(k)$, is described by the following equation:

$$\chi(k) = S_0^2 \sum_i N_i B_i(k) \frac{f_{eff}(\pi,k,R_i)}{kR_i^2} \exp(-2\sigma^2 k^2) \exp\left(\frac{-2R_i}{\lambda(k)}\right) \times \sin\left[2kR_i + 2\delta_i^c(k) + \phi_i(k)\right] \tag{2.4}$$

where for each shell i, N_i is the number of scatterers at a distance R_i, S_0^2 is the many-body amplitude reduction factor, $B_i(k)$ is an amplitude reduction factor caused by inelastic forces in the central atom, f_{eff} is the effective backscattering amplitude of the scattering atom, δ_i^{c} and ϕ_i are the respective phase shifts for the absorber and backscatterer, σ^2 is the Debye-Waller term, and $\lambda(k)$ is the mean free-path of the photoelectron.

FEFF 5.05 functions (f_{eff}, δ, ϕ, λ) were calculated using single-scattering curved-wave theory for a simple structural model of oxygen-ligated Sr with Mn (or other atoms, C, O, S, P, Cl) located at different distances (3.0-4.0 Å) from the central Sr atom. This method gave a range of possible Sr–X interactions, depending on which was needed for curve fitting. Sr-(L-aspartate) provides a good model of Sr in a protein environment, where amino acids may supply ligands, and the crystal structures of this compound and Sr-(L-glutamate) have been published.[84,85] The core of the FEFF model was derived from Sr-(L-aspartate) or strontium carbonate, using interactions up to 4 Å away from the central Sr atom. The value for S_0^2 was fixed at 0.85 for all fits.[46,80]

The normalized error sum Φ, representing the quality of the fit, is given by:

$$\Phi = \sum_{i}^{N} \left(\frac{1}{s_i} \right)^2 \left[\chi^{\text{expt}}(k_i) - \chi^{\text{calc}}(k_i) \right]^2 \tag{2.5}$$

where N is the number of data points, $\chi^{\text{expt}}(k_i)$ and $\chi^{\text{calc}}(k_i)$ are the experimental and calculated EXAFS.[86] The normalization factor s_i is defined as:

$$\frac{1}{s_i} = k_i^{\,3} \Big/ \sum_{j}^{N} k_j^{\,3} \left| \chi_j^{\text{expt}}(k_j) \right| . \tag{2.6}$$

The ε^2 error accounts for the number of variable fit parameters (p) and the number of independent data points (degrees of freedom, N_{ind})[21,46,86] and is given by a reduced χ^2 statistical function:

$$\varepsilon^2 = \left[N_{ind}/(N_{ind} - p) \right] N^{-1} \cdot \Phi \tag{2.7}$$

Following from the Nyquist sampling theorem, N_{ind} is approximated by $2\Delta k \Delta R/\pi$, where Δk is the k-range of the data used, and ΔR is the width of the Fourier-filtered peak.[86] A negative value for ε^2 means that the fit is underdetermined because we have exceeded the justifiable number of parameters, so the fit solution is not considered to be unique.[46] By accounting for the degrees of freedom and the justifiable number of parameters, the ε^2 value lets one distinguish whether including more parameters (p) actually improves the fit quality. Curve-fitting was done by minimizing the error sum (Φ) using a non-linear least squares method, while varying the parameters for each shell of scatterers: R, coordination number N, σ^2 and ΔE_0. Distances can be reliably determined with an accuracy of 2%, whereas the N can incur errors up to 30%.[8] Absolute fit quality was judged through a combination of criteria: numerically by Φ, visually by how the fit follows the amplitude envelope and phase of the data, and whether parameters are chemically and physically reasonable.

Results

Oxygen-Evolving Activity Data

Table 2.1 shows representative rates of oxygen evolution in the process of preparing the Sr-substituted PS II samples. The six samples considered were: native PS II (untreated), Sr- and Ca-reactivated (with excess Sr/Ca), Ca-depleted, Sr- and Ca-PS II (Chelex-treated). The O_2 activity of untreated PS II (~300 μmol O_2/h/mg Chl) was the control (100%), so that all other values were normalized by this number. The typical percentages shown agree with the reports for Ca-depleted and substituted samples.[87] The measure of Ca-depletion was the extent of suppression of water oxidase activity. As expected, Sr substitution induced a lower steady-state rate (~40%), which served as a useful characteristic of the treatment. We have also reproduced a previous study[35] on the light-intensity dependence of oxygen evolution in Sr- and Ca-treated PS II (Appendix 1). Under limiting light Sr reactivates oxygen evolution almost as efficiently (81%) as Ca. However, during saturating light conditions, Sr reactivates only partially (40%) compared to Ca. The authors of that study concluded that Sr binding reconstitutes oxygen evolution but the rate-limiting step of the reaction is slower than for Ca.[35] For saturating light the pattern of oxygen activity is as follows: Ca-depleted 10-25%,[32,87] Sr-reactivated 30-40%,[36] Ca-reactivated 70-90%,[87] relative to control PS II (100%). The Ca-PS II and Sr-PS II values in Table 2.1 indicate that the Chelex wash to remove excess Sr or Ca does not harm or irreversibly inhibit the enzyme function. The data for NH_2OH-treated Sr-PS II are not shown, but the excess NH_2OH totally inhibits activity by disrupting the catalytic Mn cluster.[88]

Table 2.1 O_2 Activity Data

Sample	Activity (μmol O_2/h /mg Chl)	% vs. Native PS II
Native PS II (control)	268 ± 14	100
Ca-Reactivated PS II	221 ± 39	82
Sr-Reactivated PS II	100 ± 5	37
Ca-Depleted PS II	38 ± 5	14
Ca-PS II	219 ± 4	82
Sr-PS II	99 ± 4	37

Oxygen-evolving activity was assayed under saturating white light, in Buffer A at 25°C. Native (untreated) PS II was regarded as the control and its activity was taken as 100%. The other samples tested were Ca- and Sr-reactivated (with excess Ca/Sr), Ca-depleted, Ca- and Sr-PS II (Chelex-washed). Supplementary divalent cations (20 mM) were added to achieve maximum activity: Ca^{2+} to the native PS II and Ca-treated samples, and Sr^{2+} to the Sr-treated samples. Ca-depleted PS II was tested without added cations. DCBQ (2,5-dichloro-*p*-benzoquinone) was used as an electron acceptor at 2 mM final concentration, from a stock solution in DMSO (dimethylsulfoxide). Standard deviations for the measurements are included.

EPR Spectroscopy

Upon substitution of Sr for Ca, an altered EPR multiline signal (MLS) appears in the difference (light-minus-dark) spectra of Sr-reactivated samples (Fig. 2.1A). The changes were consistent with those observed previously:[30,38,46] reduced overall amplitude throughout and at the wings of the MLS, slightly narrower hyperfine splitting, and different intensity pattern. In addition, a feature at 3670 G was prominent in the Sr-reactivated compared to Ca-containing samples. A wider scan range (Fig. 2.1B) also shows the increased amplitude of the $g= 4.1$ EPR signal in Sr-reactivated samples.[30,46,51] Together, both aspects of the light-induced (S_2) EPR signal indicated the successful replacement of Ca by Sr. After Chelex treatment, the Sr-altered MLS almost completely reverted to the normal MLS (data not shown). The cause of the loss of this diagnostic EPR signature is the subject of further investigation (Chapter 6), but the aforementioned oxygen-evolving activity and Sr quantitation indicated the presence of functional Sr in PS II. Lastly, the characteristic split S_3' EPR signal was also observed in the Ca-depleted samples when illuminated at 0°C for 2 min (data not shown). Its presence showed that Ca is removed from its cofactor binding site, with suppression of enzyme activity, before reactivation with Sr or Ca.

Metals Analysis

Amounts of Sr were normalized per four Mn, the unit of functioning catalytic centers in PS II.[89,90] For Sr-reactivated samples before the Chelex treatment, Sr content was about 16 Sr /4 Mn; this decreased to 0.75 Sr / 4 Mn upon removal of excess cation (Sr-PS II). This stoichiometry was consistent the finding that about 1 Ca^{2+} per PS II is necessary for oxygen-evolving

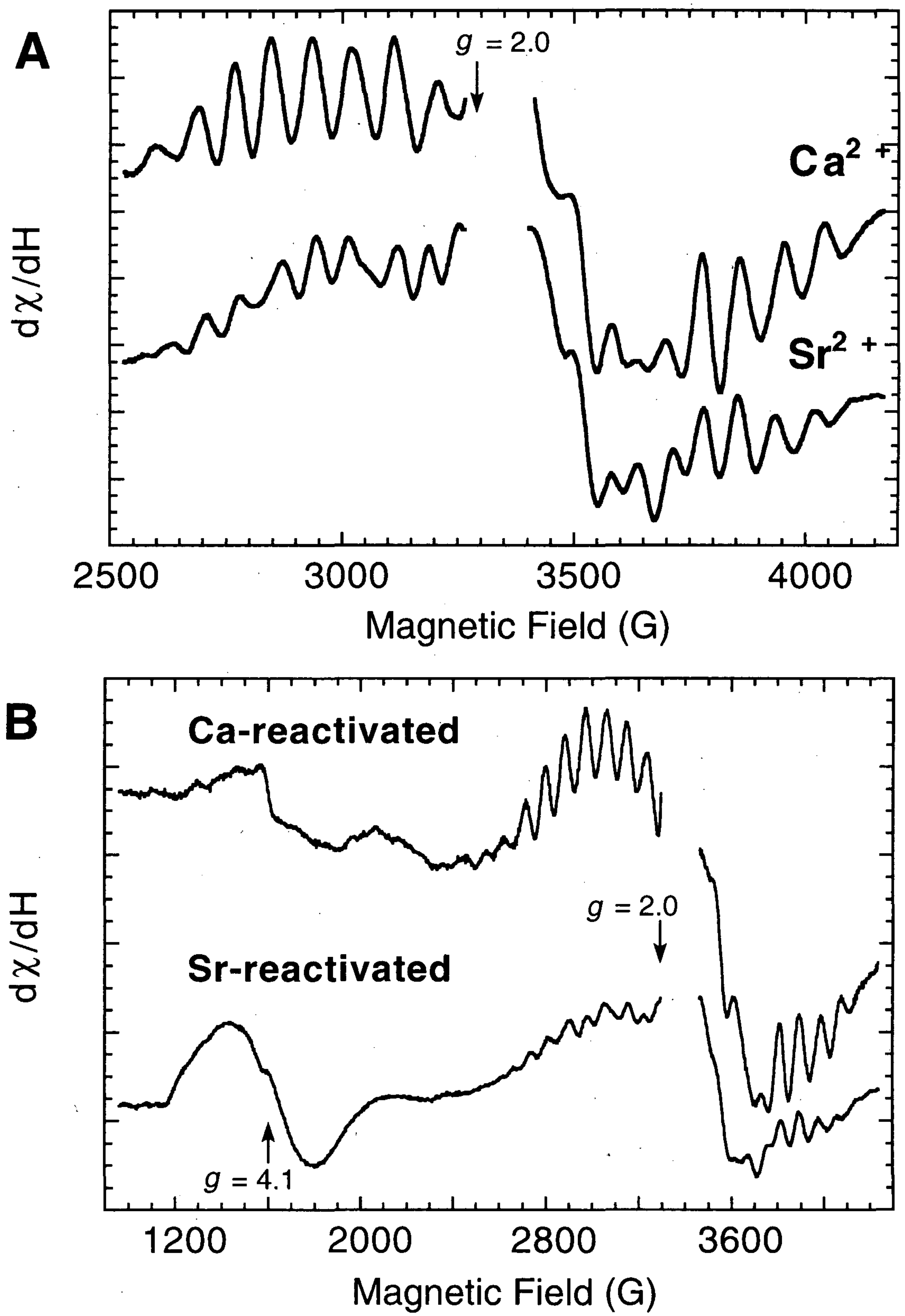
A
g = 2.0
Ca2+
Sr2+
dχ/dH
2500
3000
3500
4000
Magnetic Field (G)
B
Ca-reactivated
Sr-reactivated
g = 2.0
g = 4.1
dχ/dH
1200
2000
2800
3600
Magnetic Field (G)

Figure 2.1 EPR Spectra of Sr- and Ca-reactivated PS II samples after low pH treatment.

(**A**) These are difference (light-minus-dark) EPR spectra of the multiline signal region for Ca- and Sr-reactivated samples. Differences are visible between the two types of samples, such as the reduced amplitude in the wings of the Sr-altered multiline signal, and its different spacing compared to the Ca-reactivated MLS, which is essentially identical to that of native PS II.

(**B**) A wider EPR scan range includes both the $g = 4$ and $g = 2$ regions. The $g = 4.1$ EPR signal is enhanced in the Sr-reactivated compared to Ca-reactivated PS II, although both samples contained 2.5% ethanol, which is reported[71] to suppress formation of this signal. For clarity, the $g = 2$ region containing the dark stable Y_D^{ox} radical signal was deleted. Illumination was performed at 200 K (4 min), and all EPR spectrometer conditions were as follows: 8 K temperature, 9.21 GHz microwave frequency, 32 G modulation amplitude, 100 kHz modulation frequency, 0.5 sec time constant, 30 mW microwave power and 4 min scan time.

activity.[39] Although up to 30% of Mn may be lost during the low pH Ca-depletion step,[91] the present study focused on the Sr associated with active oxygen-evolving centers, and was not so adversely affected by the Mn loss as Mn EXAFS studies would be. Because the inactive Sr-PS II samples were derived from the active samples whose Sr concentrations were determined, and no washing steps were done after the hydroxylamine treatment, the Sr content within the Lucite holders for both types of (Chelex-treated) Sr-PS II samples was identical.

Sr EXAFS of Intact and Inactive Sr-PS II in the S_1 State

After the initial characterizations were completed, XAS measurements were made on the two types of (Chelex-treated) Sr-PS II: intact, and inactive samples. Fig. 2.2 shows representative unfiltered, k^3-weighted EXAFS data in k-space, and illustrates the distinct differences between the two samples. The intact Sr-PS II had reduced amplitude at $k \sim 8$ Å^{-1} resulting from the presence of more than one frequency component, whereas the inactive Sr-PS II seemed to possess only one component. The two samples also had different amplitude envelopes, beat patterns and phases, especially beyond $k \sim 9$ Å^{-1}. The Fourier transforms of the Sr EXAFS appear in Figure 2.3, and reveal striking differences in the crucial 'R' ~ 3.0 Å region. The noise level in both spectra was low, as shown by the absence of major peaks beyond 'R' > 5 Å. The intact Sr-PS II displayed two main Fourier peaks (I and II) at 'R' = 2.0 Å and 3.0 Å, whereas the inactive Sr-PS II had only one major peak at 'R'= 2.0 Å.

Fourier peak I dominated the spectrum for both types of Sr-PS II samples (Fig. 2.3) and consisted of the first shell of ligating oxygens. This major feature was roughly similar in the active and inactive samples,

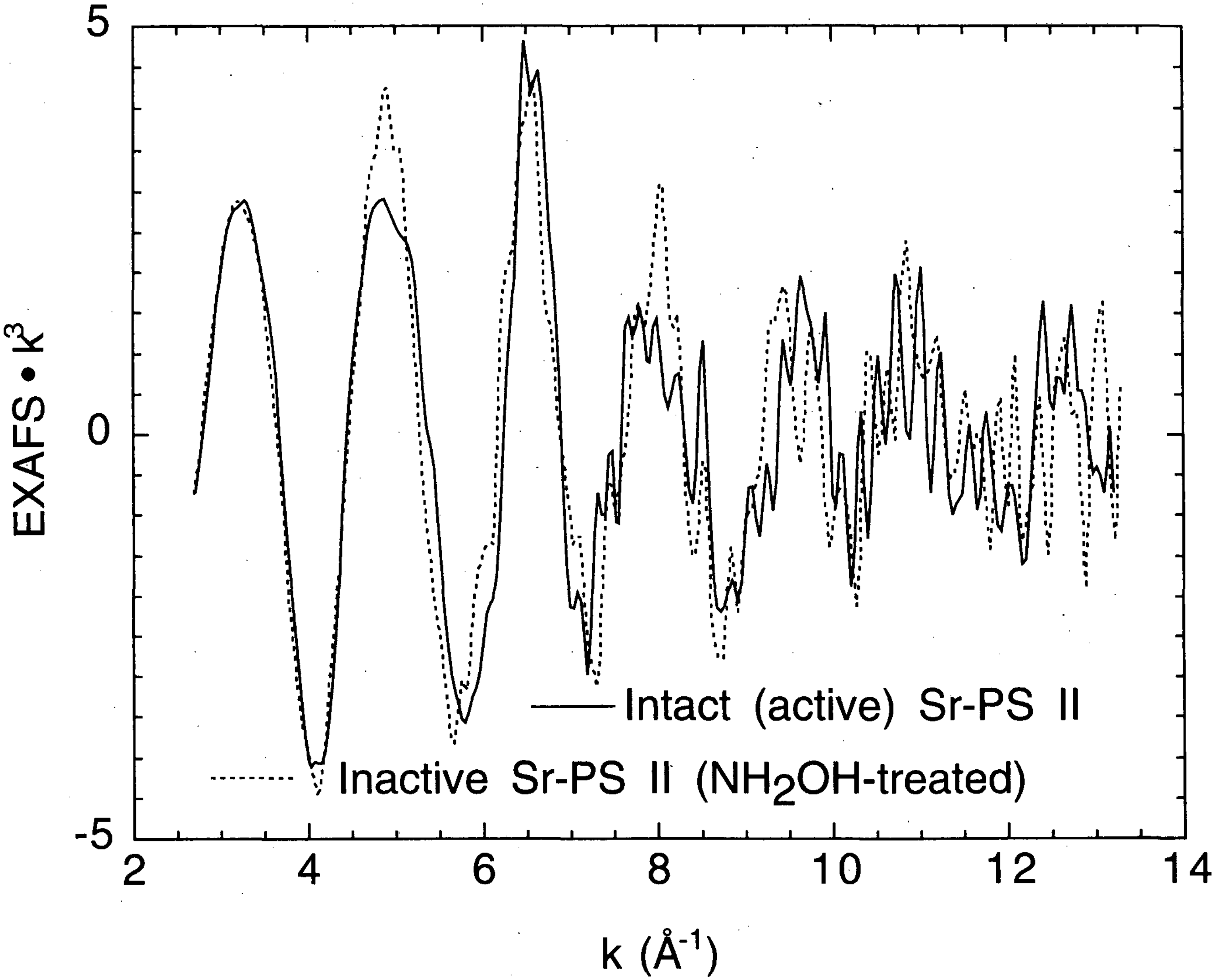
5
0
-5
EXAFS • k^3
2
4
6
8
10
12
14
k (Å^{-1})
Intact (active) Sr-PS II
Inactive Sr-PS II (NH$_2$OH-treated)

Figure 2.2 k^3-Weighted Sr EXAFS data of intact and inactive Sr-PS II (Chelex-treated) in the S_1 state. The average of 100 scans for each type of sample is typical of four separate data sets. The differences between the two are apparent in the amplitude envelopes and the phases, especially beyond $k \sim 9$ Å^{-1}. The intact Sr-PS II (solid line) has multiple frequency components, whereas the inactive, NH_2OH-treated Sr-PS II (dashed line) seems to possess only one component. Beyond $k \sim 12$ Å^{-1}, the inactive sample has no discernible feature in the EXAFS (only noise present).

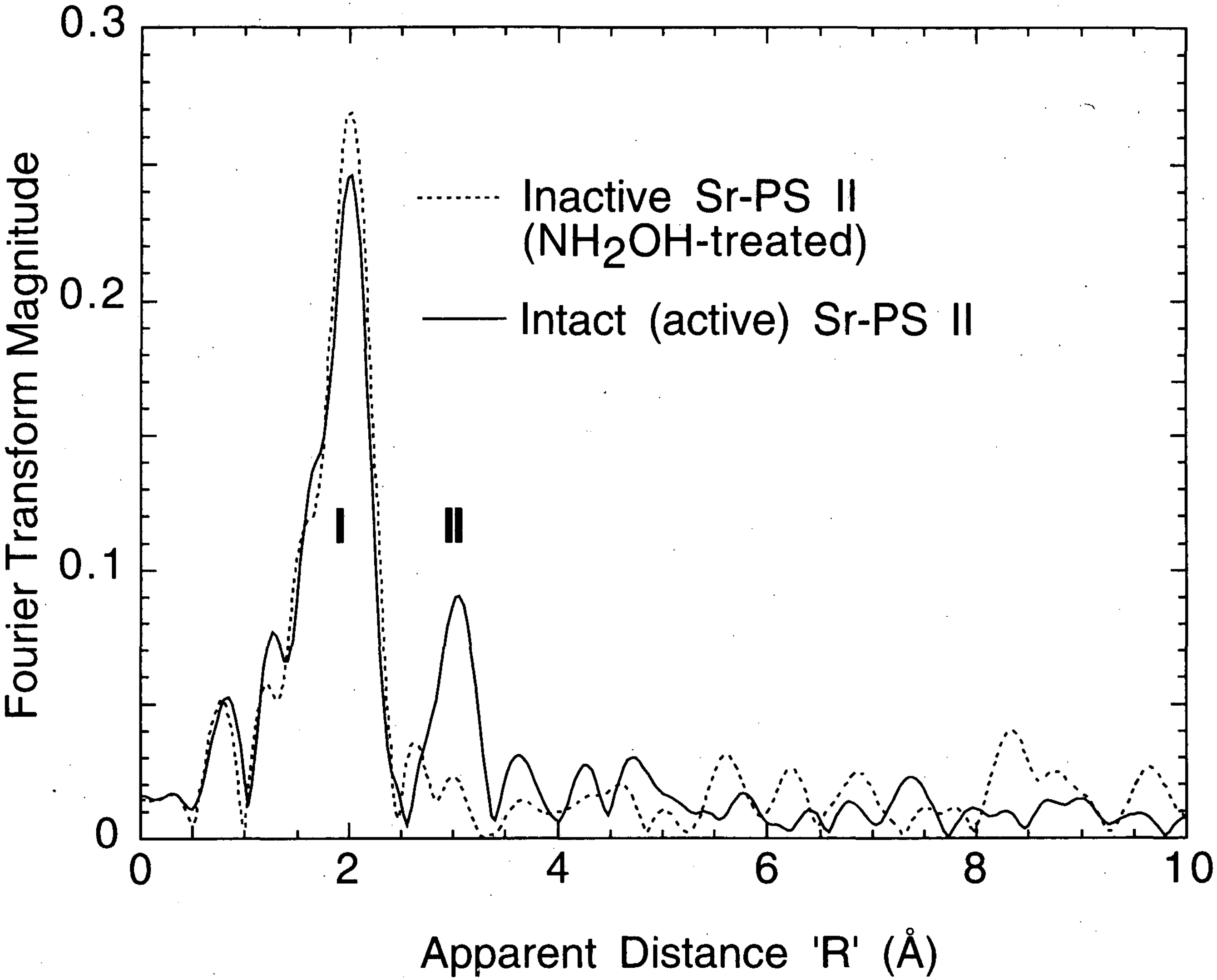
0.3
0.2
0.1
0
Fourier Transform Magnitude
Inactive Sr-PS II
(NH$_2$OH-treated)
Intact (active) Sr-PS II
I
II
0
2
4
6
8
10
Apparent Distance 'R' (Å)

Figure 2.3 Fourier transforms of Sr EXAFS for intact and inactive Sr-substituted PS II samples (Chelex-treated) from Figure 2.2. Features around '*R*'= 1 Å are due to incomplete background removal. The dominant Fourier peak I is due to ligating oxygens in the first coordination sphere and is common to both samples. The two Sr-PS II samples differ mainly at the '*R*' = 3.0 Å region, where the intact samples exhibit Fourier peak II. This peak is present in each of the four active samples represented by this spectrum. The absence of peak II in NH_2OH-treated sample may be a result of the disruption of the Mn cluster, and serves to provide a comparison between the Sr coordination environment in the active or inactive PS II. Because it is resolved from the major peak I, peak II can be isolated for further curve fitting to determine the identity and number of contributing scatterers.

indicating the presence of similar nearest-neighbor shells. The first peak can be simulated by 9 ± 2 oxygen at 2.57 ± 0.02 Å, where the error in coordination number is estimated at ±30%.[8] The known coordination numbers of Sr^{2+} range from 6 to 9, and Sr–O distances are distributed from 2.56 to 2.71 Å.[84,85,92] Fourier peak II ('R'= 3.0 Å) was consistently present in the four sets of intact Sr-PS II and absent in all four inactive Sr-PS II data sets. Beyond the first shell, coordination environments for Sr were different, so we focus on the main point of contrast: Fourier peak II.

Curve Fitting of Sr EXAFS Data

To determine the number and identity of contributing scatterers, Fourier peak II was isolated (ΔR = 1.0 Å) and back-transformed into k-space (k-range = 3.7 – 13.0 Å^{-1}) for curve fitting. Peak II was sufficiently resolved to allow easy separation from the dominant influence of peak I. The simulations started with chemically reasonable scatterers at about 3.5 Å from strontium, and fitting results are summarized in Table 2.2. First, we tried one shell of carbon at a distance of about 3.5 Å, representing light-atom scattering from possible carboxylate ligands. As Figure 2.4A shows, the fit was poor, especially in the middle of the range, $k \sim 6 – 9$ Å^{-1}, with a mismatch of amplitude envelopes and phases. The amplitude function of C, as calculated from FEFF (using $SrCO_3$), contains a minimum at $k \sim 7$ Å^{-1}, which probably explains the similar pattern in the carbon simulation. However, when one shell of a heavier, metal scatterer (Mn) was used, the fit improved visibly (except in the low-k region, 4 – 5 Å^{-1}) and numerically, by a factor of three, judging from Φ. In this case, the coordination number was fixed at integer values, and N = 2 was found to yield the best fit of the data (Figure 2.4B).

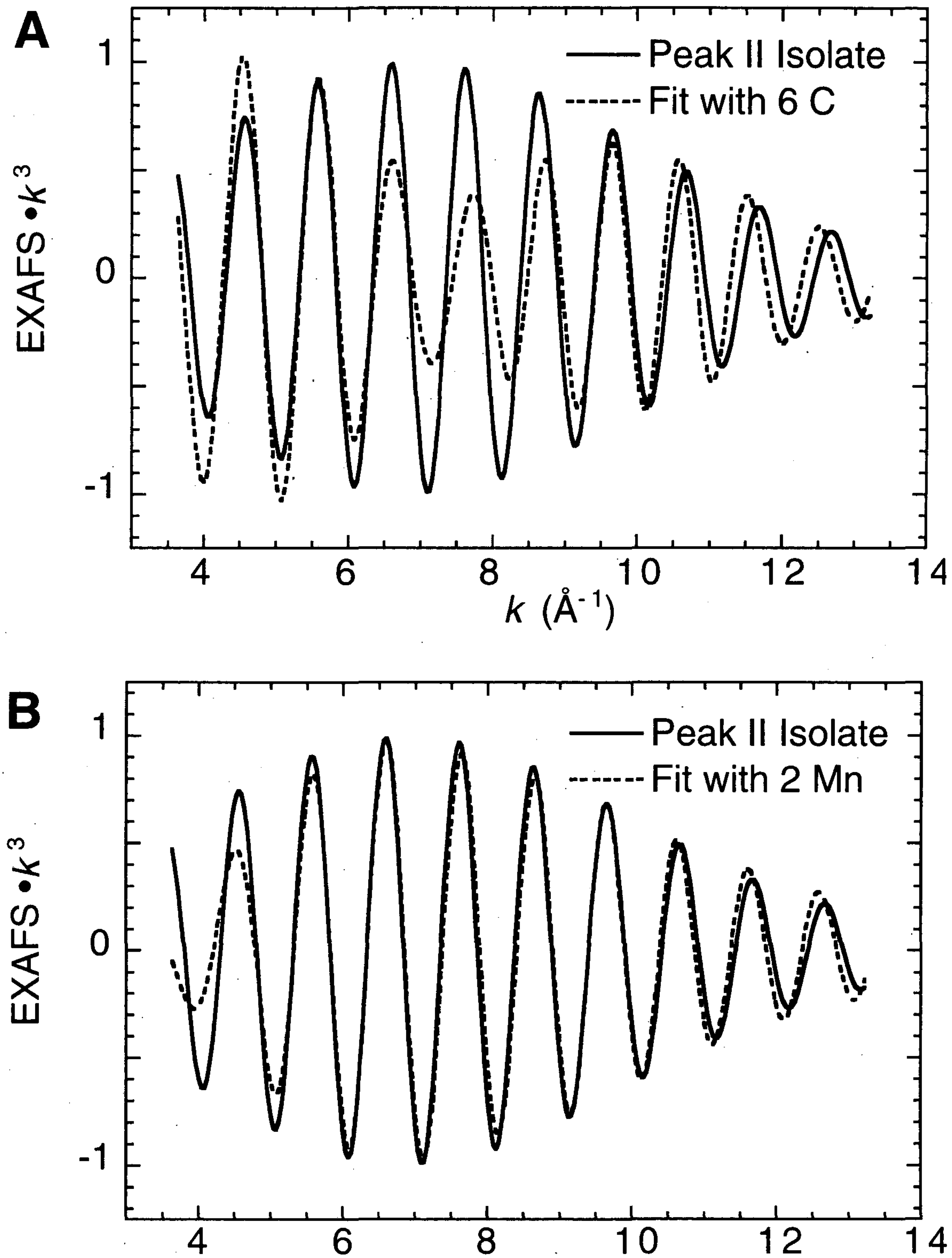
A
Peak II Isolate
Fit with 6 C
EXAFS •k^3
1
0
-1
4
6
8
10
12
14
k (Å^{-1})
B
Peak II Isolate
Fit with 2 Mn
EXAFS •k^3
1
0
-1
4
6
8
10
12
14
k (Å^{-1})

Figure 2.4 Sr EXAFS curve fitting for peak II with C or Mn scatterers. Simulations on Fourier isolates of peak II (k = 3.7 – 13.0 Å^{-1}) were done using FEFF 5.05 theoretical phases and amplitudes, and minimizing the error sum (Φ) using a non-linear least squares method, while varying these parameters for each shell of scatterers: R, σ^2 and ΔE_0. The coordination number N was then fixed at the best fit integer value, giving a number of free parameters p = 3 (Equation 2.7). Peak II experimental data (Fourier-filtered isolate) is shown as the solid line, while the fit result is the dashed line. (**A**) When carbon (from carboxylates) was simulated as a neighbor of Sr, the fit quality was visibly poor in the middle of the k-range, with mismatched amplitudes and phases. (**B**) Improvement of the fit required Mn neighbors at a distance of ~3.5 Å. For Mn simulations, N was fixed at integral values between 1 and 4. A coordination number of two Mn was found to best account for the data for most of the k-range (k = 5 – 11 Å^{-1}). Adding more shells did not significantly improve the fit quality but instead resulted in an underdetermined fit. Simulations using other low-Z atoms (O, S, P, Cl) were tried and all fit worse than Mn.

Simulations with other low-Z atoms (O, P, S, Cl — Table 2.2) all resulted in poorer fit quality, both visibly and in Φ. Other values for N_{Mn} were tried, such as 1 or 3 with mixed outcomes. An inadequate fit was obtained using $N = 1$ (Figure 2.5A) whereas $N = 3$ (Figure 2.5B) gave a simulation that was visually comparable to $N = 2$. Relative to $N = 2$, the improvement in fit error in going from $N = 2$ to 3 (2%) was not so dramatic as from 1 to 2 (160%). The $N = 3$ fit was accompanied by a large Debye-Waller factor (σ^2, Table 2.2), because N and σ^2 are highly correlated. Two-shell simulations have been attempted, but the inclusion of another shell does not improve the fit enough to justify the increased number of free parameters (p in Equation 2.7).

When peaks I and II were isolated together to minimize any possible distortions from Fourier filtering,[62] curve-fitting results (not shown) were consistent with those presented here, although dominated by first-shell scattering from peak I. Multiple-scattering was neglected in this study because it was found to be insignificant unless focusing among metal atoms occurs,[80] which would be unlikely for distances as short as 3.5 Å. One theoretical EXAFS study found multiple-scattering to be negligible in Photosystem II, around $R \sim 3.5$ Å.[93] The one-shell model used here was a simplified one that accounted for most of peak II. Other shells of scatterers such as C may be present, but the disordered nature of the likely ligand environments at these distances minimized their overall contribution to the EXAFS.

Table 2.2 Sr EXAFS Fitting Results for peak II

Scatterer	R (Å)	N	σ^2 (Å^2)	ΔE_0 (eV)	$\Phi \bullet 10^3$	$\varepsilon^2 \bullet 10^5$
Mn	3.55	2.0	0.0078	2.73	0.402	0.297
Mn	3.55	1.0	0.0042	1.74	1.052	0.778
Mn	3.56	3.0	0.0108	3.48	0.394	0.291
C	3.59	6.0	0.0056	2.94	1.680	1.242
O	3.56	4.0	0.0044	8.12	0.667	0.495
P	3.68	4.0	0.0082	-4.49	1.017	0.752
S	3.68	4.0	0.0089	-1.46	0.951	0.703
Cl	3.66	3.0	0.0074	-0.40	0.831	0.615

Fitting parameters are as defined in the text. S_0^2= 0.85 for all fits. The first four results are plotted in Figure 4A-B and 5A-B (N_{Mn} = 2, N_C = 6, N_{Mn} = 1, N_{Mn} = 3). The coordination number N was fixed to integer values for Mn and to best fit integral values for the light atom scatterers. The goodness-of-fit values are as defined in the text. The k-space data range for the fit was from 3.7 - 13.0 Å^{-1} and the window width for the Fourier filter was 1.00 Å.

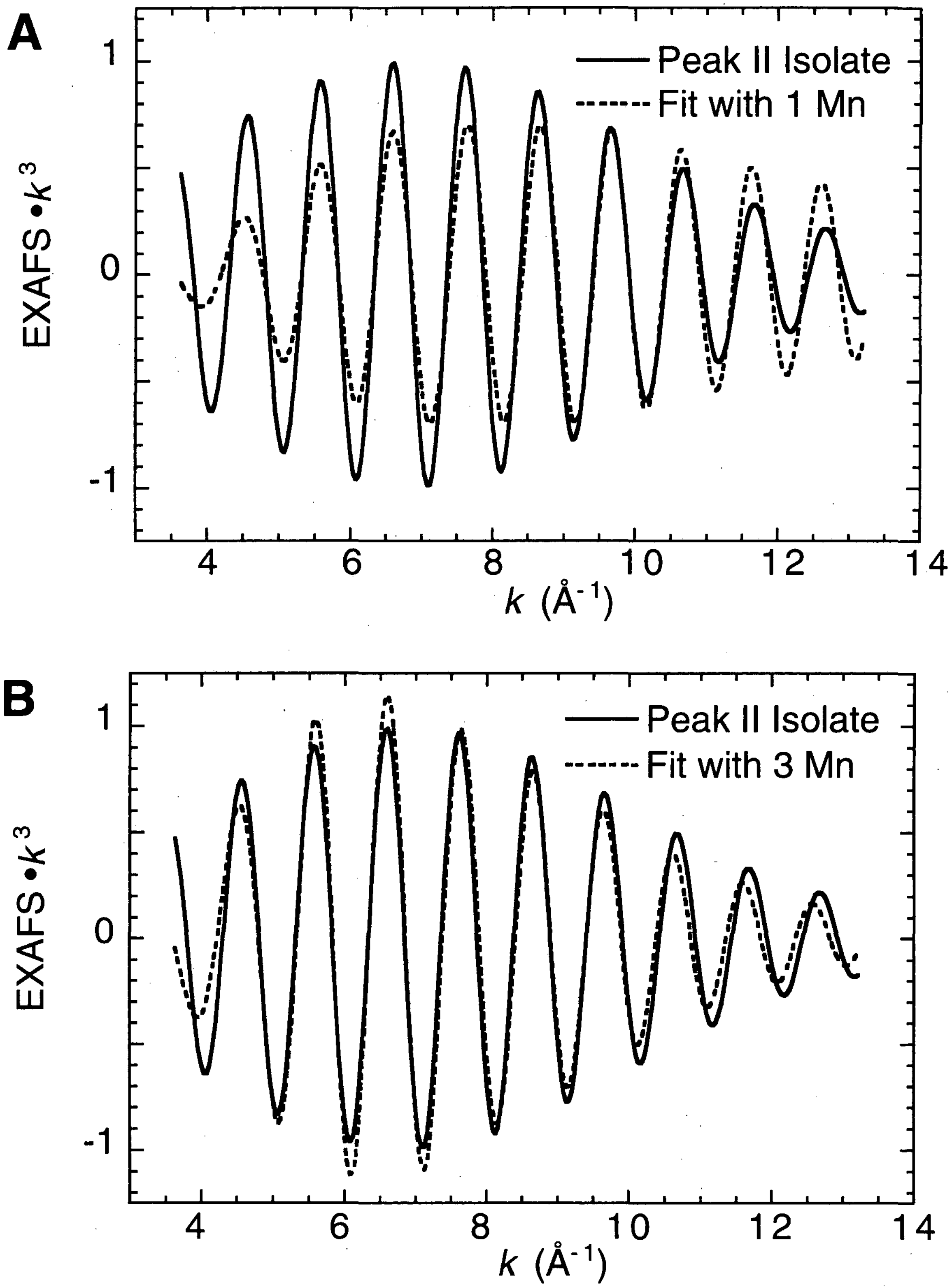
A
Peak II Isolate
Fit with 1 Mn
EXAFS •k^3
1
0
-1
4
6
8
10
12
14
k (Å^{-1})
B
Peak II Isolate
Fit with 3 Mn
EXAFS •k^3
1
0
-1
4
6
8
10
12
14
k (Å^{-1})

Figure 2.5 Sr EXAFS curve fitting for peak II with Mn scatterers. Experimental data (peak II isolate, k = 3.7 – 13.0 Å^{-1}) is the solid line, and the simulation is dashed line. (**A**) When N_{Mn} was fixed to 1, the fit was inadequate to describe the data throughout the k-range. (**B**) When N_{Mn} was fixed to 3, the fit improved only slightly (compared to $N_{\mathrm{Mn}} = 2$) by exceeding the original data at the range k = 5 – 7 Å^{-1}.

Discussion

The aim of this study, a novel use of EXAFS to probe Sr in biological systems, was to investigate the calcium cofactor binding site in PS II and address its proximity to the catalytic Mn cluster of the oxygen-evolving complex. To prepare samples for this study, the low pH/citrate protocol was used to deplete Ca so that Sr could be substituted, resulting in the lower enzyme activity (40%) and the altered multiline EPR signal. Chelex treatment then removed excess, weakly bound and adventitious Sr ions, leaving only the functioning cofactor intact, as shown by the continued oxygen activity and metals quantitation (~1 Sr / 4 Mn). We also acquired the Mn K-edge and EXAFS spectra for one Sr-PS II sample (S_1 state, Appendix 2). Its K-edge spectrum resembles normal PS II in the S_1 state[19,46] and its Fourier transform contains the customary three major peaks that are consistently observed from PS II samples (Appendix 2).[16,21,46] Although the current study is based on Sr EXAFS, this result further assures us that the Mn-containing centers are intact and not significantly damaged during the biochemical treatments. The biochemical and spectroscopic characterization shows that Sr has successfully replaced the original cofactor. The Sr-PS II samples, along with inactive Sr-PS II (prepared by adding NH_2OH to disrupt the intact samples) were then examined by Sr EXAFS techniques.

The Fourier transforms of the Sr EXAFS from intact Sr-PS II samples show an interaction (peak II) that is best modeled by two Mn at 3.5 Å distance. This vector is not present in the inactive, NH_2OH-treated set, although both types share similar first coordination shells of oxygen (peak I, Fig. 2.3). Attempting to model peak II with C (the most likely low-Z candidate, from carboxylate ligands) results in a decidedly worse fit (Fig. 2.4A). Other nonmetallic low-Z atoms (O, P, S, Cl - Table 2.2) also produce poor simulations compared to Mn, and so by extensive fitting trials we have excluded light atoms as major contributors to Fourier peak II. These simulations present Mn as the chemically reasonable alternative. Strictly speaking, the EXAFS method cannot distinguish between scatterers of adjacent Z, so iron could also account for peak II. However, the other supporting data (biochemical studies, oxygen-evolving activity, EPR, and previous Mn EXAFS studies[46]) point to Mn is the likely candidate rather than Fe.

The coordination number for Mn that best fits the data is between 2 and 3 (Figs. 2.4B, 2.5B), but for several reasons, we favor the lower number. Relative to $N = 2$, the improvement in Φ from $N = 2$ to 3 is slight (2%) compared to that from $N = 1$ to 2 (160%). Visual comparison of Fig. 2.4B with 2.5B reveals that, in the ranges $k \sim 5.5 - 7$ Å^{-1} and $k \sim 9.5 - 12$ Å^{-1}, $N = 2$ simulates the data more closely. Preliminary studies of the polarized Sr EXAFS from oriented Sr-PS II multilayers also show dichroism patterns that are inconsistent with $N = 3$ (Chapter 3).

The absence of peak II in the inactive Sr-PS II samples is consistent with the interpretation that NH_2OH disrupts the Mn cluster[64,88] and alters the Mn from its native 3.5 Å configuration. This harsh treatment may disrupt the Sr (Ca) binding site, release the cofactor and ensure that there is no Mn nearby (within 4 Å). We believe that the NH_2OH treatment provides the best control sample for this experiment, as there is no known method to "surgically" extract the Mn cluster while leaving the cofactor unperturbed. Because no washing steps are done with the NH_2OH-treated Sr-PS II, the Sr amount in the macroscopic sample remains identical to that of the intact Sr-PS II, and the general protein matrix is retained.

The Sr EXAFS results, translated back to the original cofactor, support the earlier conclusion that Ca (Sr) is near the Mn cluster[46] at a distance of ~3.4 - 3.5 Å. Ca^{2+} has a slightly smaller radius than Sr^{2+} (by about 0.1 Å).[92] A new result from this study is that $N_{Mn} = 2$, indicating two Sr–Mn interactions, whereas the earlier Mn EXAFS study proposed one Mn–Ca (Sr) interaction. The discrepancy could ensue from the increased complexity of the Mn EXAFS signal, which is the average of contributions from the four different Mn. With each Mn having its own local environment of scatterers, especially at long distances, precise determination of N for the Ca (Sr) cofactor becomes difficult. Adding to the complication is the Mn–Mn interaction (at 3.3 Å)[16,24,94] that is probably also present in the same region ('R'~ 3 Å). The conclusion based on Sr EXAFS is more compelling because there is only one Sr per functioning catalytic center so that its signal is neither diluted nor averaged.

For our fitting routines, we have used a simplified model involving only one shell of scatterer (Mn favored over C) to account for the long-distance interaction at 3.5 Å. This model relies on the observation that backscattering for light atoms such as C or O is probably insignificant at distances around 3.5 Å, based on EXAFS studies on complex crystalline solids.[80] There may be C scatterers present, but they are not EXAFS-detectable at these long distances because of disorder or low backscattering amplitude. By using only one shell, we avoid an underdetermined fit where the information content of the EXAFS data does not justify the large number of adjustable parameters.

The distance of ~ 3.5 Å for the Sr–Mn vector indicates the presence of a single-atom bridge, likely to be oxygen.[49] This bridge may be derived from carboxylate ligands (aspartate or glutamate protein residues), protein backbone carboxyl, water or hydroxide. This finding of a short metal–metal interaction is unprecedented for calcium-containing metalloenzymes. As discussed in an earlier study,[46] examination of calcium-binding sites in proteins and calcium complexes shows that carboxylate bridging (involving both O atoms) between two metal centers produces distances[95] of 3.8 - 4.3 Å, as seen in thermolysin (double Ca binding site with three bridges) and concanavalin A (Ca–Mn site with one bridge). However, in complexes where two Ca are bridged by lone oxygen atoms from two carboxylates, shorter distances (~ 3.6 Å) result.[46] A polyether carboxylate complex has two single-O-atom carboxylate bridges that bring two Ca to within 3.9 Å.[96] Because Ca–O bonds are normally 2.45 Å[92] and Mn–O distances range from 1.75 - 1.9 Å[97], replacing one Ca with a high-valent Mn (III or IV) in these bridged Ca complexes would yield a Mn–Ca distance that approaches the value found in our study (~3.5 Å). This assumes a Ca–O–Mn angle of 106° as found in the synthesized compounds.[96] Single-O-atom bridges also help to achieve a short (3.4 Å) Sr–Ti distance in the perovskite compound $SrTiO_3$.[54] Because Ti^{4+} has a radius almost identical to that of Mn^{3+} (0.68 and 0.66 Å, respectively), if Ti were substituted with Mn the distance would resemble the observed value from Sr EXAFS of PS II. In mixed carboxylate/catecholate complexes that contain Mn_4LaCl and Mn_4Tb clusters, single-O-atom bridges combine to yield Mn–La and Mn–Tb distances of 3.5 and 3.2 Å, respectively.[98] The lanthanides were chosen because the ionic radii for La^{3+} (1.03 Å) and Tb^{3+} (0.92 Å) are similar to that for Ca^{2+} (1.00 Å).[92] Finally, a Mn^{III}-Schiff base complex features a manganese-sodium interaction, bridged by one acetate and O atoms from two phenolate groups.[99] With the Mn–Na distance of 3.3 Å, this complex has relevance because the ionic radius of Na^+ (1.02 Å)[100] nearly equals that of Ca^{2+}. Compared to motifs found in relevant synthesized complexes, our results are compatible with the presence of single-O-atom bridging (oxygen) between the Mn and Ca (Sr) cofactor to achieve the relatively short ~3.5 Å vector.

A model of the OEC that is topologically consistent with the new findings is presented in Fig. 2.6, which incorporates two Mn–Ca interactions at ~ 3.4 – 3.5 Å distance and single-O-atom bridging. For simplicity, other ligands or bridges that may be present are not depicted. This model represents one configuration, with Ca spanning the "open" end of the Mn cluster, although other modes of placing Ca between two Mn are possible (such as Ca spanning the "closed" end or extending across the top or bottom Mn pairs). Further studies to place constraints on the geometry and relative orientation of the Mn–Ca (Sr) vectors will rely on X-ray absorption linear dichroism[21,22,24,101,102] to target Fourier peak II from the Sr EXAFS. To provide further refinement of the proposed model, polarized Sr EXAFS experiments on oriented Sr-PS II multilayers are in progress.

The intimate link between Ca and Mn that had been suggested in previous studies has led to the description of the catalytic center of the OEC as a "tetra-Mn/Ca cluster".[103] The present study provides concrete evidence to reinforce this concept, now that the EXAFS technique extended to strontium in biological samples has confirmed the proximity of Ca to the Mn cluster. Moreover, this approach holds promise for probing the role of the Ca cofactor in the mechanism of oxygen evolution.

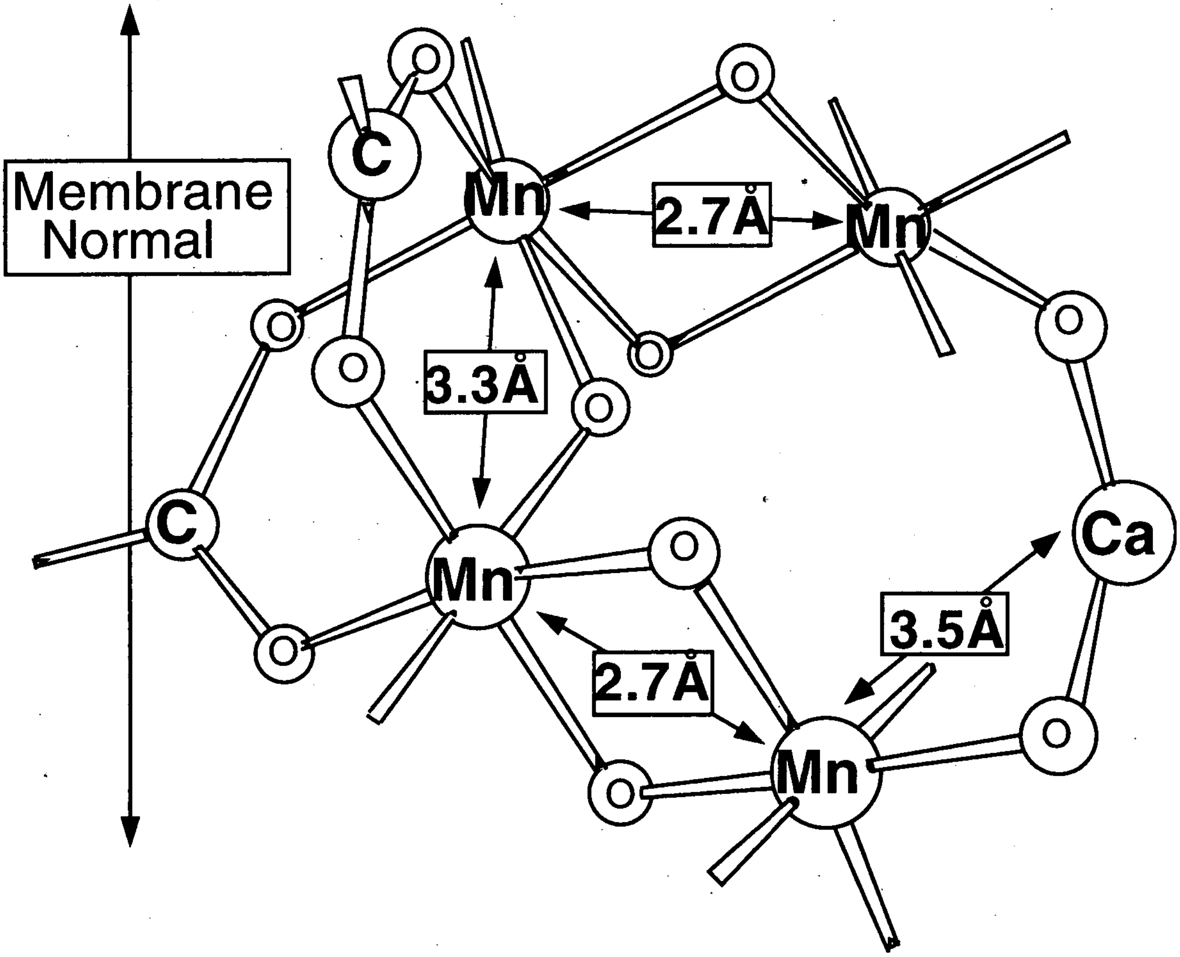

Figure 2.6 Proposed model for the active site of the oxygen-evolving complex (OEC) in PS II. The model incorporates the finding from the Sr-substituted PS II studies: Sr (and therefore Ca) is intimately linked to the Mn cluster at distance of ~ 3.4 – 3.5 Å. This linkage requires single-atom (oxygen) bridging that can derive from acidic protein residues (aspartate or glutamate), hydroxide or water. Depicted is one simple configuration consistent with the findings of the Sr EXAFS study; other topologies having two Mn–Ca interactions are possible. It does not explicitly account for the angular information about the Mn–Mn vectors, found from polarized Mn EXAFS studies,[21,22] and not all ligands to Mn and Ca are specified. Adapted from an earlier report.[46] Copyright 1995 American Chemical Society.

Chapter 3 — Orientation of the Calcium Cofactor in Oxygen Evolution Probed by Polarized Strontium EXAFS on Layered Photosystem II Membranes

Introduction

Calcium is an essential cofactor for photosynthetic oxygen evolution in green plants and algae.[3,9,27] Without it and another cofactor, chloride,[10] the oxygen-evolving complex (OEC) cannot catalyze the oxidation of water into dioxygen, protons and electrons. The OEC consists of a tetranuclear manganese cluster[3,11,13], that ultimately supplies reducing equivalents to the photooxidized reaction center chlorophyll (P_{680}) through a redox-active tyrosine Y_Z.[12,104-106] The one-electron photooxidation of P_{680} drives the OEC through a cycle of five intermediates S_i (i = 0-4),[14,15] where the four oxidizing equivalents are stored before water is finally oxidized into oxygen, four electrons and protons. Calcium is needed for the OEC to advance to the S_3 state and subsequent oxygen evolution. The involvement and role of manganese in photosynthesis have been extensively studied using a battery of biochemical, spectroscopic and kinetic tools.[11,107-109] Without the benefit of suitable crystals for high-resolution x-ray crystallography,[110,111] x-ray absorption spectroscopy (XAS)[7,25,59,61] and electron paramagnetic resonance (EPR)[112-114] studies have emerged as the primary methods to provide structural and chemical information about the OEC and devise a working model for its manganese cluster. Because these methods are element-specific and sensitive at dilute concentrations, x-ray absorption near-edge structure (XANES)[19,20,115] and extended x-ray absorption fine structure (EXAFS)[22-25,46] analyses have been applied at the Mn K-edge to determine oxidation states and information about the local environment of the Mn atoms.

In comparison, there have been fewer spectroscopic investigations of the calcium cofactor.[3,9] Most studies on Ca in PS II have been biochemical,[45,77,103] because Ca has no easy spectroscopic handles, and have shown that depleting Ca by low-pH citrate treatment[32] or 1-2 M NaCl wash[30,116] suppresses oxygen evolution. Replenishing with Ca^{2+} restores catalytic oxygen activity (up to 95%)[29,117] whereas strontium can reactivate centers only up to 40%.[29,30] The smaller rate is due to slower kinetics, because the rate is higher (85%) at limiting light intensity (see Appendix 1).[30,35] No other metal ion has been shown to restore activity in Ca-depleted centers. Besides the lower level of recovered oxygen activity (40%), Sr substitution for Ca induces an altered S_2 state EPR multiline signal (MLS) with slightly narrower hyperfine splitting, and shifts of the different lines.[30,36-38]

The structure of the Ca cofactor binding site has caused some dispute and generated discussion. To probe it, the most common approach was to substitute other metals (such as Sr) for calcium and then use Mn EXAFS to detect changes in the cluster. The first Mn EXAFS study on Sr-reactivated PS II membranes was interpreted to indicate a 3.4 – 3.5 Å distance between the Sr (and therefore Ca) and the Mn cluster.[46] This relatively short distance was supported by FTIR spectroscopic evidence consistent with a carboxylate bridge between Mn and Ca.[48,118] A slightly longer distance (3.6 – 3.7 Å) was deduced from a Mn EXAFS study on NaCl-washed PS II membrane preparations.[49] In contrast, another Mn EXAFS study found no detectable evidence for such an interaction within 4 Å of the Mn.[51] Other studies such as Mn EXAFS on terbium-substituted[52] PS II and EPR experiments on Mn^{2+}-substituted samples[53] seemed to support this view that the Ca binding site is at least 4 Å away from the Mn.

Recently we have used strontium EXAFS experiments to probe the cofactor itself for any nearby Mn.[119] This approach differed fundamentally from the previous studies focusing on Mn. By using Sr EXAFS on isotropic Sr-reactivated PS II membranes, we have confirmed the proximity of Sr (and implicitly Ca) to within 3.5 Å of the Mn cluster.[119] The finding was based on the presence of a second Fourier peak in the Sr EXAFS from functional samples, a peak that is absent from inactive, hydroxylamine-treated PS II. This peak II was found to fit best to Mn rather than lighter atoms (carbon).

As an extension of this current approach, polarized Sr EXAFS studies on oriented Sr-reactivated PS II have shown that this Fourier peak II is dichroic: within the range of angles (θ, between PS II membrane normal and the x-ray electric field vector) examined, peak II magnitude was largest at 10° and smallest at 80°.[120] Analysis of this dichroism provides more information on the location of the Ca cofactor binding site. Conventional EXAFS can provide the absorber–backscatterer distance and the number and identity of scatterers up to second or third coordination sphere, but typically cannot give information about angles.[78] However when applied to oriented samples such as membrane multilayers this method can furnish additional angular information. X-ray absorption linear dichroism spectroscopy applies linearly polarized synchrotron radiation to partially ordered molecular systems with a preferred orientation along at least one sample coordinate axis.[101,121] Specifically, polarized EXAFS has been applied to PS II multilayers that possess an effective membrane normal.[21,22,24,101,102,122]

If we collect EXAFS spectra for oriented samples we can extract the relative orientation of the absorber–backscatterer (A–B) vector of interest. Depending on how the A–B vector is aligned with the electric field (as measured by the angle β), the vector of interest may show dichroism in the EXAFS and Fourier transform, roughly following a $\cos^2\beta$ relation.[101] When PS II membranes are carefully layered on flat films, a preferred orientation arises with the membranes parallel to the underlying substrate plane. Polarized EXAFS involves collecting EXAFS spectra for different incident angles (θ) between the membrane normal and the x-ray electric field vector. Dichroism in the EXAFS occurs depending on how the particular A–B vector is aligned with the electric field. Through analysis of the dichroism, we extract the average orientation (ϕ) of this A–B vector relative to the membrane normal, and the average number of scatterers (N_{iso}). Constraints on the structural model are imposed by these parameters, highlighting the advantage of polarized EXAFS on layered samples, over randomly oriented membranes.

To date, polarized EXAFS studies on PS II have concentrated on the Mn–Mn vectors[21,22,24,102,122] and have produced valuable insights into the relative angles of the ~ 2.7 Å and ~ 3.3 Å Mn–Mn vectors.[21,22] Previous research on native and NH_3-treated PS II revealed angles of 55° and 67° for the two 2.7 Å vectors, and ~ 30° for the 3.3 Å vector. By contrast, the present study details work on using polarized Sr EXAFS on (partially) ordered Sr-reactivated PS II to find the relative orientation of the calcium cofactor involved in oxygen-evolution. The results further bolster the contention that Ca (Sr) is proximal to the Mn cluster and allow us to refine the working model of the oxygen-evolving complex in PS II.

Experimental Section

Sample Preparation

Sr^{2+}-substituted PS II samples were made by a process of Ca depletion by low-pH treatment,[32,68,69] Sr^{2+} reactivation,[30] and Chelex treatment to remove excess Sr.[42,72] These steps have been described in detail previously[119] (see Chapter 2) and were carried out in the dark at 4°C. The samples were assayed for enzyme activity, EPR multiline signal generation (from the S_2 state) and metals quantitation (Mn and Sr from inductively coupled plasma - atomic emission spectroscopy, ICP-AES). After the final Chelex treatment to remove non-essential Sr^{2+}, the samples were placed in a SS34 rotor (Sorvall Instruments) and centrifuged (Model RC5B, Sorvall Instruments) for 15 min. at 40000*g* in sucrose buffer (0.4 M sucrose, 30 mM NaCl, 50 mM MES, 5 mM $MgCl_2$ and 2.5% ethanol at pH 6.5). The resulting pellet was then painted onto flat Mylar films, supported by a Plexiglas frame, and dried under a stream of dinitrogen at 4°C. Repeated cycles (6-7) of painting and drying took 18-20 h to build up a sufficient amount of PS II (2 - 3 mg Chl).[21,22] After the last layer had dried, a razor blade cleaned the sides of the sample holders of excess PS II then the samples were frozen in liquid nitrogen for storage. Oxygen evolution assays were conducted on samples before the painting process, as mentioned earlier.[119]

Metals Quantitation

PS II samples (1 - 3 mg Chl) were first digested in 3 ml of boiling, concentrated ultra pure HNO_3 (TracePur plus, EM Science), then diluted to 10 mL with deionized water. Elemental analysis of Mn and Sr in the ppb range were carried out at the Microanalytical Lab in the U. C. Berkeley College of Chemistry using inductively coupled plasma and atomic emission spectroscopy (ICP-AES). The amounts of PS II per sample were calculated from the chlorophyll assays, assuming 200 Chl per PS II.[41,42,77]

EPR Spectroscopy

X-band (9.2 GHz) EPR spectra were acquired on layered Sr-PS II on Mylar films, using a Varian E-109 system, a standard TE102 cavity and a Helitran liquid helium cryostat (Air Products). Low temperature (8 K) spectra were used to monitor EPR-detectable Mn^{2+} on isotropic and layered samples before and after exposure to x-rays. The Ca- and Sr-treated, untreated (native) and layered samples were poised in the S_2 state by illumination for 8 min at 200 K (solid CO_2/ethanol bath) using a 400 W tungsten lamp (General Electric) and an aqueous $CuSO_4$ filter (5% w/v, 7 cm path). Difference (light-minus-dark) EPR spectra were used to characterize the extent of Sr-substitution and the turnover of the OEC in pelleted (Sr- and Ca-reactivated) and layered Sr-reactivated samples.

Mosaic Spread Determination by EPR

The paint-and-dry cycles produce samples with a preferred orientation of the PS II membrane normal perpendicular to the substrate surface: an imperfect one-dimensional order. The disorder or mosaic spread[123,124] can be due to several factors: imperfect stacking of the membranes on the substrate film, disorder of PS II proteins within the membranes, or disorder of the OEC within the PS II proteins. There is no way to assign the contribution of each factor to the total mosaic spread. The extent of orientation can be assessed from the angle dependence of the EPR Signal II_s from tyrosine Y_D^{ox}.[112,125-127] X-band (9.2 GHz) EPR spectra of the Signal II region ($g = 2.00$ or 3240 – 3340 G) were taken for layered samples oriented 0° and 90° in the magnetic field at

20 K and 50 μW power with 2.5 G modulation amplitude. The sample face was aligned parallel (0°) or perpendicular (90°) to the external magnetic field. The dichroic ratio (here, amplitude at 90° divided by that at 0°) was taken at the ~ 3260 G. This dichroic ratio ("Signal II ratio") was related to the dichroism in the cytochrome b_{559} EPR signal[21,22,112,124,125,128] to obtain the mosaic spread, or half-width of the Gaussian distribution of a particular vector in PS II samples.[126] In previous work from this laboratory,[126] a calibration line has been constructed, which equates mosaic spread to a measured Signal II ratio. Thus, from the Signal II ratio, we can estimate the degree of disorder inherent in the layered samples. The estimate is crucial because the disorder affects the observed dichroism in the EXAFS spectra.

EXAFS Data Collection

Conditions for acquiring Sr EXAFS data on oriented Sr-PS II samples closely resembled those for isotropic samples and have been detailed before.[119] At the Stanford Synchrotron Radiation Laboratory (SSRL), EXAFS at the Sr K-edge (16 - 17 keV) were collected on Sr-PS II multilayers at various excitation angles (θ, angle between the x-ray **e** field vector and the substrate normal): 10°, 30°, 45°, 70°, and 80°.[21,22] A Si(220) double crystal monochromator was used at the wiggler Beamline VII-3 (unfocused mode) along with a 13-element energy-resolving Ge detector (Canberra Instruments). Samples were kept at a temperature of 10 K in a liquid helium flow cryostat to minimize radiation damage. Six separate samples were used, with at least two angles per sample, for a total of 15. Twenty-five to fifty 15-min. scans (depending on θ) were necessary for signal averaging on each sample to reduce noise to a sufficiently low level. As a check for sample integrity after Sr substitution and layering treatments, Mn EXAFS data were also collected for comparison with normal, intact PS II spectra from previous experiments.[46]

EXAFS Data Analysis

Data reduction has been recounted previously[119] (see Chapter 2) and will be only briefly summarized. After conversion of background-corrected spectra from energy space to photoelectron wave vector (k) space, and weighting by k^3, a five-domain spline was subtracted for a final background removal. The k-space EXAFS was truncated near the zero crossings (k = 2.7 - 11.8 Å^{-1}) before the Fourier transform. The region around 'R' = 3.0 Å, peak II, was Fourier-isolated using a Hanning window applied to the first and last 15% of the range (ΔR = 0.9 Å), while not affecting the middle 70%. The back-transformed (k-space) peak II was simulated with a Sr–Mn interaction, similar to the isotropic Sr EXAFS protocol[119] (Chapter 2) using *ab initio* phase and amplitude functions calculated from the program FEFF 7.[82,83] Curve-fitting was done by minimizing the error sum (Φ) using a nonlinear least-squares protocol while varying these parameters for the Sr–Mn shell: R, $N_{apparent}$, and ΔE_0. The Debye-Waller factor (σ^2) was fixed to the best all-around value. For each sample, we compiled a table of the detection angle θ, distance R, apparent coordination number N_{app} and ΔE_0.

Theory of Polarized EXAFS

To analyze the x-ray absorption linear dichroism of the Sr EXAFS and find the relative orientation of the vector of interest (ϕ), we used the formalism of Dau et al.[121,122] Although it differs somewhat from the previous studies,[21,22,24,101,102] this approach is nevertheless valid and both methods produce comparable results. To a first approximation, the angle dependence of the EXAFS is proportional to $\cos^2(\theta_{\mathrm{ER}})$, with θ_{ER} being the angle between the x-ray electric field vector (**E**) and the absorber–scatterer vector (**R**, see Figure 3.1). In turn, θ_{ER} is composed of the measurement angle θ and the angle ϕ between **R** and **M**. Because of the rotational symmetry of the layered membranes, the angle ϕ defines a cone around the membrane normal **M**. When membranes are layered on a flat substrate, the preferential orientation of **M** is parallel to the underlying substrate normal (**S**). For these imperfectly stacked sheets, the probability (P_α) of finding an angle α between **M** and **S** is the product of $\sin\alpha$ and the order function $P_{ord}(\alpha)$, which is maximum at $\alpha = 0°$. $P_{ord}(\alpha)$ is best approximated by a Gaussian distribution whose half-width is denoted as the mosaic spread (Ω) or disorder angle.[121,122] Here we assume that the mosaic spread accounts for the disorder between the membrane normal and substrate normal, while the spread of **R** relative to **M** is negligible. For an ensemble of A–B vectors (**R**), the magnitude of the EXAFS is related to the P_α-weighted integration over all possible orientations of **M** (α- and β-integration) and along the cone of possible directions of **R** (γ-integration). The N_{app} found from EXAFS curve-fitting on an oriented sample at a particular θ is related to the coordination number of an isotropic sample N_{iso} by the following equation:

$$N_{app}(\theta) = N_{iso} + \frac{1}{2} N_{iso}(3\cos^2\theta - 1)\cdot(3\cos^2\phi - 1)\cdot I_{ord} \tag{3.1}$$

where I_{ord} is the order integral (Equation 3.2):

$$I_{ord} = \frac{1}{2}\frac{\int_0^{\pi/2} \sin\alpha\cdot(3\cos^2\alpha - 1)\cdot\exp(-\alpha^2\ln 2/\Omega^2)d\alpha}{\int_0^{\pi/2}\sin\alpha\cdot\exp(-\alpha^2\ln 2/\Omega^2)d\alpha} \tag{3.2}$$

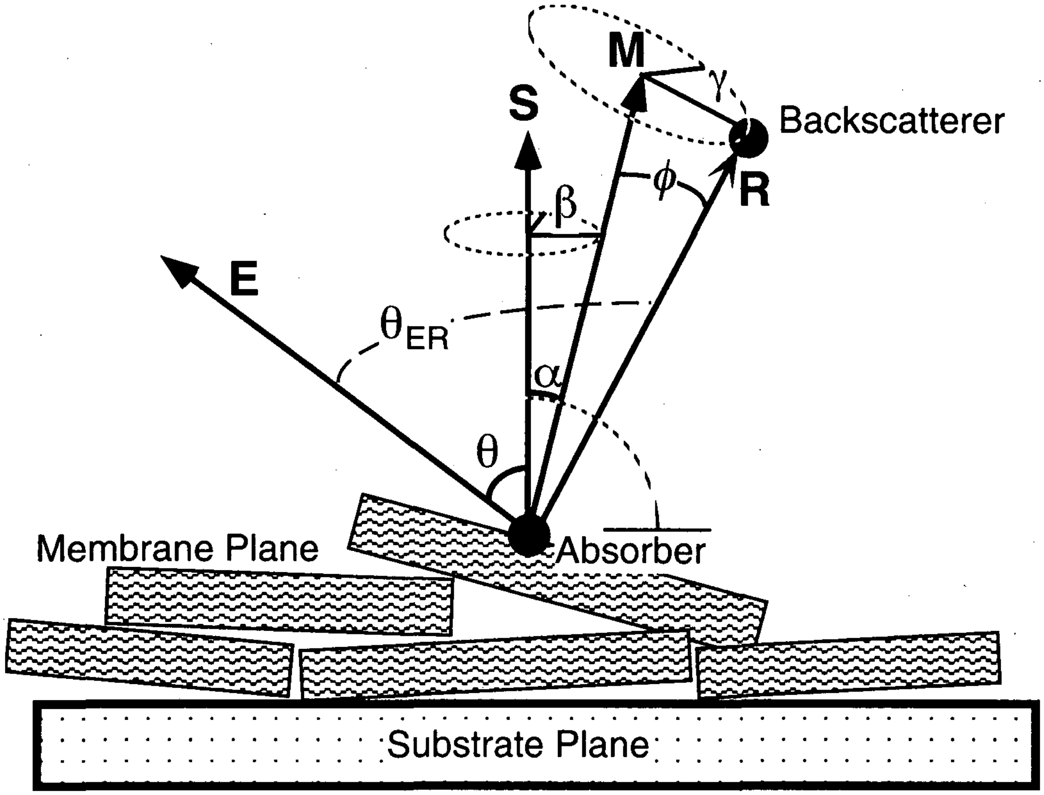
M
γ
S
Backscatterer
φ
R
β
E
θER
α
θ
Membrane Plane
Absorber
Substrate Plane

Figure 3.1 Scheme (side view) for the vectors and angles involved in x-ray absorption linear dichroism for partially oriented membranes on flat substrate. Due to the rotational symmetry of the layered samples, the orientation of **R** (defined by the angle ϕ) is described by a cone around the membrane normal **M**.

By fitting the θ-dependence of N_{app} by nonlinear regression analysis, we extract the average relative orientation ϕ and N_{iso}. Eq. 3.1 was implemented numerically by a Mathematica 3.0 program[129] (Wolfram Research, Inc.) using values for Ω as determined from EPR. Regression analysis of the linear form of Eq. 3.1 (with $x = 3\cos^2\theta - 1$ and $y = N_{app}$) was done with Igor Pro software (version 3.1, WaveMetrics Inc.). As a simulated example, Figure 3.2 shows the calculation of Equation 3.1 for various values of the relative angle ϕ, assuming $N_{iso} = 1$ and $\Omega = 20°$. This polar plot contains the N_{app} as radial values plotted against the excitation angle θ (0 – 360°) and predicts the dichroism of the observed N_{app} for different relative angles of the vector of interest, as ϕ varies from 0° to 90°. Note that at the magic angle ($\phi = 55°$) the observed N_{app} is isotropic for all experimental angles (dashed circle).

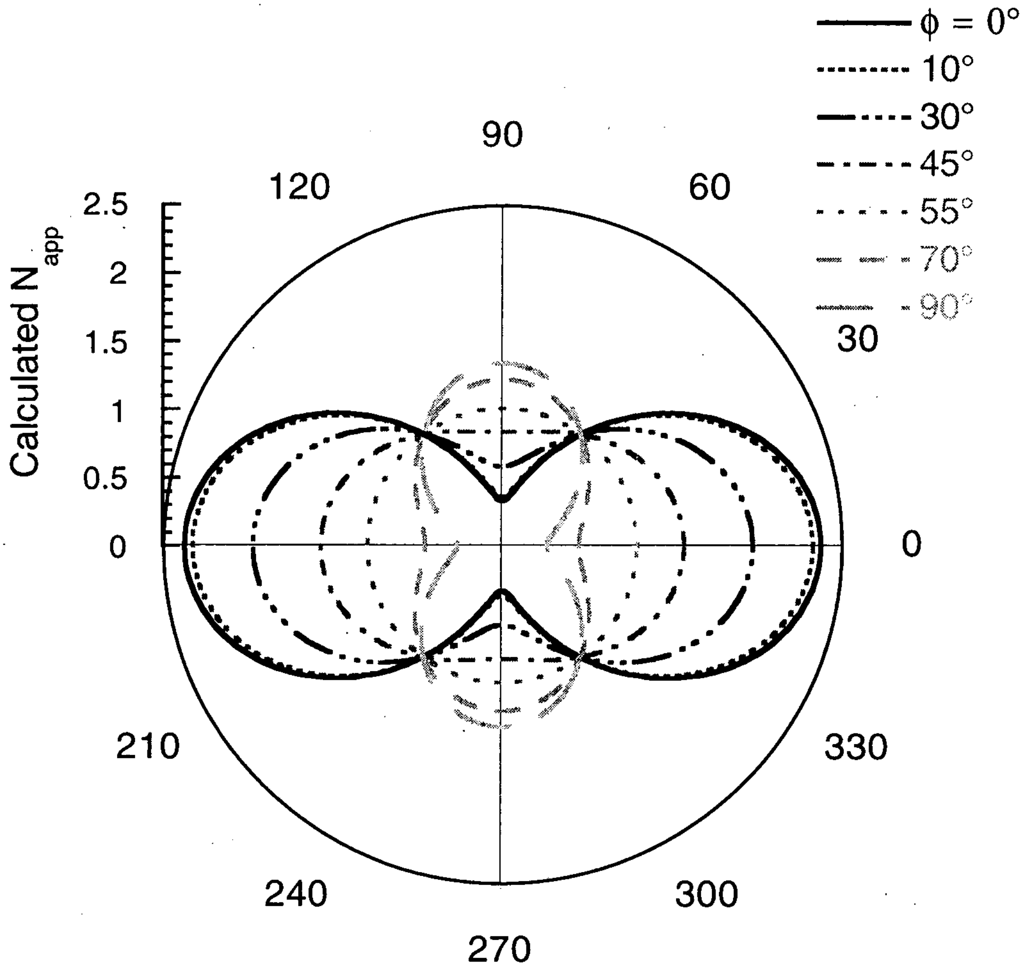

Figure 3.2 Polar plot of calculated EXAFS amplitude (N_{app}) in Eq. 3.1 for various relative angles (ϕ, 0–90°), assuming N_{iso} = 1 and the mosaic spread Ω = 20°. The simulation contains radial values of N_{app}versus the measurement angle θ (0 – 360°).

Results

The characterizations (EPR, O_2 activity, metals content) yielded results similar to those obtained previously.[119] The Sr-substitution was successful as judged from the Sr-altered EPR multiline signal (before the Chelex removal of excess Sr), the reduced level of oxygen evolution (40%) and metal content (~ 0.8 Sr per 4 Mn). No EPR-detectable Mn^{2+} was observed after the layering process.

Mosaic Spread

The tyrosine Y_D^{ox} (Signal II "slow") EPR spectrum[112,125] at two extreme angles (0° and 90°) between the sample face and the applied magnetic field. As Figure 3.3 shows, the dichroic ratio of the ~ 3260 G feature can be measured and compared for the oriented samples. This Signal II ratio is related[126] to the mosaic spread as measured from the angle dependence of the cyt b_{559} EPR spectra, following the protocol of Blum et al.[21,124] Here we assumed a Gaussian distribution for the direction of the membrane normal. The mosaic spread is the half-width of that distribution. A calibration curve was constructed to estimate the mosaic spread from a given Signal II ratio.[126] In the example in Fig. 3.3, this ratio was 4.3 ± 0.5 and yielded $\Omega = 20° \pm 3°$. For the six samples used in this study, the mosaic spread averaged 15° ± 5°.

Polarized Sr EXAFS on Oriented Samples

Figure 3.4 shows the unfiltered, k^3-weighted Sr EXAFS from the Sr-PS II multilayers at the extreme measurement angles (θ). Data from the various angles (10°, 30°, 45°, 70°, 80°) were processed similarly for consistency and to allow for valid comparisons. Two independent sets are shown in Fig. 3.4; these are representative of four other sets, which exhibited similar patterns of

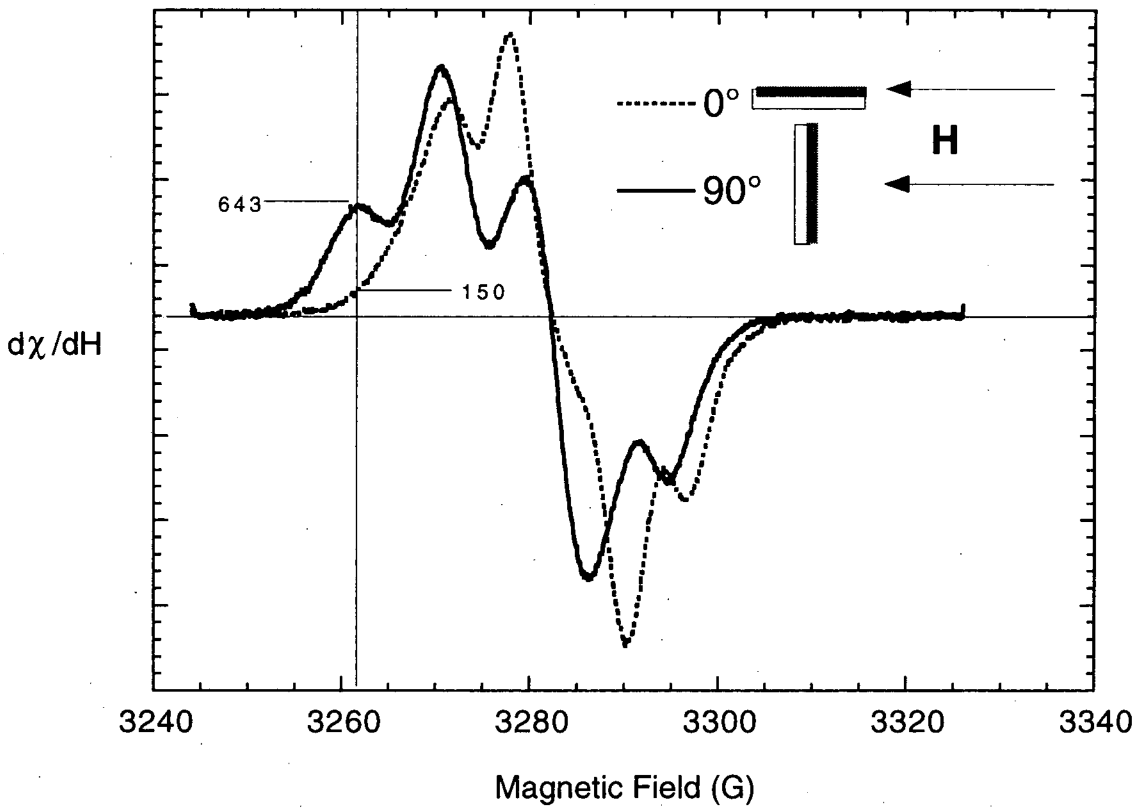

Figure 3.3 EPR Signal II spectrum of layered PS II to estimate mosaic spread. The tyrosine Y_D^{ox} signal shows dichroism, especially at ~ 3260 G depending on the angle between the sample plane and the magnetic field. In this particular sample, the Signal II ratio (net amplitude at 90° divided by that at 0°) is 4.3 ± 0.5, which corresponds to a mosaic spread (Ω) of 20° ± 3°. The error mainly comes from determining the baseline. The legend shows orientation of the layered PS II and its underlying substrate in the applied magnetic field (**H**).

dichroism. In particular, the oscillation at k = 6.6 Å^{-1} is consistently larger in the 10° orientation than at 80°. Also, beyond k = 7.5 Å^{-1}, the 80° oscillations have slightly larger amplitude and become out-of-phase with those at 10°. Consequently, at the more perpendicular angle, the amplitude envelope is roughly even across the k-range, whereas the 10° spectra have a maximum at k = 6.6 Å^{-1}, and decline on either side of this "beat" feature.

Fourier Transform (FT) of Polarized Sr EXAFS

The corresponding Fourier transforms show extreme dichroism in peak II for oriented Sr-substituted samples (Figure 3.5). Within the excitation angles studied, peak II has largest magnitude at θ = 10°, while it is smallest and near the noise level at 80°. For comparison, the Fourier transform of the inactive Sr-PS II is plotted along with those of the 10° and 80° orientations (Figure 3.5A).[120,130] As Fig. 3.5A shows, the 80° orientation is reminiscent of the inactive Sr-PS II where peak II is absent, being either at or below the noise level. This is noteworthy, because for the oriented samples, PS II was found to be active in oxygen evolution before the layering procedure. In contrast, inactive Sr-PS II was treated with hydroxylamine as the sample was prepared, suppressing enzyme activity. Just by measuring the layered samples at θ = 80°, its FT is indistinguishable from that of inactive Sr-PS II. The two FTs shown are representative of four other sets of data, which are consistent both in the dichroism of peak II between 10° and 80°, and in the similarity of the 80° spectra to that of hydroxylamine-treated PS II. As for the 30° and 45° FTs (not shown), their peak II magnitudes are correspondingly smaller than those at 10° but still above those of 80°.

The dichroism in peak I is relatively minor (Fig. 3.5, as measured by relative peak heights at 10° and 80°) compared to that in peak II. The peak I

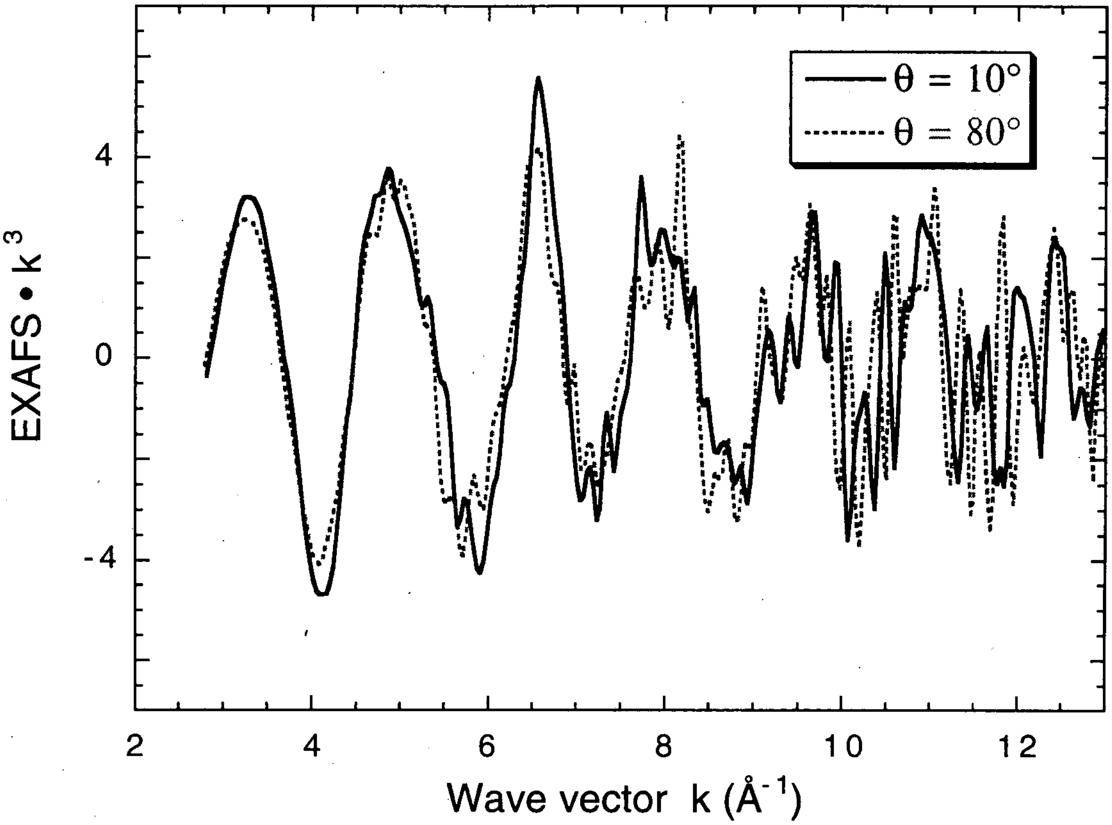
θ = 10°
θ = 80°
EXAFS • k^3
4
0
-4
2
4
6
8
10
12
Wave vector k (Å^{-1})

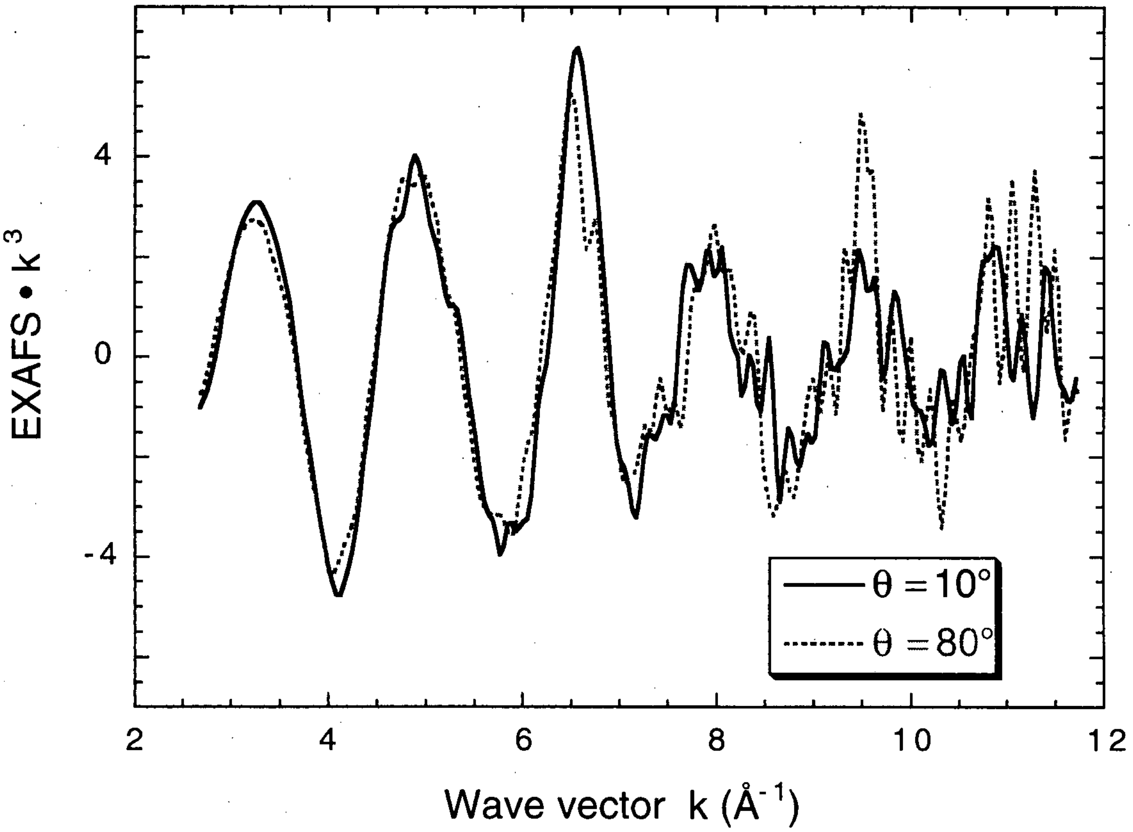
EXAFS • k^3
4
0
-4
θ = 10°
θ = 80°
2
4
6
8
10
12
Wave vector k (Å^{-1})

Figure 3.4 k^3-weighted Sr EXAFS of oriented Sr-PS II membranes at two extreme measurement angles (θ) for two independent samples. The most prominent difference between the two orientations is in the region $k = 5 - 8$ Å^{-1}.

dichroism was also not reproducible across all samples, so we concentrate here on peak II. The order of measurement (10° then 80°, or 80° then 10°) did not affect its dichroism: its amplitude was always largest at 10°, even following measurement at 80°.

To study the angle dependence of peak II, we performed Fourier isolation of the crucial region ('R' = 2.55 – 3.45 Å) from the spectra taken at various angles. Two sets of Fourier isolates are shown in Figure 3.6, where the differences in amplitude are clear: at 80°, the EXAFS contribution is much smaller compared to that at 10°. The 10° spectra have a consistently similar amplitude envelope, whereas the 80° data show major differences between the two samples. The variation originates from a large component of random noise that is present in the 80° isolates. The dichroism observed here (Figs. 3.5 and 3.6) is more pronounced than in many of the previous polarized EXAFS studies[21,22,101,122], and already indicates that the vector of interest is nearer to 10° than 80°.

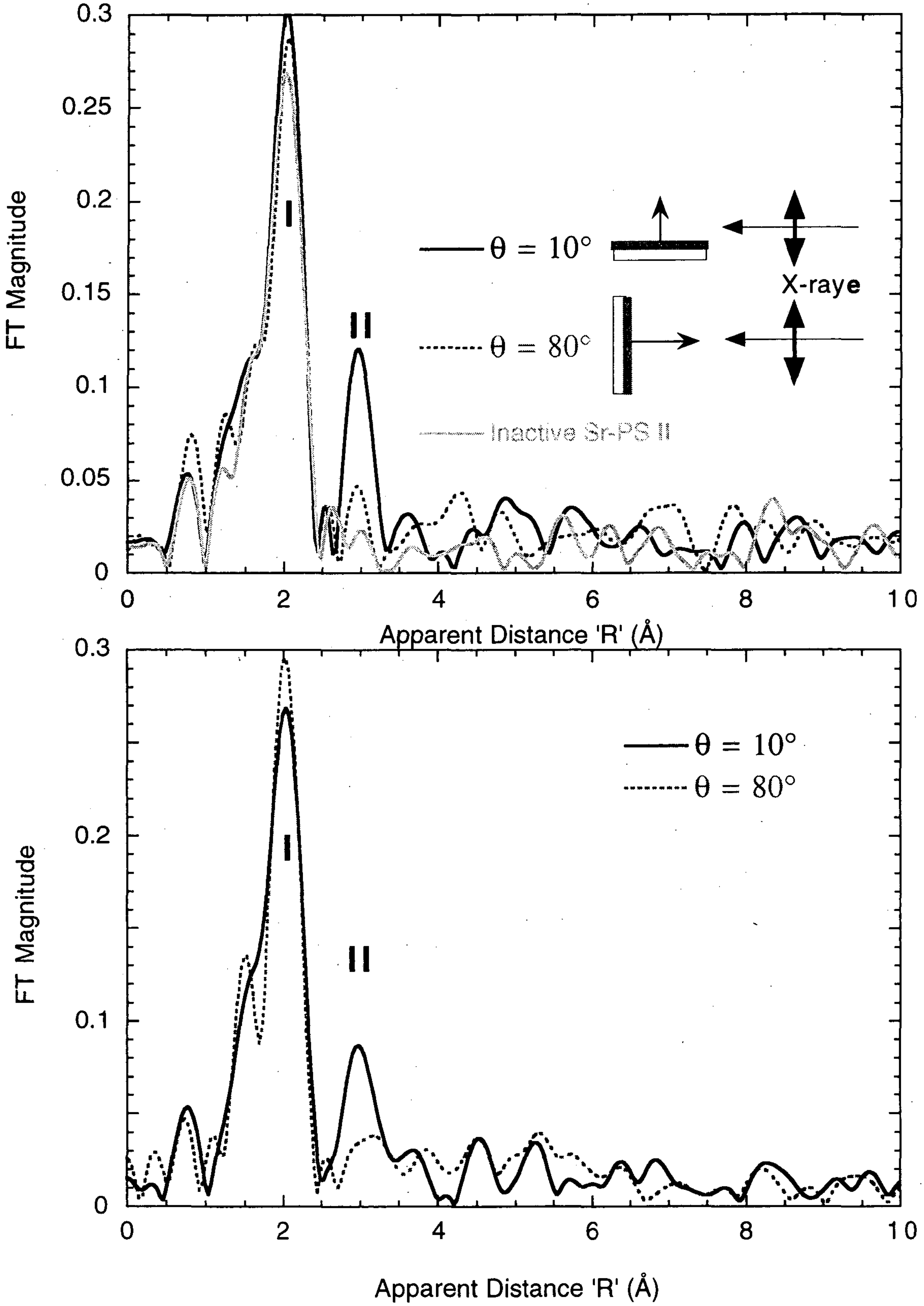
0.3
0.25
0.2
0.15
0.1
0.05
0
FT Magnitude
I
II
θ = 10°
θ = 80°
X-raye
Inactive Sr-PS II
0
2
4
6
8
10
Apparent Distance 'R' (Å)
0.3
0.2
0.1
0
FT Magnitude
I
II
θ = 10°
θ = 80°
0
2
4
6
8
10
Apparent Distance 'R' (Å)

Figure 3.5 Fourier transforms of k^3-weighted EXAFS from oriented Sr-PS II samples at two angles (θ). These are the corresponding transforms of the Figure 3.4. Also included for comparison is the FT of hydroxylamine-treated, inactive PS II. The dichroism is most readily apparent in Fourier peak II ('R' = 3.0 Å). The legend shows the layered PS II membranes and the underlying substrate in relation to the x-ray **e** vector.

EXAFS Curve Fitting

The Fourier isolates at 10°, 30° and 45° were simulated with one shell of Mn as done previously. Carbon and other light atoms were previously ruled out as possible scatterers.[119] Further shells were unnecessary and produced underdetermined fits. The Debye-Waller factor was fixed to the best value ($\sigma^2 = 0.010$) for most of the samples, because the static disorder of a Sr–Mn interaction is not expected to show orientation dependence.[21,101]

Table 3.1 lists the fit results including R, N_{app}, ΔE_0 and the fit error (Φ and ε^2). Two representative results of fitting to 10° spectra are shown in Figure 3.7. These are consistent with earlier Sr–Mn fitting results to peak II,[119] where the lower k region (k = 2.7 - 4.5 Å^{-1}) always has a poorer fit, compared to the rest of the k range. A problem arose when we attempted to simulate data from the higher angles (70°, 80°). As shown in Fig. 3.5, the Fourier peak II is much reduced and within or close to the noise level of the data (see region at 'R' > 4 Å). Because of the inconsistent amplitude envelopes and large proportion of random noise, the fit errors (Φ and ε^2) were always 2-3 times larger than the fits from 10°. Since the resulting fit parameters at 70° and 80° are suspect, the noise problems prevent a precise finding for N_{app}.

However, instead of setting $N_{app} = 0$ as has been done in other studies,[24,101] we decided to estimate the upper limit of N_{app} that could be present in the much reduced peak II based on peak heights in the FTs. The baseline was first measured as the average value of the FT magnitude for 'R' between 4 – 10 Å (Fig. 3.5), where no real features in R-space are detectable, to yield the noise level. Starting from their respective baselines, the net magnitude of peak II at 'R' = 3.0 Å was found, and compared for 10° and 80°. The dichroic ratio (80°/10°) of peak II was then multiplied by the derived N_{app} at 10° (Table 3.1) to give an estimate of N_{app} present at 80°. The fractional

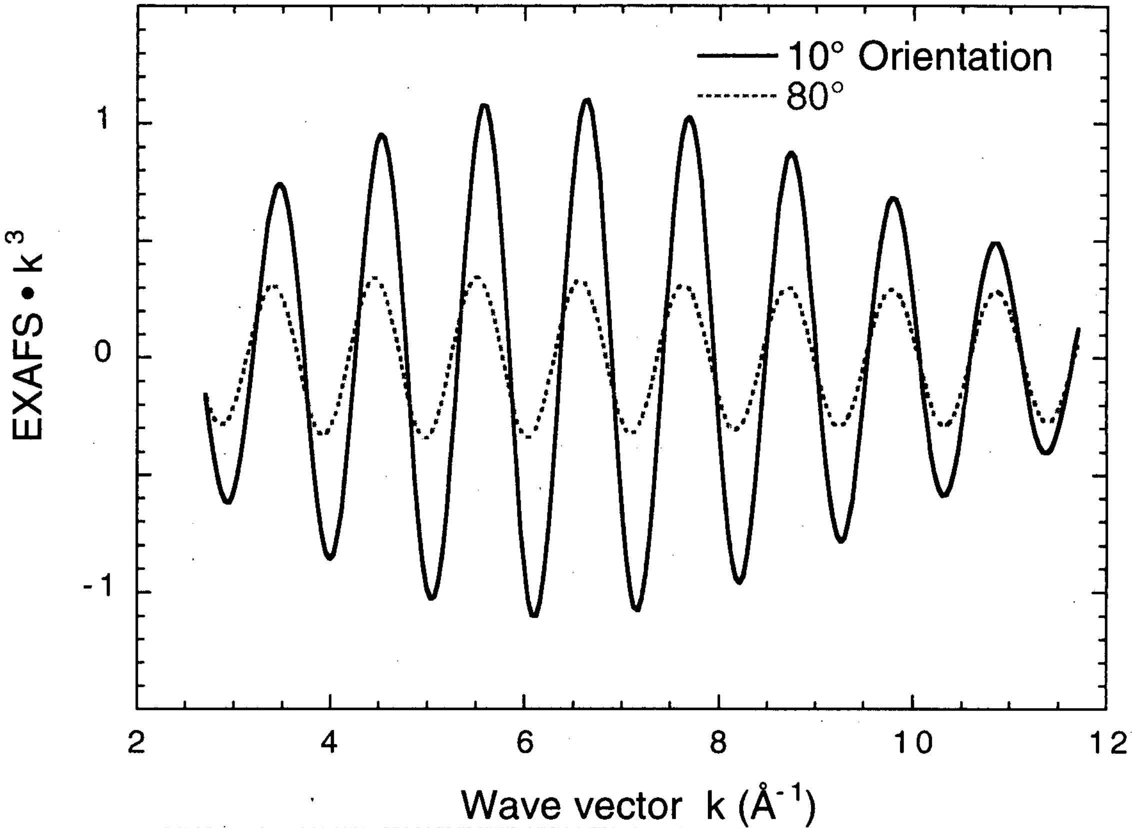

10° Orientation
80°
EXAFS • k^3
1
0
-1
2
4
6
8
10
12
Wave vector k ($Å^{-1}$)

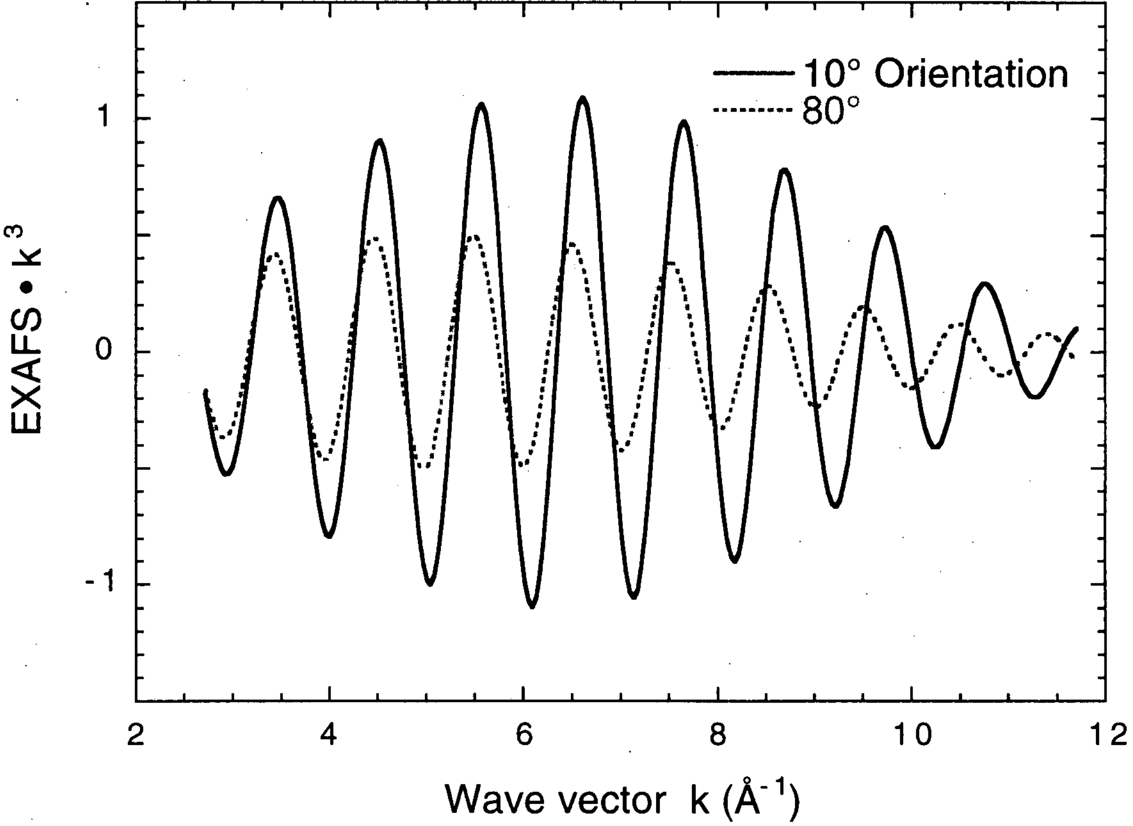

10° Orientation
80°
EXAFS • k^3
1
0
-1
2
4
6
8
10
12
Wave vector k ($Å^{-1}$)

Figure 3.6 Fourier-isolated EXAFS of peak II from two oriented Sr-PS II samples at two extreme angles. These were isolated from the Fourier transforms in Fig. 3.5. The difference in the amplitude envelope of the two $\theta = 80°$ spectra suggests a large component of random noise present in these samples.

Table 3.1 Oriented Sr EXAFS Fitting Results for Peak II

Angle (θ)	R (Å)	N_{app}	ΔE_0 (eV)	$\Phi \bullet 10^3$	$\varepsilon^2 \bullet 10^5$
10°	3.51	2.9	0.07	0.754	0.814
10°	3.52	3.0	-2.4	0.742	0.801
10°	3.52	2.9	-0.25	0.706	0.739
10°	3.53	2.8	1.3	0.685	0.717
10°	3.54	2.8	2.9	0.547	0.572
30°	3.56	2.2	2.5	0.721	0.840
30°	3.48	2.0	-0.05	0.851	0.891
45°	3.53	1.4	2.0	1.35	1.51
45°	3.51	1.6	2.7	0.668	0.710
70°		0.8			
80°		0.7			
80°		0.2			
80°		0.7			
80°		0.3			
80°		0.5			

The Fourier isolates taken from each excitation angle were subjected to curve fitting to the EXAFS equation to give the resulting parameters. The value for σ^2 was fixed to the best value for all samples: 0.010. The fit error parameters (last two columns) have been discussed before.[119] Because the isolates for 70° and 80° were so close to the noise level, curve fitting to them produced unreliable, suspect values. The N_{app} for 70° and 80° were instead calculated from the relative peak II heights in the Fourier transform, and the derived N_{app} at 10° (see text for description).

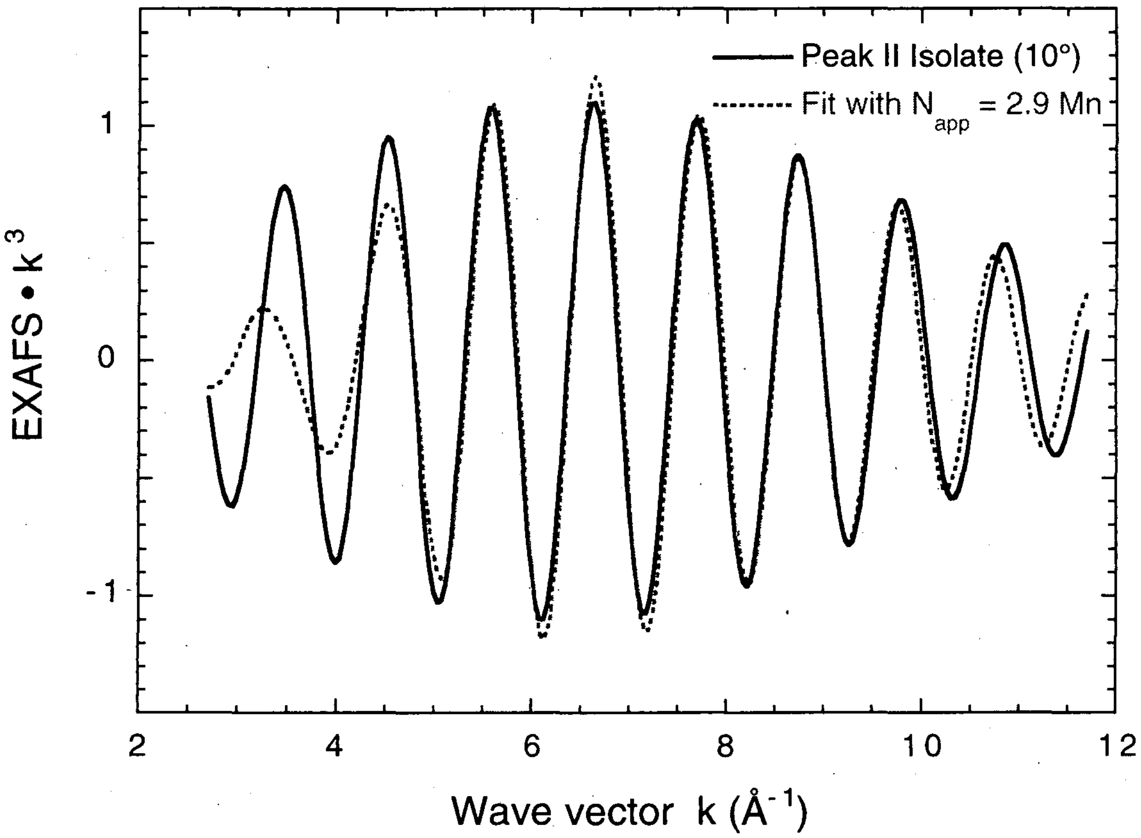
Peak II Isolate (10°)
Fit with N$_{app}$ = 2.9 Mn
EXAFS • k^3
1
0
-1
2
4
6
8
10
12
Wave vector k (Å^{-1})

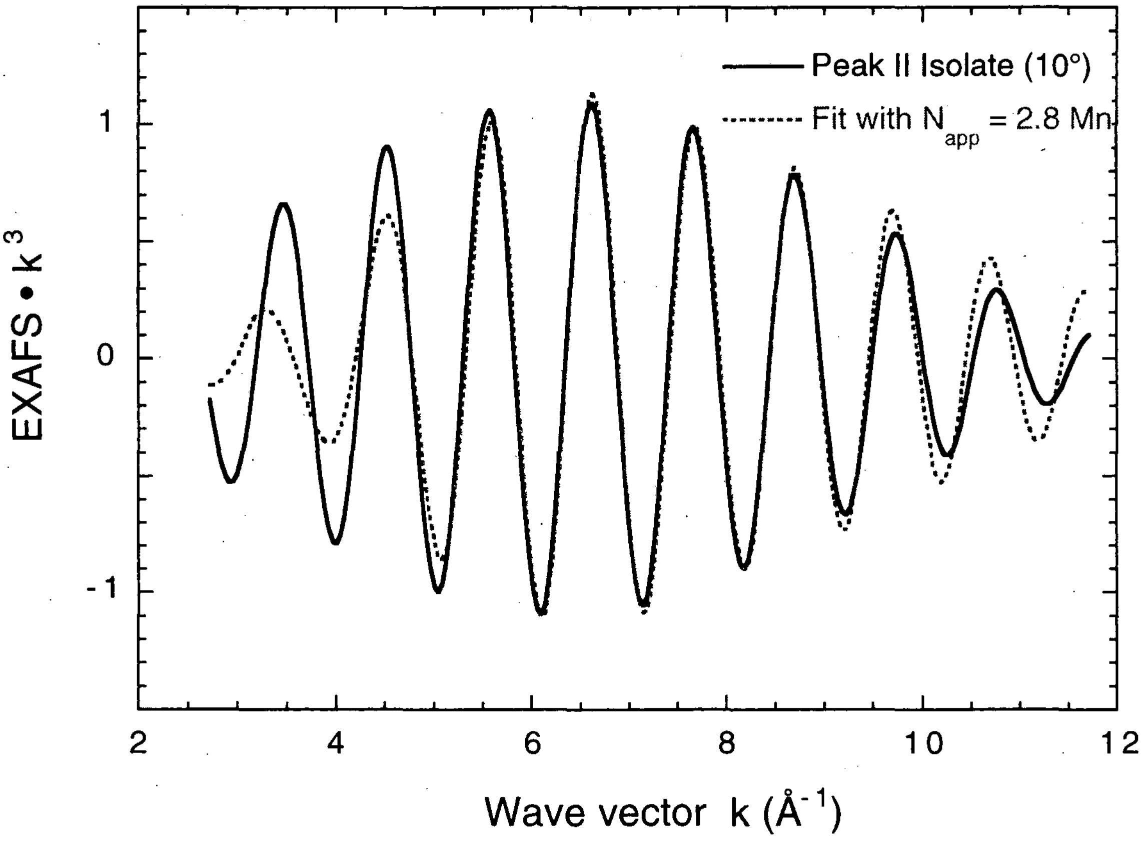
Peak II Isolate (10°)
Fit with N$_{app}$ = 2.8 Mn
EXAFS • k^3
1
0
-1
2
4
6
8
10
12
Wave vector k (Å^{-1})

Figure 3.7 EXAFS curve fitting for the $\theta = 10°$ data from Figure 3.6. The best fit was obtained by varying R, N_{app} and ΔE_0 while fixing σ^2 to the best value (0.010). As found previously, the fit is always deficient in the lower k range (2.7 – 4.5 Å^{-1}) but improves after $k = 5$ Å^{-1}.

amount of peak II present at 80° (compared to 10°) was then listed in Table 3.1 for $\theta = 70°$ and 80°. The N_{app} values in Table 3.1 are subject to ± 25% systematic error as an inherent limitation of the EXAFS technique.[7,8,62,131]

Determination of ϕ

The values of N_{app} in Table 3.1 come from six separate samples, each with its own mosaic spread (Ω). Before these values can be combined in a plot of N_{app} vs. θ, they must be corrected to a common Ω. As stated earlier, the average mosaic spread for the six samples was 15 ± 5°. The correction was made using the plot in Figure 3.8. Equation 3.1 was simulated for each of three Ω values (10°, 15°, 20°), assuming that $N_{iso} = 1$ and $\phi = 20°$. These are reasonable starting assumptions, based on the observed dichroism in Fig. 3.5 (orientation closer to 10° than to 80°). For each measurement angle, the relative correction to N_{app}, when Ω is adjusted to 15°, can be found. For example, at 10° and the sample $\Omega = 10°$, a -5% correction is needed to bring N_{app} in line with $\Omega = 15°$. Likewise, minor adjustments were necessary for the various N_{app}, to allow the use of the common Ω for all 15 points. The original N_{app} values, along with their respective mosaic spread and the corrected N_{app} are listed in Table 3.2.

With N_{app} now found for each excitation angle, θ, we plotted these corrected values in a polar plot and used Eq. 3.1 to find the relative orientation (ϕ) of the Sr–Mn vector and its isotropic coordination number N_{iso}. Nonlinear least-squares regression analysis produced the solid curve shown in Figure 3.9 as the best fit of the 15 data points (angles from six separate samples) to Eq. 3.1. Based on the mathematical simulation, the best fit parameters were: $\phi = 23°$ and $N_{iso} = 1.2$.

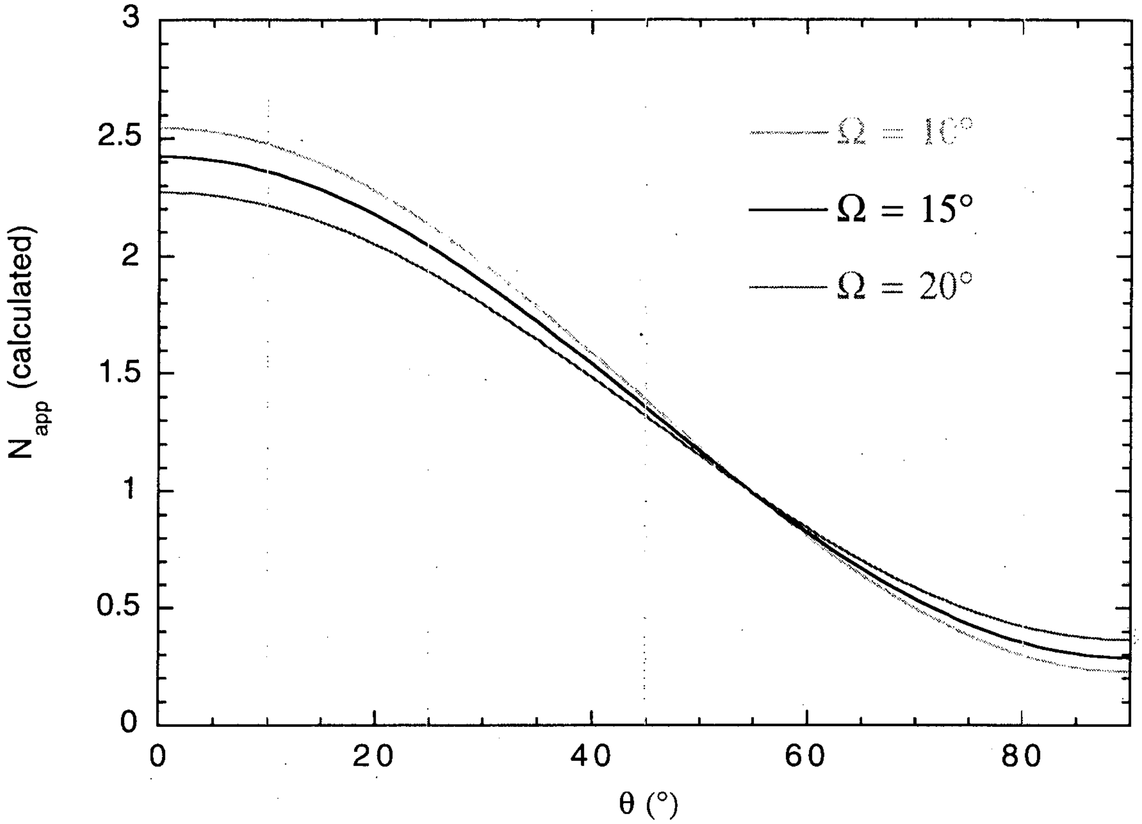

Figure 3.8 Simulation of N_{app} for Different Ω. Assuming N_{iso}= 1 and ϕ = 20°, Equation 1 was calculated for Ω = 10, 15 and 20° to show how N_{app} changes with mosaic spread. Because the three curves encompass the range of mosaic spread values observed for the layered PS II samples, we could adjust the observed N_{app} to values expected at Ω = 15°, the common value used for curve-fitting the orientation dependence of Sr EXAFS (Equation 1). For example, N_{app} from a sample with Ω = 10°, measured at θ = 80°, will have to be adjusted downward by 20%. At θ = 10°, the correction amounts to about 6% per 5° of mosaic spread. Guidelines show the experimental angles listed in Table 3.1.

The six distinct samples (sets of 2 – 4 incident angles each) were also analyzed and fitted separately (data not shown here). This is advantageous because, within each sample, the data from the excitation angles share the same mosaic spread and same Sr content. The results for each sample are then self-consistent. The average of the six sets of extracted parameters (ϕ and N_{iso}) from the individual samples (data not shown) closely matched the results from the collective (15-point) fit mentioned above.

Table 3.2 Corrected N_{app} values for $\Omega = 15°$.

Incident Angle θ (°)	N_{app}	Mosaic Spread Ω (°)	Corrected N_{app}
10	2.9	18	3.0
10	2.9	10	2.8
10	2.8	12	2.7
10	2.8	11	2.7
30	2.2	22	2.4
30	2.0	12	2.0
30	1.9	12	1.9
45	1.4	12	1.4
45	1.6	11	1.6
70	0.8	22	0.9
80	0.7	18	0.8
80	0.2	10	0.2
80	0.7	12	0.6
80	0.3	12	0.3
80	0.5	11	0.4

The N_{app} values from Table 3.1, each with its individual mosaic spread, were corrected to the values expected at $\Omega = 15°$, as described in the text (and using Figure 3.8). The corrected numbers are plotted in Figures 3.9 and 3.10.

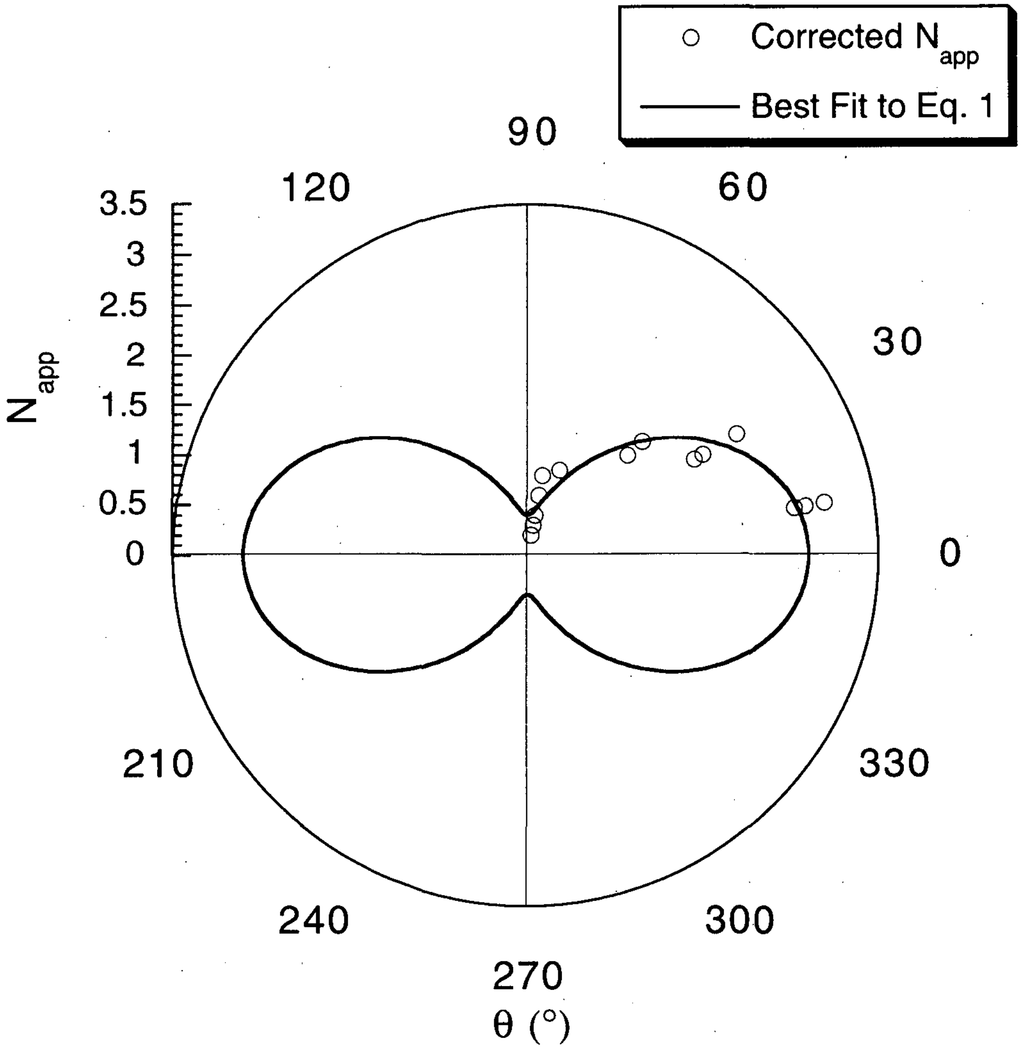

Figure 3.9 Polar plot of the x-ray absorption linear dichroism from oriented Sr-PS II samples. From Table 3.2, the various corrected N_{app} derived from EXAFS curve fitting are plotted (solid circles) with their respective detection angles (θ). A best fit of N_{app} vs. θ is shown as the solid curve (—), according to Equation 3.1 and assuming $\Omega = 15°$. This curve gives $N_{iso} = 1.2$ and $\phi = 23°$. Error bars are discussed in the text.

Discussion

Error Analysis

The major sources of systematic error in the extracted parameters come from the uncertainties in N_{app} and in the mosaic spread. On the other hand, most of the random error is due to the statistical distribution of the data points, or curve fitting error to Equation 3.1. (We assume that θ is accurately determined, with negligible error.) First, the N derived from EXAFS curve fitting can incur an error of ± 25% as described earlier[7,8,62] due to an inherent limitation of the EXAFS technique. This error range was also validated in a recent EXAFS study of Mn distorted cubane complexes (Chapter 3), where the N_{Mn-Mn} derived from curve fitting was compared to known crystallographic values.[131] Therefore, we should allow for ± 25% error in the N_{app} listed in Table 3.1 and 3.2, including those for 70° and 80°, because these were calculated based on the 10° values. The systematic error in N_{app} translates to an error of ± 25% in the fit-derived N_{iso} or 0.3.

Second, there was uncertainty in the mosaic spread used for the fitting to Eq. 3.1. As stated previously, each of the six samples had an individual mosaic spread value. Yet in the collective fit, we used the average Ω (15 ± 5°). In doing so, we accounted for the variability in Ω by correcting each N_{app} to the value expected at $\Omega = 15°$. The adjustments allowed us to address this type of systematic error.

Third, the source of random error lies with the statistical distribution of the data points in the plot in Figure 3.9. The scatter in the points is best shown in the linear plot of Equation 3.1, shown in Figure 3.10. As in Fig. 3.9, the best fit curve yields the N_{iso} and ϕ. However, the least-squares fit of Equation 1 to the points in Fig. 3.9 or 3.10 is imperfect, therefore the derived

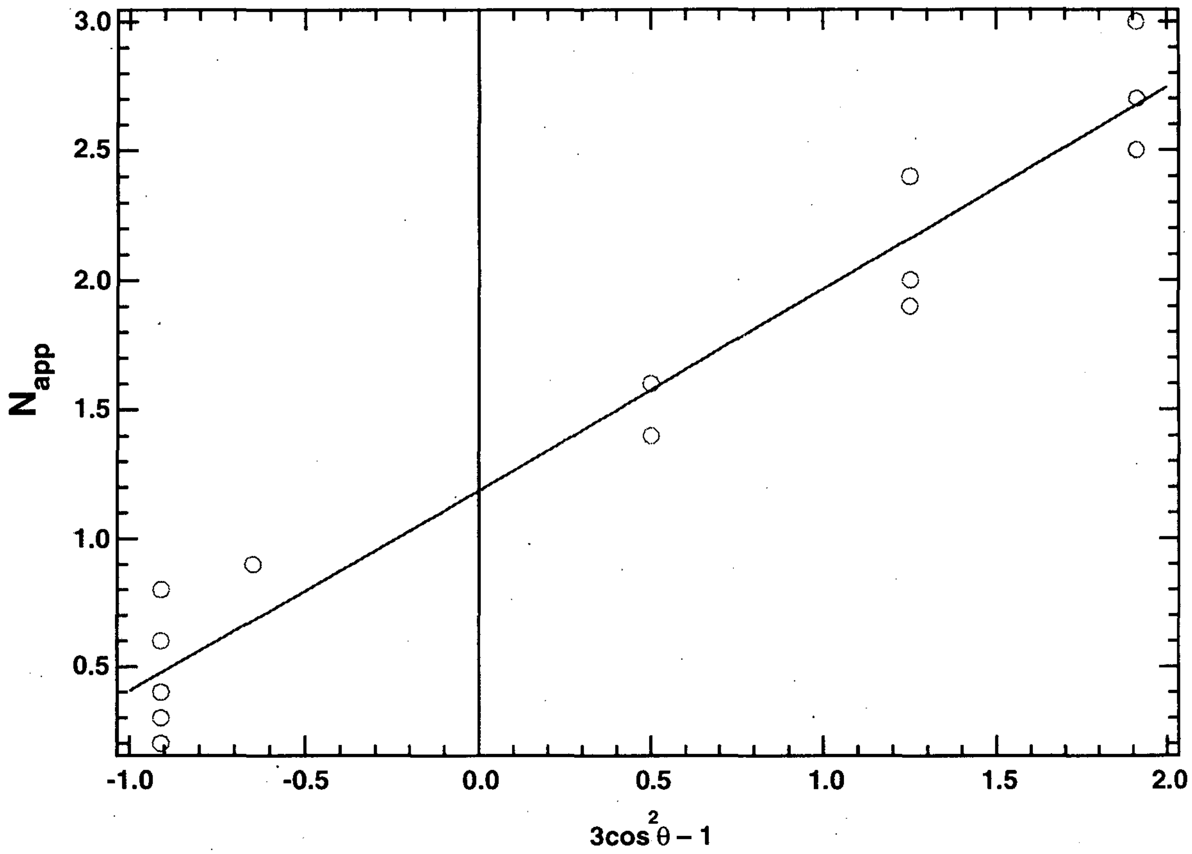

Figure 3.10 Linear Plot of polarized Sr EXAFS Data. This form of Equation 3.1 best shows the scatter of the data points in Table 3.2, and assumes $x = 3\cos^2\theta - 1$ and $y = N_{app}$. It is otherwise equivalent to Figure 3.9. From the best-fit slope, ϕ can be calculated (23°) and the y-intercept yields N_{iso} (1.2). The standard deviations of the slope and y-intercept are derived from the residuals, and translate to random errors in ϕ and N_{iso}.

values of N_{iso} and ϕ incur a standard deviation based on the residuals and the goodness of fit.[129,132] This implicitly assumes that the errors are normally distributed with zero mean and constant variance.[133] For the best fit line in Fig. 3.10, the errors are be related to the standard deviations in the slope and the y-intercept. From analysis of the residuals in Fig. 3.9 and 3.10, the resulting standard deviations are: ± 4° for ϕ and ± 0.1 for N_{iso} . As mentioned before, though, the larger systematic error in N_{iso} (± 0.3) outweighs the random, fitting error (± 0.1) because the former correctly accounts for the inherent ambiguity in EXAFS curve fitting method. After this error analysis, final values for the crucial parameters are: $\phi = 23 \pm 4°$ and $N_{iso} = 1.2 \pm 0.3$.

Implications of the Polarized Sr EXAFS Results

As expected from the pronounced dichroism in the Sr EXAFS (Figs. 3.5 & 3.6), the relative orientation (ϕ) of the Sr–Mn is closer to 10° than 80° (23 ± 4°) and $N_{iso} = 1.2 \pm 0.3$. According to Fig. 3.1, the orientation (ϕ) is a cone around the membrane normal, with the Sr–Mn vector (**R** here) tilted 23°. The observed dichroism and the curve fitting of Fourier peak II also further support the previous finding that Mn is within 3.5 Å for the Ca (Sr) cofactor.[119] If many (> 2) light atoms such as C or O accounted for Fourier peak II, such a marked dichroism would be impossible: it would be difficult to align 3 – 4 (or more) vectors parallel or perpendicular with the x-ray **e** vector to produce the observed behavior. In addition, the extracted N_{iso} also argues against the possibility of $N_{Mn} = 3.0$ raised in the previous Sr EXAFS investigation.[119]

We have accounted for the major sources of error: systematic uncertainty in the measurement of N_{app} (25%) and mosaic spread, and random error in fitting to Eq. 3.1. The first affected N_{iso} substantially (± 25%)

while the curve fit error influenced the spread in ϕ. When the error ranges are considered and after rounding to integer values, the N_{iso} indicates 1 – 2 Mn neighbors to the Sr (and therefore Ca) cofactor. We have detected at least one Sr–Mn vector, but cannot rule out the possibility of a second Mn neighbor because the upper limit of N_{iso} is 1.5, which rounds to 2, a value consistent with the previous Sr EXAFS study of PS II.[119] Also, the observed values from $\theta = 45°$ (the excitation angles closest to the magic angle, where we expect $N_{app} = N_{iso}$) average to $N_{app} = 1.5$, supporting the notion of 1 – 2 Mn scatterers. If $N_{iso} = 2$, the two vectors are indistinguishable (because the difference in distances is less than the EXAFS resolution) with an average angle of 23° ± 4°, and an average distance of 3.5 Å.

Nevertheless, we have to account for possibility that the derived N_{iso} (1.2 ± 0.3) is different from that found in previous Sr EXAFS studies.[119] One possible explanation for this deviation may lie in the inherent nature of the layered samples as compared to the isotropic (pelleted) samples. The pelleted Sr-PS II, though compact, still retains moisture, whereas the layered samples have undergone 18 h of drying under a dinitrogen stream. That process could induce some changes in the local environment of the Sr cofactor, manifesting itself in the loss of one Sr–Mn vector. The loss could result from the loss of one of the two O-bridges depicted in an earlier working model.[119] Such a loss, of perhaps an H_2O bridge, will introduce more disorder into that Sr–Mn vector, rendering it undetectable by EXAFS. To test this prospect, an experiment is suggested below.

Another possible explanation is that the drying process may cause one-half of the functional Sr population to dissociate from its binding site near the Mn cluster. If only one-half of the Sr population remains intact (50% occupancy), then the coordination number, which is based on the total Sr amount, will decrease by 50% (compared to pelleted, isotropic Sr-PS II). We compared the Mn EXAFS from the freshly oriented samples and the isotropic (intact) Sr-PS II (Appendix 2). There are no major differences to indicate increased damage to the Mn cluster itself or Mn^{2+}-release during the drying process. They were virtually identical to each other and to other Mn EXAFS of Sr-reactivated PS II as prepared previously in this research group.[46]

The number of Sr–Mn vectors could also be reduced by radiation damage, which may disrupt the Mn cluster during the 8 – 12 h of data collection per measurement angle. Such disruption would then reduce the amplitude of Fourier peak II, as seen in the hydroxylamine-treated, inactive Sr-PS II.[119] However, it is unlikely that radiation damage has affected the Sr EXAFS from the oriented samples because, as mentioned earlier, the order of measurement (10° then 80°, versus 80° then 10°) did not affect the dichroism of Fourier peak II: its amplitude was still largest at 10°, even following measurement at 80°.

Although previous polarized EXAFS studies on oriented PS II found no difference between oriented and isotropic PS II samples,[22] such an equivalence may not hold true for Sr-reactivated samples. These samples have undergone various treatments (Ca depletion, Sr replenishing, removal of excess Sr) that may render the OEC more sensitive and delicate. For layered Sr-PS II, one additional treatment is the drying process required to orient the membranes. With the OEC already in a delicate state, the dehydration step may alter it enough to differentiate it from the pelleted, isotropic samples. To test the actual differences between the isotropic (pelleted) and oriented samples, one could dry the isotropic samples (without painting or layering them) under a dinitrogen stream, and compare the Sr EXAFS-derived N_{iso} of such (partly) dehydrated isotropic samples to the layered ones. This experiment will determine whether the painting or drying process does affect the number of observed Mn neighbors to the Sr cofactor, and help resolve the differences in N observed here.

Another avenue for future work is the rigorous determination of mosaic spread (Ω). As stated before, the Ω value used here (15 ± 5°) is an estimate, drawn from relating the EPR signal II ratio (90°/0°) to the EPR cyt b_{559} dichroism (see Chapter 6). However, this calibration could be better strengthened and updated with more experimental points to provide more accurate values and account for higher Signal II ratios (> 5). One new way is to relate the Signal II ratio to the disorder found from simulations of the cyt b_{559} EPR spectrum itself, not its dichroism. Through work on high-field EPR, it is now possible to simulate EPR spectra on oriented samples, using known g- and hyperfine tensors, while incorporating a disorder parameter.[134-137] A single spectrum can be calculated and its disorder parameter found without the need for EPR measurements at multiple angles.[21,22,122,126] The calculations of EPR spectra alone, or used in conjunction with Signal II ratios will facilitate the process of finding accurate values for this crucial parameter Ω.

This polarized EXAFS study on oriented Sr-reactivated PS II has detected at least one Sr–Mn vector, at 3.5 Å distance, whose orientation (ϕ) is 23 ± 4° relative to the membrane normal. Referring to Fig. 3.1, this orientation is not one specific angle but instead is a cone around the membrane normal. However, given the current state of the data and the error in N_{iso} (1.2 ± 0.3), we cannot rule out the possibility of two Sr–Mn vectors. If $N_{iso} = 2$, it is not possible to distinguish the individual values of ϕ; instead only an average value $\langle\phi\rangle$ is found[101] (23 ± 4°). The average distance for the two Sr–Mn vectors is 3.5 Å. Thus our best estimate is 1 – 2 Mn neighbors to the Sr (Ca) cofactor. Because Sr has substituted for Ca, the new information is incorporated into a revised working model for the Mn cluster of the OEC that includes the Ca cofactor at 3.5 Å and tilted at 23 ± 4° to the membrane normal. One configuration that is in accord with these constraints is shown in Figure 3.9. The inherent ambiguity in the number of Sr–Mn vectors (1 – 2) is reflected in this model. In the case of $N = 2$, both vectors are identically oriented 23° from the membrane normal and have the same distance (3.5 Å). Previously, we improved on Mn EXAFS studies[46] by using conventional Sr EXAFS on isotropic samples to confirm the proximity of the Ca (Sr) cofactor to the Mn cluster,[119] but could not provide information beyond distances. Now we have advanced the technique by showing that polarized Sr EXAFS studies on oriented samples have obtained additional angular information about the calcium cofactor to further refine the model for the oxygen-evolving complex of PS II.

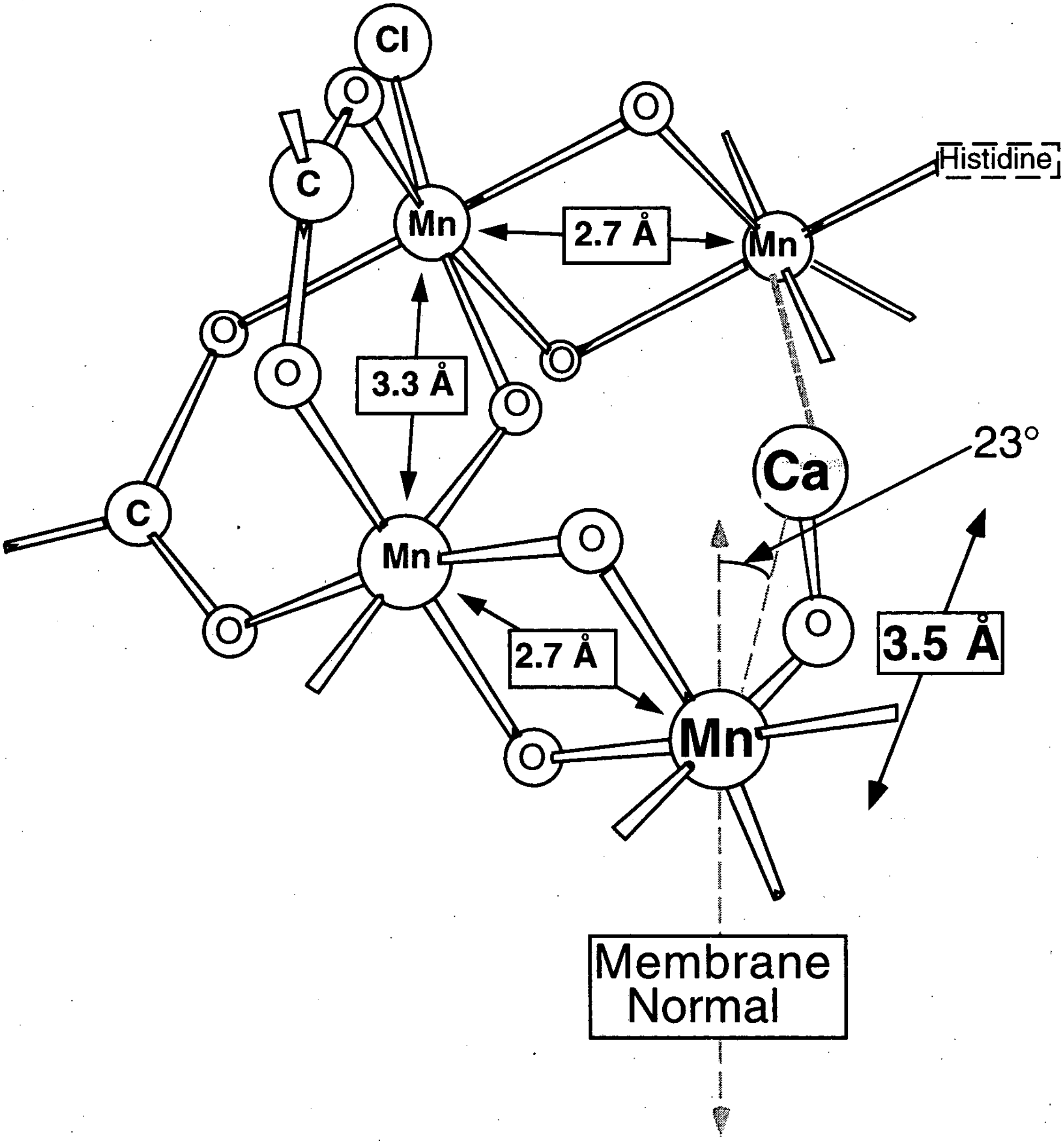
Cl
O
C
Mn
2.7 Å
Mn
Histidine
O
O
O
3.3 Å
O
O
C
Mn
O
O
2.7 Å
Ca
23°
O
3.5 Å
O
Mn
Membrane Normal

Figure 3.11 Revised working model for the Mn cluster of the OEC and its Ca cofactor. The results of the polarized Sr EXAFS study are translated to the Ca cofactor. One configuration (shown) incorporates the new angular information derived from the present polarized Sr EXAFS study: ϕ_{Sr-Mn} = 23 ± 4°. There is the possibility that the number of Mn neighbors to Ca (Sr) can range from 1 – 2. If $N = 2$, the two vectors are indistinguishable with the average orientation of 23° relative to the membrane normal and average distance of 3.5 Å. Because of the one-dimensional order in these membrane samples, the "up" and "down" directions are equivalent. The Mn–Ca (Sr) distance of 3.5 Å was also verified in this study. As drawn, this model does not fully include the angular information in the Mn–Mn vectors, as found from polarized Mn EXAFS studies[21,22] and not all ligands to Mn and Ca are specified. Other configurations consistent with the polarized Sr EXAFS results are possible.

Chapter 4 — Comparison of the Manganese Cluster in Oxygen-Evolving Photosystem II with Distorted Cubane Manganese Compounds through X-ray Absorption Spectroscopy

Introduction

One important goal of bioinorganic chemistry is to produce biomimetic systems that emulate existing active site metal centers structurally and, if possible, functionally. A tetranuclear manganese metalloenzyme under sustained study is the oxygen-evolving complex (OEC) of Photosystem II (PS II).[3,11,138,139] The OEC forms an integral part of the photosynthetic energy transduction chain in green plants, algae and cyanobacteria. The light-driven reaction of photosynthesis converts water and carbon dioxide into carbohydrates and dioxygen. The reducing equivalents for carbon fixation are provided by the OEC, which catalyzes the four-electron oxidation of water. These four electrons are transferred to the reaction center P_{680} (via a redox-active tyrosine Y_Z) as the OEC cycles through five intermediate states S_n ($n = 0 - 4$), gradually storing (up to 4) oxidizing equivalents.[14]

Although it has been the subject of ongoing bioinorganic synthesis, biochemical and biophysical studies, the exact structure of the photosynthetic Mn complex and the mechanism of water oxidation remain unknown. Nevertheless, x-ray absorption spectroscopy (XAS) and electron paramagnetic resonance (EPR) have provided insights into the structure and mechanism of the OEC.[6,7,59] Mn K-edge extended x-ray absorption fine structure (EXAFS) studies have shown the presence of at least two Mn–Mn pairs at ~ 2.7 Å, characteristic of di-μ-oxo bridged Mn, along with mostly oxygen ligation at 1.8 - 1.9 Å.[107] The Mn EXAFS also shows a longer distance interaction at ~ 3.3 Å, whose interpretations in the literature differ. It has been assigned to: 1) one Mn–Mn and Mn–Ca at ~ 3.3 Å;[25,46,107] 2) one Mn–Mn at 3.3 Å;[24,51,94] 3) Mn–Mn or Mn–Ca;[140] or 4) Mn–Ca at 3.7 Å.[49] Further support for including a Mn–Ca at ~ 3.4 Å comes from recent strontium EXAFS studies.[119]

Mn K-edge x-ray absorption near edge structure (XANES) has been used to probe the Mn valence at the different S states.[19,20,115,141] The Mn K-edge positions for the S_0, S_1 and S_2 states have been determined as inflection-point energies from second derivative zero-crossings[142] and the overall edge shape is consistent with oxygen ligation.[107] The shifts in edge position, along with characteristic changes in the edge shapes are indicative of Mn oxidation, so that the proposed Mn oxidation state assignments are as follows: S_0 (II, III, IV, IV) or (III, III, III, IV), S_1 (III, III, IV, IV), and S_2 (III, IV, IV, IV).

Chloride is, along with calcium, an essential cofactor for oxygen evolution.[10,143,144] Although Cl^- can be replaced with Br^- with retention of activity,[145] the role of this halide is still unknown. Until recently, Mn XAS methods have been inconclusive in finding the presence of halide in the ligation sphere of the Mn,[24,49,140,146,147] probably due to the low levels of Cl^- ligation (1 Cl per 4 Mn). A recent report of polarized Mn EXAFS on oriented PS II membranes has suggested that chloride is a ligand to the Mn cluster in the S_3 state.[148] The perturbation of the Mn–Mn 2.7 Å distance by fluoride (F^-, an inhibitor of oxygen activity) is the most direct evidence available of halide binding.[149]

Interest in the OEC and other Mn-containing metalloenzymes has stimulated the synthesis and characterization of polynuclear manganese complexes as possible structural (if not yet functional) models of the catalytic active site.[62,97,150-153] The type of proposed structure of the OEC at the various S states (S_0 - S_4) has profound implications for the proposed mechanism for water oxidation. Mechanisms have been proposed based on the "dimer-of-dimers" motif,[11,97,106] the "cubane" geometry,[154] and the "butterfly" cluster.[155] To sort through the multitude of possible models for the active site, the Mn EXAFS data from several multinuclear Mn model complexes have been analyzed and compared with the data from the OEC.[25,62,146,156,157] Earlier studies have shown that the symmetric "cubane-like" or "butterfly" motifs are incompatible with the observed numbers of 2.7 Å and 3.3 Å Mn–Mn vectors.[25,146] "Vector" here is defined as a pair of absorber and backscatterer atoms that are not necessarily bonded. The symmetric cubane was also ruled inconsistent based on the dichroism observed for the EXAFS data from PS II.[22,102] From the many ways to arrange four Mn atoms to include distances of 2.7 Å and 3.3 Å consistent with the PS II EXAFS, ten possibilities were considered in a previous study.[25] These are shown in Figure 4.1 and are grouped roughly as "dimer-of-dimers" (**1** - **4**), "trimer-monomer" (**5** - **7**) and "tetranuclear" (**8** - **10**) clusters.[25] Because of the presence of the requisite 1.8 Å Mn–O, 2.7 Å Mn–Mn and ~3.3 Å Mn–Mn distances, any of these ten topologies could be a viable model on the basis of XAS data. However, four of the ten complexes (**1**, **5**, **6**, **7**) are particularly consistent with the coordination numbers predicted from PS II EXAFS, so that we currently favor the "dimer-of-dimers" cluster (especially **1** in Fig. 4.1).[11,16]

One of the ten possibilities, the $[Mn_4O_3]$ trigonal pyramid unit (**8**), is the subject of this current study, where we investigate a series of $[Mn_4(\mu_3\text{-}O)_3(\mu_3\text{-}X)]^{6+}$ units with Mn K-edge EXAFS and XANES, and compare them to recent data from the OEC. These compounds are of great interest because they satisfy the requisites for modeling the OEC active site: ~ 2.7 Å and ~ 3.3 Å Mn–Mn vectors, and (for many of the cubanes) mostly O ligands. These synthetic complexes are best described as "tetra-face-capped Mn_4 trigonal prisms" or for convenience, highly distorted cubanes.[158] The central core consists of a Mn_4 pyramid with the Mn^{IV} at the apex, three Mn^{III} on the basal plane, a μ_3-X bridging the basal plane, and a μ_3-O bridging each of the remaining faces (Figure 4.2). Bridging carboxylate and terminal ligands complete the ligation

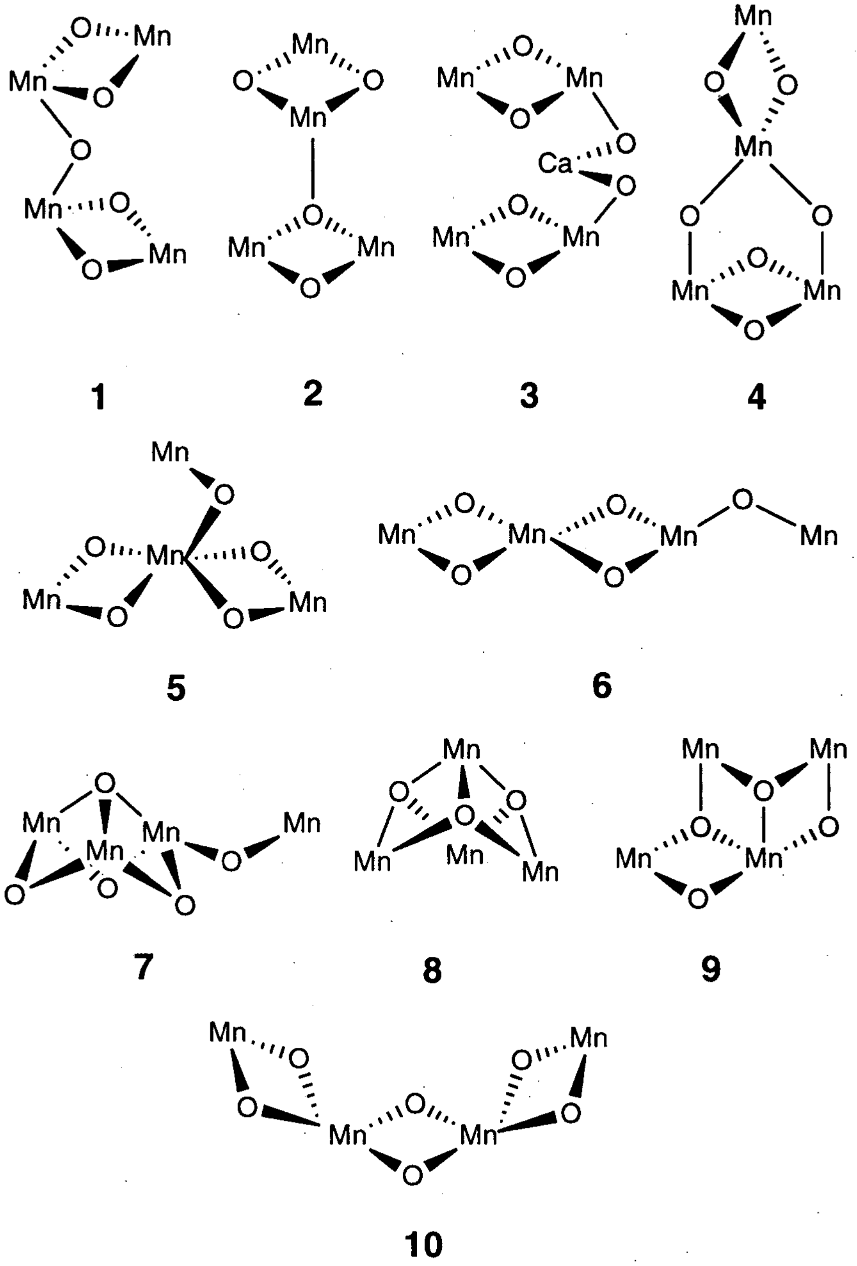

Figure 4.1 Possible core structures for the active site of the OEC in PS II, containing Mn–Mn distances of 2.7-2.8 Å and 3.1-3.3 Å. Reproduced from a previous report.[25] Copyright 1994 American Chemical Society. Only Mn and bridging O are shown.

of each Mn. In the following discussion the "core structure" is defined as the Mn cubane framework, along with the nearest-neighbor ligands to Mn. The core contains Mn^{III}–Mn^{IV} and Mn^{III}–Mn^{III} distances of ~ 2.8 Å and ~ 3.3 Å, respectively, which emphasize the severe deviation from true cubane (T_d) symmetry. The series of $[Mn_4O_3X(OAc)_3(dbm)_3]$ (dbmH = dibenzoylmethane) complexes have different X "substituents": X = **OAc**,[159] **OMe**,[160] **OH**,[160] $\mathbf{N_3}$,[161] **F**,[162] **Cl**,[158,163] and **Br**.[158] Closely related to this series is the compound $[Mn_4O_3(OBz)(OBz)_3(dbm)_3]$, with X = **OBz** (benzoate, O_2CPh), and OBz bridges instead of OAc.[164] Included for comparison are the complexes $Mn_4O_3\mathbf{Cl_4}(OAc)_3(py)_3$ [161,165] and $(pyH)_3[Mn_4O_3\mathbf{Cl_7}(OAc)_3]$[158] possessing single or double, respectively, Cl terminal ligation at each of the three Mn^{III} (Fig. 4.2). Except for the **OBz** cubane core, which has virtual C_s symmetry, the distorted cubanes have virtual C_{3v} symmetry.

The goal of this study is to narrow the topological possibilities for the structure of the OEC by comparing the EXAFS and XANES data from this series of distorted cubane complexes $[Mn_4O_3X]$ of C_{3v} symmetry to those from PS II. The S_1 state of PS II is chosen for comparison because this dark-stable resting state of the enzyme is the most characterized and accessible.[18,107] Because it probes the local structure of the Mn_4O_3X core, EXAFS will be used to detect ligation changes in the series of complexes as the substituent X is altered. Of particular interest will be the substitution of Cl^- by Br^- or F^- to probe the effect of halide on the EXAFS of these complexes. The results of this comprehensive comparison indicate that, while the distorted cubanes do simulate some important features of the Mn EXAFS and XANES, major differences remain in the phases and amplitudes of the *k*-space EXAFS and the Fourier transforms (FT). Based on these findings, the highly distorted cubane of C_{3v} symmetry can be excluded as a topological analog for the active site of the OEC, and a significantly greater distortion of the cubane core would be necessary in order to approach the observed OEC data. The EXAFS method can indeed detect the small changes in the core structures of these cubanes and can differentiate this type of tetranuclear Mn cluster from that present in PS II.

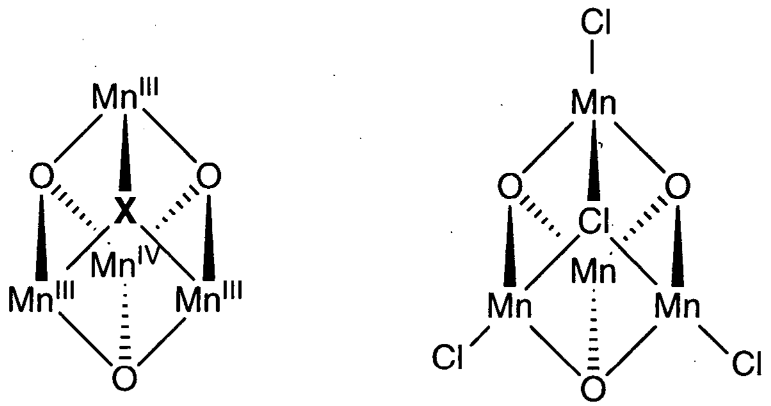

Mn^III
O
O
X
Mn^IV
Mn^III
Mn^III
O
Cl
Mn
O
O
Cl
Mn
Mn
Mn
Cl
Cl
O

$Mn_4O_3X(OAc)_3(dbm)_3$
[X = OAc, OMe, OH, N_3, F, Cl, Br]

$Mn_4O_3Cl_4(OAc)_3(py)_3$
[Cl_4]

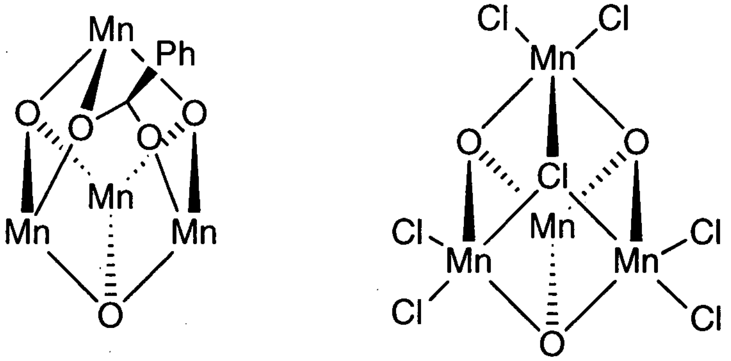

Mn
Ph
O
O
O
O
Mn
Mn
Mn
O
Cl
Cl
Mn
O
O
Cl
Cl
Mn
Cl
Mn
Mn
Cl
Cl
Cl
O

$Mn_4O_3(OBz)(OBz)_3(dbm)_3$
[X = OBz]

$Mn_4O_3Cl_7(OAc)_3[Hpy]_3$
[Cl_7]

Figure 4.2 Core structures of tetranuclear Mn cubane complexes: $[Mn_4O_3X(OAc)_3(dbm)_3]$ (with X = **OAc, OMe, OH, N$_3$**, F, **Cl**, **Br**), $[Mn_4O_3($**OBz**$)(OBz)_3(dbm)_3]$, and the multi-halide $Mn_4O_3Cl_4(OAc)_3(py)_3$ and $(pyH)_3[Mn_4O_3Cl_7(OAc)_3]$. Carboxylate bridges and other terminal ligands outside the cubane framework are not depicted.

Experimental Section

Sample Preparation

The following tetranuclear Mn cubane complexes have been prepared and characterized: $[Mn_4O_3X(OAc)_3(dbm)_3]$ with X = **OAc**,[159] **OMe**,[160] **OH**,[160] **N_3**,[161] **F**,[162] **Cl**,[158,163] **Br**,[158] **OBz** (with OAc replaced by OBz),[164] $Mn_4O_3\mathbf{Cl_4}(OAc)_3(py)_3$[161,165] and $(pyH)_3[Mn_4O_3\mathbf{Cl_7}(OAc)_3]$.[158] For convenience, the Mn model compounds will be designated by their special substituent (X, or **Cl_4** or **Cl_7**). XAS samples were made by carefully grinding 5 - 10 mg of compound and diluting with ten-fold excess of boron nitride. The mixture was packed into 0.5-mm-thick Al sample holders and sealed with Mylar windows.

PS II-enriched membranes were isolated from market spinach using a slightly modified BBY preparation,[66,67] with final activities of ~ 600 (µmol of O_2 / mg of Chl) / h. The membranes were resuspended in buffer A (50 mM MES pH 6, 400 mM sucrose, 5 mM $CaCl_2$) and pelleted by centrifugation at 4°C, 39000 *g* for 1 h. The pellets were then loaded directly into Lucite sample holders designed to fit into both EPR and X-ray cryostats. The final Mn concentration in these samples was 600 - 750 µM Mn, assuming 30 mg of Chl/mL and 200 Chl/PS II. Samples were dark-adapted in the S_1 state, then frozen, stored and transported in liquid nitrogen. Care was taken to prevent warming of biological samples when transferring them to the liquid helium cryostat used for EPR and X-ray spectroscopy. The biological samples were characterized with oxygen evolution activity assays and EPR measurements, as described previously.[25]

X-ray absorption spectroscopy

Mn XAS experimental conditions have been previously detailed[25] and are summarized here. XANES and EXAFS spectra were recorded at the wiggler Beamline VII-3 of the Stanford Synchrotron Radiation Laboratory, with beam current of 65 - 100 mA at 3.0 GeV. The X-ray beam was used unfocused, with an energy-scanning Si[220] double-crystal monochromator detuned to 50% to attenuate higher harmonics. The compound $Mn_4O_3\mathbf{Br}(OAc)_3(dbm)_3$ was measured using a harmonic rejection mirror in the beam path,[166] and ionization chamber detectors (I_0, I_1, and I_2) were filled with dinitrogen. For model compounds, data were collected as fluorescence excitation spectra with a Lytle detector,[167,168] but PS II samples required a 13-element Ge detector.[169] In either case, absorption was related to the fluorescence signal divided by the incident flux ($A = I_F / I_0$). A liquid-helium flow cryostat (CF1208A, Oxford Instruments) kept the samples at 10 ± 1 K in a gaseous helium atmosphere at ambient pressure. Scans were collected from 6520 to 7100 eV, with step sizes of 0.2 eV in the XANES region (6535 to 6575 eV), and 0.05 $Å^{-1}$ in the EXAFS region ($k = 2 - 12$ $Å^{-1}$). Energy calibration and resolution were monitored by simultaneous measurements of the absorption spectrum of $KMnO_4$, using its narrow pre-edge line at 6543.3 eV (FWHM $\leq$ 1.7 eV). Reproducibility of the Mn K-edge position in the above conditions is typically ± 0.1 eV.[19] Four scans were averaged for each Mn compound, whereas PS II required four XANES scans and ~ 20 EXAFS scans.

Data Analysis

Data reduction for Mn XANES and EXAFS has been detailed earlier and is summarized here.[19,25,46] The pre-edge background was removed from all spectra by subtracting a linear fit to the pre-edge region. The data were divided by the Mn free-atom absorption and normalized to unit edge step by extrapolating a quadratic fit from the post-edge region (> 7000 eV) to the energy of the edge peak. For XANES spectra, the first inflection-point energy of the steeply rising absorption edge was determined from the zero-crossing of the second derivative of the spectrum, produced by analytical differentiation of a third-order polynomial fit to the data over an interval of 3.0 eV on each side of a data point. This inflection-point energy (IPE) was taken as the K-edge energy position. For EXAFS spectra, a smooth background absorption curve (quadratic fit to the post-edge region) was removed from the data to leave the net EXAFS. Conversion from energy space into photoelectron wave vector[78] (Å^{-1}) was done as in Eq. 4.1, where m_e is the electron mass, h is Planck's constant, E is the X-ray energy and E_0 is the ionization threshold, chosen as 6563 eV and assigned to the edge peak.

$$k = (2\pi / h)[2m_e(E - E_0)]^{1/2} \tag{4.1}$$

The EXAFS data were weighted by k^3 and low-frequency background was subtracted as a two-domain spline. No windowing function was applied to forward Fourier transforms but a Hanning window was used for Fourier filtering. Limits in k-space and R-space for the forward and back Fourier transforms are shown in Table 4.1S. Fourier peaks were isolated individually and together, to help simplify the analysis and to minimize the effects of distortions from windowing.[170] The resulting Fourier-filtered data were subjected to nonlinear least-squares curve fitting to the EXAFS equation[25,46,78,80,94] (Eq. 4.2) using single-scattering amplitude and phase functions calculated from the program FEFF 5.05.[82,83] The EXAFS amplitude, $\chi(k)$, is described by the following equation:

$$\chi(k) = S_0{}^2 \sum_i N_i B_i(k) \frac{f_{eff}(\pi,k,R_i)}{kR_i^2} \exp(-2\sigma^2 k^2) \exp(\frac{-2R_i}{\lambda(k)}) \times \sin\left[2kR_i + 2\delta_i^c(k) + \phi_i(k)\right] \tag{4.2}$$

where for each shell i, N_i is the number of scatterers at a distance R_i, $S_0{}^2$ is the many-body amplitude reduction factor, $B_i(k)$ is an amplitude reduction factor caused by inelastic forces in the central atom, f_{eff} is the effective backscattering amplitude of the scattering atom, $\delta_i{}^c$ and ϕ_i are the phase shifts for the absorber and backscatterer, respectively, σ^2 is the Debye-Waller term, and $\lambda(k)$ is the mean free-path of the photoelectron. The basic structure used for calculation of FEFF 5.05 fitting functions (f_{eff}, δ, ϕ, λ) was that of the model complex **OMe**,[160] but other Mn–scatterer interactions were constructed, such as for Mn–F / Cl / Br at distances from 2.2 - 2.8 Å. Curve fitting of the filtered data normally extracts the parameters R, N, σ^2, and ΔE_0, where for each shell: N is the number of scatterers at distance R; σ^2 is the Debye-Waller term; and ΔE_0 is the difference between the ionization threshold E_0 of the reference and of the unknown.

Error analysis of the EXAFS fitting results has been discussed elsewhere.[46,86,149,171] The normalized error sum (Φ, Equation 4.3) represents the general quality of the fit where N is the number of data points, $\chi^{\mathrm{expt}}(k_i)$ and $\chi^{\mathrm{calc}}(k_i)$ are the experimental and calculated EXAFS.[86] The normalization factor s_i is defined in Equation 4.4.

$$\Phi = \sum_i^N \left(\frac{1}{s_i}\right)^2 \left[\chi^{\mathrm{expt}}(k_i) - \chi^{\mathrm{calc}}(k_i)\right]^2 \tag{4.3}$$

$$\frac{1}{s_i} = k_i^3 \Big/ \sum_j^N k_j{}^3 \left|\chi_j{}^{\mathrm{expt}}(k_j)\right| \tag{4.4}$$

Another important indicator of fit quality is a χ^2-like statistic, the ε^2 error (Eq. 4.5), which accounts for the number of variable fit parameters (p) and the number of independent data points (N_{ind}). Because the ε^2 error is weighted by the degrees of freedom ($N_{\text{ind}} - p$), the inclusion of additional, unjustified shells of scatterers incurs a penalty, and we can determine whether including more parameters (p) actually improves the fit.

$$\varepsilon^2 = \left[N_{ind}/(N_{ind} - p)\right]N^{-1} \cdot \Phi \tag{4.5}$$

Both values are presented here, but curve fitting was done by minimizing the Φ error specifically, while varying R and σ^2 for each shell of scatterers. The limited information content in the EXAFS spectrum precludes allowing all four parameters (per shell) R, N, σ^2, and ΔE_0 to vary. Especially in the fits to peaks I-II-III, floating all such variables would result in an underdetermined fit ($p > N_{ind}$). Therefore for these whole-spectrum fits, we used only a single ΔE_0 for all shells[46,80] and restricted N to known values from crystallography or previous results.[25] Later, in subsequent two-shell fits to peak II (isolates), N was allowed to float and the observed N was compared to the known values. Coordination numbers are calculated on a per Mn basis and interpreted here in the context of a total of four Mn atoms per PS II. This means that Mn–scatterer interactions appear in multiples of 0.25, except for Mn–Mn interactions, where the increments are 0.5, because each Mn would detect the other at the same distance. Throughout the analysis, data from PS II and the inorganic complexes were processed as uniformly and consistently as possible, especially in the normalization stage, to validate comparisons between the two sets.

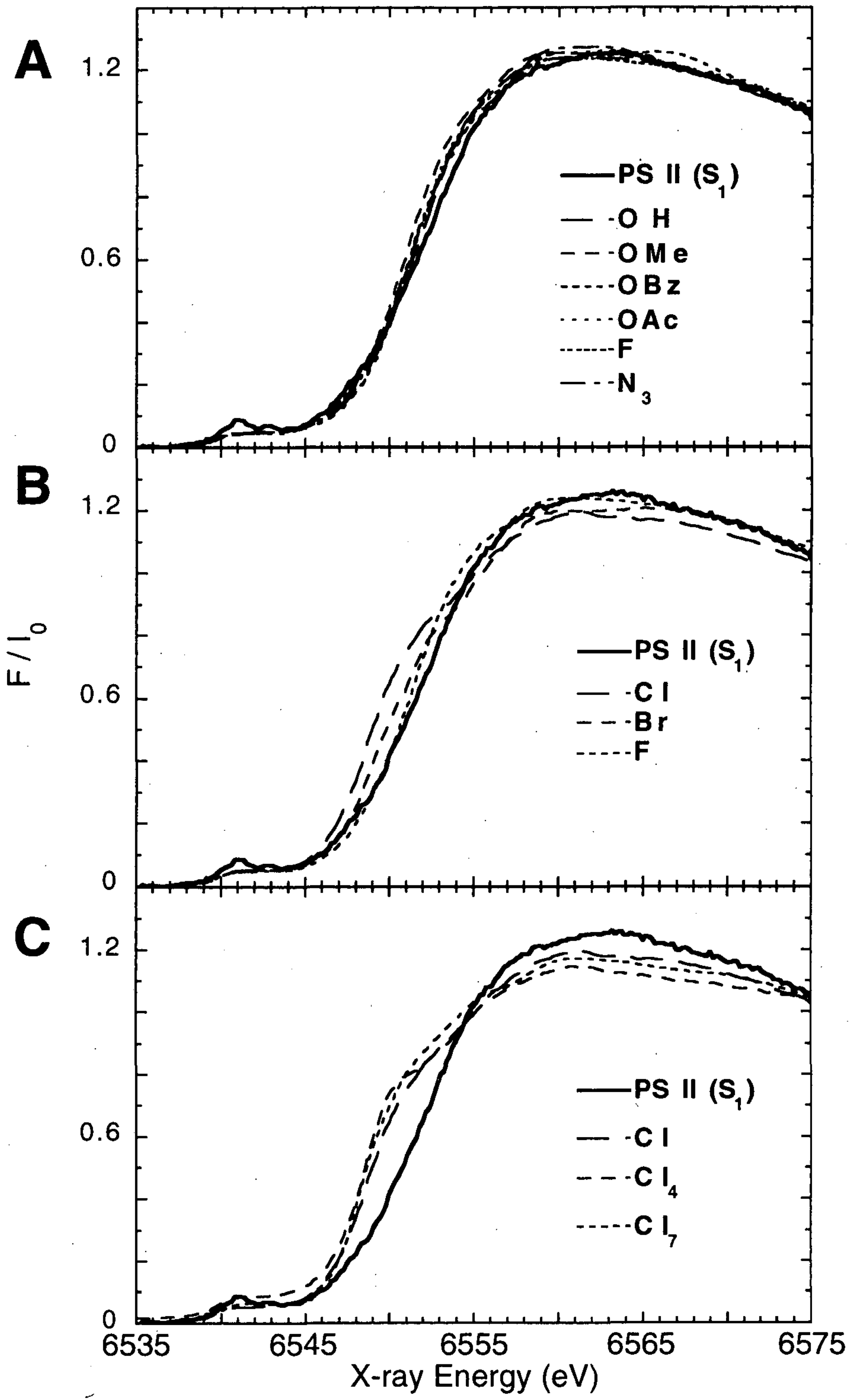
A
B
C
1.2
0.6
0
F / I_0
PS II (S_1)
O H
O Me
O Bz
O Ac
F
N_3
Cl
Br
F
Cl
Cl_4
Cl_7
6535
6545
6555
6565
6575
X-ray Energy (eV)

Figure 4.3 Normalized Mn K-edge X-ray absorption near-edge structure (XANES) spectra of spinach Photosystem II (PS II) preparations poised in the S_1 state and model compounds: (A) **OBz, OAc, OMe, OH, N_3,** and **F**; (B) **F, Cl, Br**; (C) **Cl, Cl_4,** and **Cl_7**.

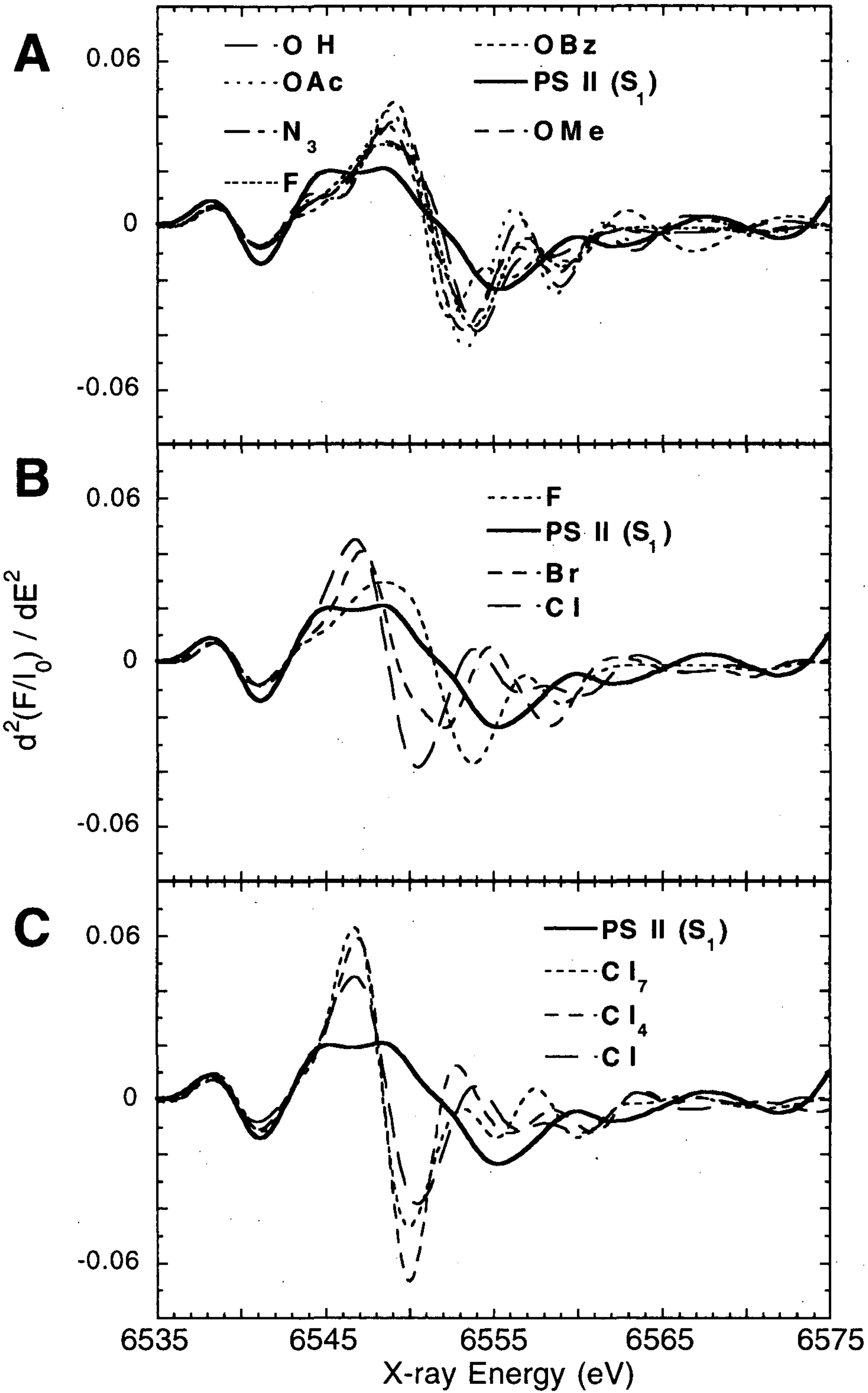
A
O H
OAc
N3
F
OBz
PS II (S1)
OMe
B
F
PS II (S1)
Br
Cl
C
PS II (S1)
Cl7
Cl4
Cl
0.06
0
-0.06
d2(F/I0) / dE2
6535
6545
6555
6565
6575
X-ray Energy (eV)

Figure 4.4 (A) Second derivatives of the edge region of the samples in Fig. 4.3A. (B) Second derivatives of the edge region of the samples in Fig. 4.3B. (C) Second derivative spectra of XANES from Fig. 4.3C. Data were smoothed by a cubic polynomial fit over ± 3.0 eV around each point.

Results

For comparison purposes, the cubanes are subdivided into three groups: the oxygen ("O") cubanes consisting of **OAc, OBz, OMe, OH**, the "halide" cubanes (**Cl** and **Br**), and the "multiple-halide" cubanes (**Cl_4** and **Cl_7**). Although **N_3** is considered a pseudo-halide, both it and **F** are almost indistinguishable from O by having adjacent atomic numbers, and so **N_3** and **F** are grouped with the O cubanes.

Mn XANES

The Mn K-edge X-ray absorption spectra of the OEC poised in the S_1 state and the tetranuclear models **OBz, OAc, OMe, OH, N_3, F, Cl, Br, Cl_4** and **Cl_7** are presented in Figure 4.3A-B-C with their corresponding second derivatives presented in Figure 4.4A-B-C. Fig. 4.3A shows that the O cubanes resemble the general edge shape of PS II, but differ in the pre-edge region (6540 - 6544 eV) and the steeper rise of the K-edge (6549 - 6553 eV). The inflection-point energy indicates the Mn K-edge position and is defined as the zero-crossing of the second derivative (Fig. 4.4A-B-C). Mn K-edge positions of these compounds are given in Table 4.1, where the estimated error is ± 0.2 eV, from previous XANES studies.[19] This set of tetranuclear model compounds contains 3 Mn^{III} and 1 Mn^{IV}, which is one possible assignment for S_0. For **OBz, OAc, OMe, N_3, F** and **OH** we find edge positions between 6550.9 and 6551.8 eV (Table 4.1). These numbers are higher than those reported for the S_0 state of PS II, but the second derivative spectra (see Fig. 4.4A-B-C) show that the overall edge shape is similar to the one we find for the S_0 state in PS II.[19] The spectra of **OBz, OAc, OMe, N_3, F** and **OH** (Fig. 4A) and PS II in the S_0 state[19] lack a feature around 6552 eV, which is present in S_1. A positive feature around 6548 eV is also present, with a large amplitude and a significantly

Table 4.1 Mn K-Edge Rising Edge Inflection Point (Edge Position) and Mn–O Bond Length for Mn Model Compounds and Different S-States of the OEC

Compound	Edge Position (eV)	Average Mn–O Bond Length (Å) (for O cubanes)	Bond Valence Sum (BVS)	Ref.
PS II S_0	6550.1			19
PS II S_1	6551.7			19
PS II S_2	6553.5			19
$Mn_4O_3(\mathbf{OBz})(OBz)_3(dbm)_3$	6550.9	1.93	3.20	164
$Mn_4O_3(\mathbf{OAc})(OAc)_3(dbm)_3$	6551.5	1.92	3.17	159
$Mn_4O_3(\mathbf{OMe})(OAc)_3(dbm)_3$	6551.3	1.92	3.21	160
$Mn_4O_3(\mathbf{OH})(OAc)_3(dbm)_3$	6551.8	1.91	3.22	160
$Mn_4O_3(\mathbf{N_3})(OAc)_3(dbm)_3$	6551.1			161
$Mn_4O_3\mathbf{F}(OAc)_3(dbm)_3$	6551.5			162
$Mn_4O_3\mathbf{Cl}(OAc)_3(dbm)_3$	6548.7			158,163
$Mn_4O_3\mathbf{Cl_4}(OAc)_3(py)_3$	6548.5			162,165
$[Hpy]_3Mn_4O_3\mathbf{Cl_7}(OAc)_3$	6548.4			158
$Mn_4O_3\mathbf{Br}(OAc)_3(dbm)_3$	6549.3			158

Estimated error in the Mn K-edge positions (inflection points) is ± 0.2 eV from previous XANES measurements on PS II.

narrower width than in S_1. The presence of this narrow feature suggests a greater amount of Mn^{III},[19] and its increased intensity is related to the steeper rising edge in these complexes (Figs. 4.3 and 4.4). Fig. 4.3B-C show that the addition of Cl or Br ligands alters the edge shape significantly by shifting to lower energy as seen in the halide cubane compounds **Cl**, **Br**, **Cl_4** and **Cl_7** (see also Table 4.1 and Fig. 4.4B-C). The exchange of an O atom with one or more Cl atoms (or Br) reduces the ligand hardness and consequently leads to a lower edge position. This is in contrast with **F** and the pseudo-halide **N_3**, which display edge positions within the range of **OBz**, **OAc**, **OMe**, and **OH** (Fig. 4.4A)

We also investigated whether differences in the bond valence sum (BVS) can explain the 1 eV spread that we observe for **OBz**, **OAc**, **OMe**, and **OH**. The bond valence sum analysis (BVSA)[172-174] approach was introduced primarily to assign an oxidation state to a particular metal center based on the knowledge of the nature of the immediate neighbors and the interatomic distances involved. For **OBz**, **OAc**, **OMe**, and **OH** we performed a BVSA using the r_0 values reported by Liu and Thorp[175] and the crystallographic Mn–O distances. Within this set of model compounds there is no change in oxidation states and all compounds exhibit the same structural motif. An overall average shortening of Mn–O distances is reflected in a higher BVS that correlates with a higher edge position. The BVS values for **OBz**, **OAc**, **OMe**, and **OH** are summarized in Table 4.1. The four compounds exhibit almost the same number, showing that the BVS concept cannot satisfactorily explain the different edge positions observed here.

Mn EXAFS

Background-subtracted EXAFS oscillations in *k*-space are presented in Figure 4.5A-B-C for the "oxygen" and "halide" model compounds and PS II.

Table 4.1S Minimum, Maximum, and Width of k for Forward Fourier Transforms and Width of R for Back Fourier Transforms for Peak I-III ($\Delta R_{\text{I-III}}$) in the Experimental EXAFS Spectra, and the Number of Independent Parameters (N_{ind}) for the Data Window Equal to $2\Delta k\Delta R/\pi$.

				Peak I-III	Peak II
Compound	k_{min} (Å^{-1})	k_{max} (Å^{-1})	Δk (Å^{-1})	$\Delta R_{\text{I-III}}$ (Å)	ΔR_{II} (Å)
PS II S_1	3.3	11.7	8.4	3.82	1.11
$Mn_4O_3(\mathbf{OBz})(OBz)_3(dbm)_3$	3.3	11.7	8.4	3.27	1.84
$Mn_4O_3(\mathbf{OAc})(OAc)_3(dbm)_3$	3.3	11.7	8.4	3.43	1.73
$Mn_4O_3(\mathbf{OMe})(OAc)_3(dbm)_3$	3.3	11.7	8.4	3.27	1.67
$Mn_4O_3(\mathbf{OH})(OAc)_3(dbm)_3$	3.3	11.7	8.4	3.52	1.85
$Mn_4O_3(\mathbf{N_3})(OAc)_3(dbm)_3$	3.3	11.7	8.4	3.61	2.03
$Mn_4O_3\mathbf{F}(OAc)_3(dbm)_3$	3.3	11.7	8.4	3.34	1.74
$Mn_4O_3Cl(OAc)_3(dbm)_3$	3.3	11.7	8.4	3.53	2.13
$Mn_4O_3\mathbf{Cl_4}(OAc)_3(py)_3$	3.5	11.7	8.2	3.71	1.29
$[Hpy]_3Mn_4O_3\mathbf{Cl_7}(OAc)_3$	3.3	11.7	8.4	3.82	2.38
$Mn_4O_3\mathbf{Br}(OAc)_3(dbm)_3$	3.3	11.7	8.4	3.31	1.86

For clarity, the spectra presented in Fig. 4.5 are Fourier-filtered data covering peaks I-II-(III), using the *k* windows in Table 4.1S. (The raw, unfiltered k^3-weighted EXAFS spectra of the Mn cubanes and PS II are included in Figure 4.5S.) k^3-weighting is applied to offset the decay of EXAFS amplitude at higher *k*-values and to emphasize the contributions of heavier atoms at longer distances. The data sets of the oxygen cubanes **OBz, OAc, OMe, OH, N_3** and **F** are quite similar and almost overlay each other. Although the pattern of oscillations is similar to that of PS II (Fig. 4.5A), the overall amplitude is considerably and consistently larger, and the EXAFS is phase-shifted (at $k = 8 - 11.5$ Å^{-1}). Together these indicate that, although the distances may be similar, the number of such interactions is different from that in PS II. This distinction is most evident in the Fourier transforms that are shown in Figure 4.6A-B-C and discussed below. The halide cubanes are unique for their incorporation of a single halide into a tetranuclear Mn cluster.[158,163] Of these, the single halides **F, Cl** and **Br** are again similar to each other (Fig. 4.5B), but distinct from PS II, in amplitude and phase. When more chloride atoms are ligated to Mn in **Cl_4** and **Cl_7** (Fig. 4.5C), the EXAFS oscillation pattern changes drastically, but it should be noted that these two compounds have aromatic pyridine ligands.

Mn EXAFS spectra were truncated to $k = 11.7$ Å^{-1} starting from $k = 3.3$ Å^{-1} (see Table 4.1S; forward Fourier transform parameter). The Fourier transforms of the raw *k*-space data of **OBz, OAc, OMe, OH, N_3, F** and PS II are presented in Figure 4.6A, while those of **Cl** and **Br** and PS II appear in Fig. 4.6B. The multiple-halide cubanes **Cl_4** and **Cl_7** are shown in Fig. 4.6C. Two and sometimes three peaks appear at *'R'* = 1.4 - 1.5 Å (I), 2.3 - 2.5 Å (II) and 2.9 - 3.0 Å (III), which are clearly above the noise level. All peaks appear at an apparent distance *'R'* that is shorter than the actual distances by 0.4 - 0.5 Å due

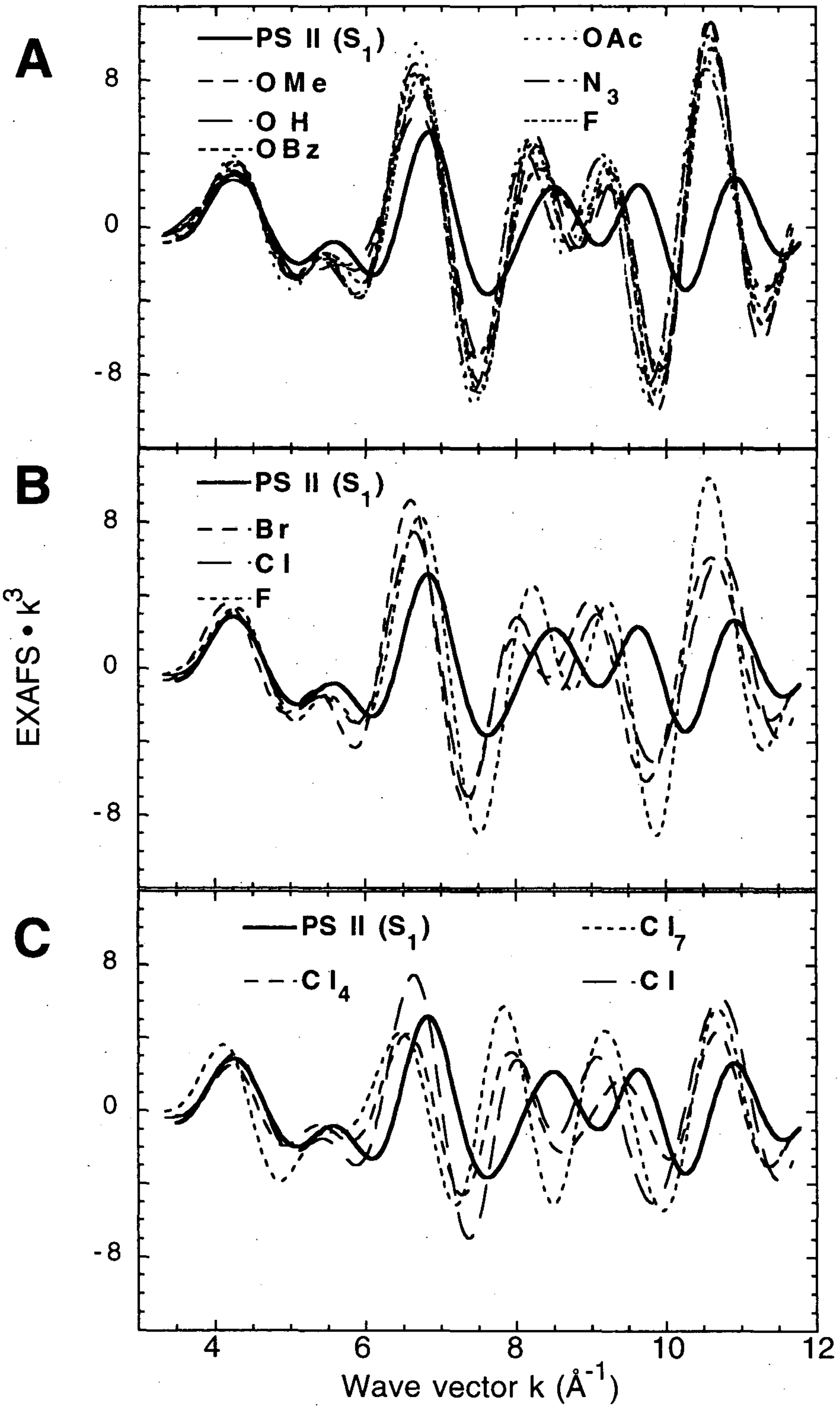
A
PS II (S$_1$)
OAc
OMe
N$_3$
OH
F
OBz
B
PS II (S$_1$)
Br
Cl
F
C
PS II (S$_1$)
Cl$_7$
Cl$_4$
Cl
8
0
-8
4
6
8
10
12
EXAFS • k^3
Wave vector k (Å^{-1})

Figure 4.5 Background-subtracted *k*-space EXAFS from PS II in the S_1 state and model compounds. For clarity, the EXAFS are Fourier-filtered using the ΔR ranges in Table 4.1S, and have been weighted by k^3. The raw *k*-space EXAFS spectra are available in Fig. 4.5S. (A) **OBz**, **OAc**, **OMe**, **OH**, $\mathbf{N_3}$, and **F**; (B) **F**, **Cl**, **Br**; (C) **Cl**, $\mathbf{Cl_4}$, and $\mathbf{Cl_7}$.

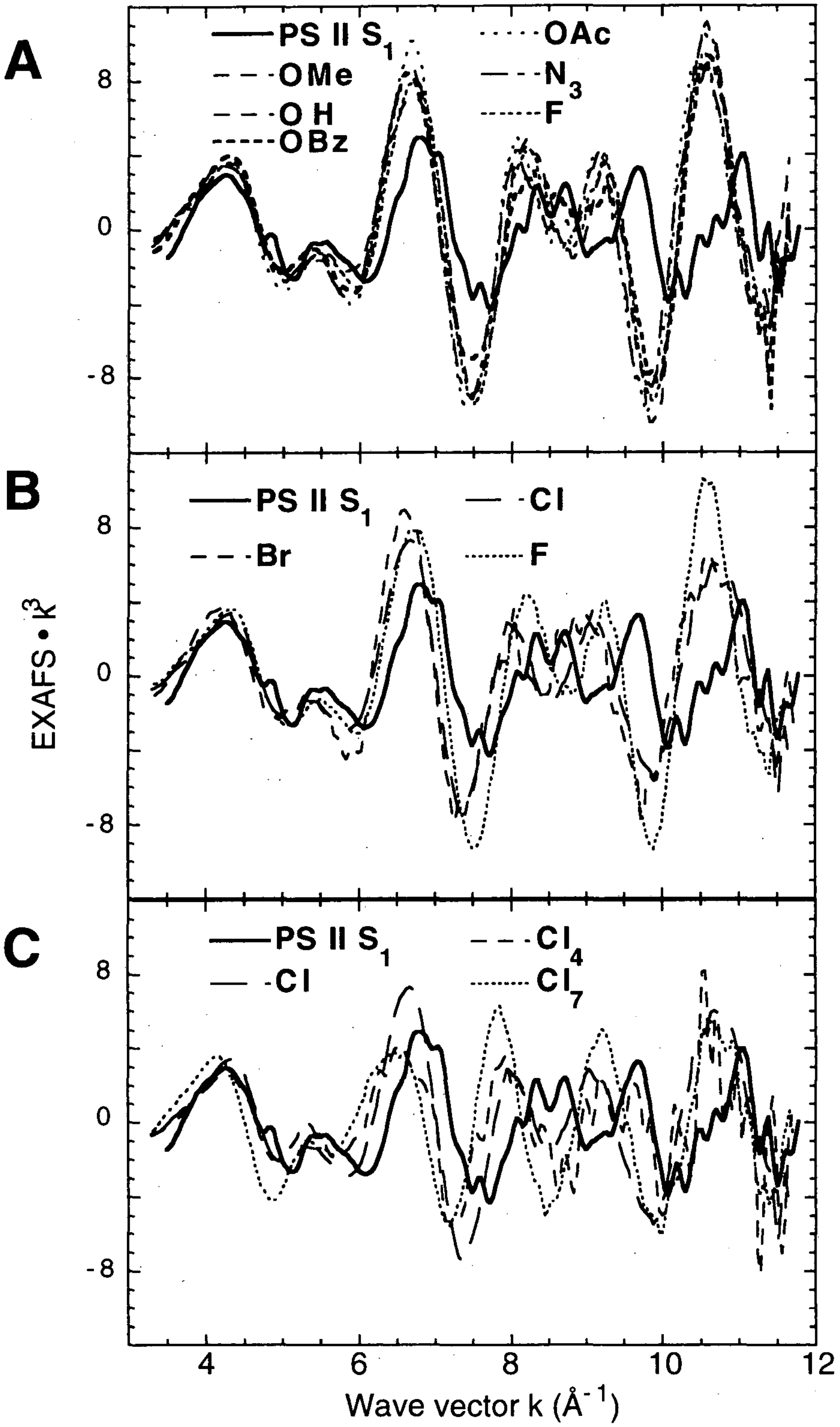
A
PS II S$_1$
OAc
OMe
N$_3$
O H
F
OBz
B
PS II S$_1$
Cl
Br
F
C
PS II S$_1$
Cl$_4$
Cl
Cl$_7$
8
0
-8
EXAFS • k^3
4
6
8
10
12
Wave vector k (Å^{-1})

Figure 4.5S Raw k^3-weighted Mn EXAFS of PS II (S_1 state) and Mn model compounds: (A) **OBz, OAc, OMe, OH, N_3,** and **F**; (B) **F, Cl, Br**; (C) **Cl, Cl_4,** and **Cl_7**. These can be compared with the Fig. 4.5 (after Fourier filtering). The Fourier transforms of these raw k-space data are shown in Fig. 4.6.

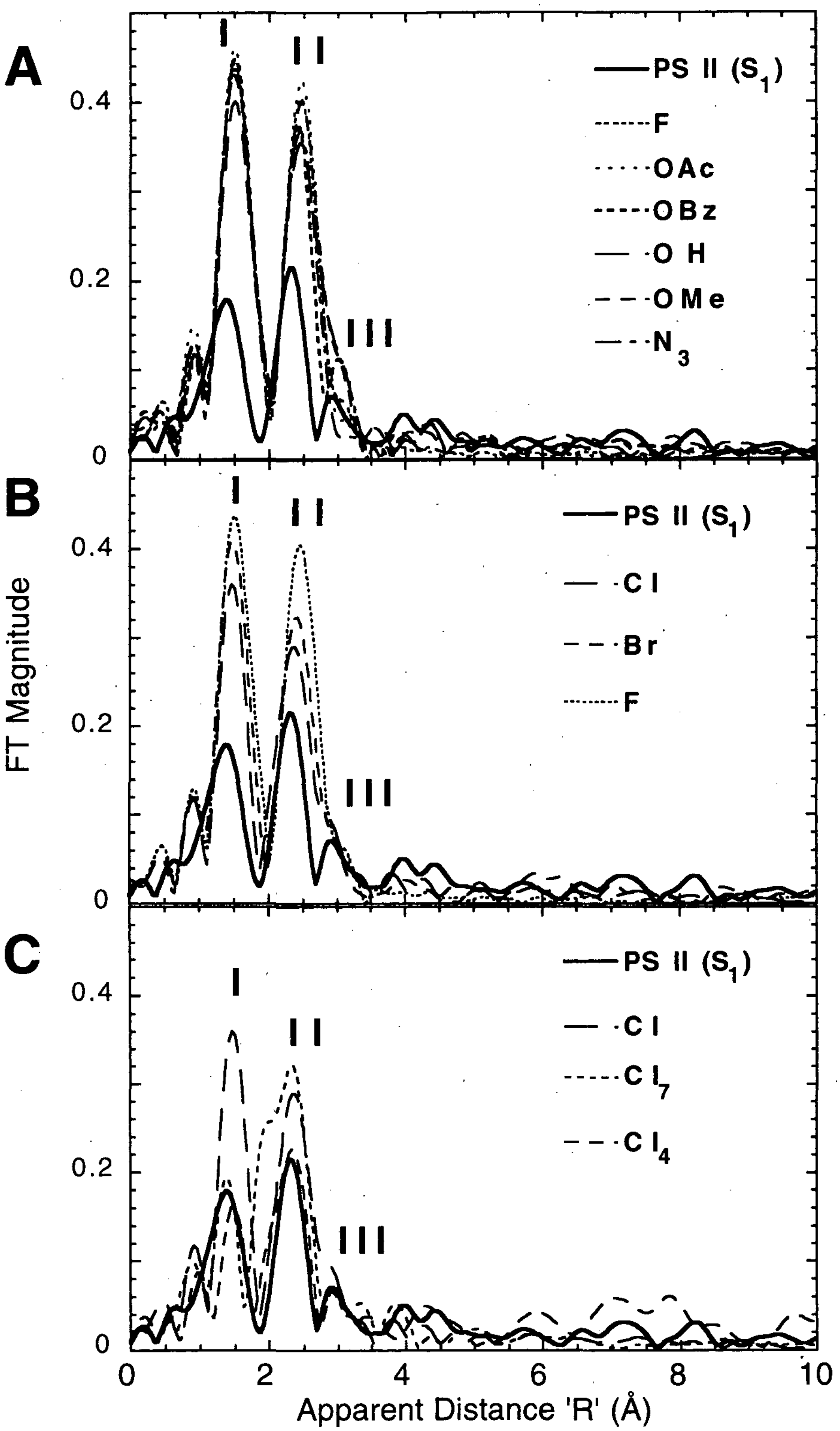
A
B
C
I
II
III
PS II (S1)
F
OAc
OBz
OH
OMe
N3
Cl
Br
Cl7
Cl4
FT Magnitude
0
0.2
0.4
0
2
4
6
8
10
Apparent Distance 'R' (Å)

Figure 4.6 Fourier transform spectra of raw *k*-space Mn EXAFS from PS II in the S_1 state and model compounds: (A) **OBz, OAc, OMe, OH, N_3, F**; (B) **F**, **Cl**, and **Br**; (C) **Cl**, **Cl_4**, and **Cl_7**. The *k*-ranges used were the same as in Fig. 4.5 and the minor peaks at '*R*' < 1 Å are due to residual background.

to a phase shift. The shoulder below 'R'' = 1 Å is a result of incomplete background removal. Compared to PS II, the larger magnitude of the Fourier transforms imply a larger number of ordered contributions to peaks I and II (and III for OBz), and the longer peak distances imply longer average distances for those interactions. The most obvious difference between PS II and the cubane model compounds is in the intensities of peak I and II (Fig. 4.6A-B); those of PS II are much lower. For all other compounds, with exception of **OBz,** the "peak III" appears as a shoulder on peak II. Whereas PS II shows a resolved peak III, only the **OBz** cubane shows a comparable feature, at a slightly longer distance. Another difference is the significant scattering contribution between peak I and II shown by **Cl_4** and **Cl_7** (Fig. 4.6C), as manifested by a shoulder at 'R'' = 1.9 - 2.0 Å or a broadening of peak II. These compounds exhibit 3 and 6 terminal Cl ligands, respectively, at 2.25 Å besides one bridging Cl at 2.65 Å.

Peaks I-II (and III) have been isolated by Fourier filtering (Fig. 4.5A-B-C) for curve-fitting analysis. They have been isolated and analyzed both individually and collectively, but only the results from group fitting will be described here. The curve-fit range was k = 3.3 - 11.7 Å^{-1}. To keep the number of variable parameters from exceeding the number of independent data points and prevent underdetermined fits, the coordination numbers (N, per four Mn) for the cubanes were fixed to crystallographically-known values. For PS II, we used N values determined previously.[25] Also, one ΔE_0 value was used for all shells in each fit, following previous practice.[46,80] For the oxygen cubanes (including **F** and **N_3**), three to four shells are used except for **OBz**, which required five shells. For the halides (**Cl, Br, Cl_4, Cl_7**) four to five shells were used, and we found that a sixth shell did not significantly improve the fit. To evaluate the fits, we monitored the ε^2 error to see whether the addition of more shells (and more variables) actually improved the fit.

We compared the best fit distances to the crystallographically-determined values, which were segregated by shells consisting of a number of neighbors centered at an average distance. The theoretical model used by the FEFF 5.05 program was the **OMe** cubane, from which we generated Mn–scatterer phase and amplitude functions as needed for curve fitting. Only single-scattering functions were used, and we tried to fit only the Mn nearest neighbors and the Mn cubane core. The fit results are tabulated in Table 4.2, where almost all distances were fit to within ± 0.05 Å of the crystallographic values.

For **OBz**, **OAc**, **OMe** and **OH**, two nearest-neighbor oxygen shells were resolved, with 4.5 O at ~ 1.9 Å and another 1.5 O at ~ 2.2 Å. This difference is greater than the EXAFS resolution limit ($\Delta R = \pi / 2\Delta k = 0.196$ Å).[62,176] The best fit spectra for **OH, OMe, OAc** and **OBz** are shown in Figure 4.7. Except for **OBz**, these O cubanes were reasonably fit with four distinct shells: two each of oxygen, and two of Mn. N and F are normally indistinguishable from O by EXAFS, so the μ_3-X atom was combined into the longer Mn–O interaction (~ 2.2 Å). The best fit spectra for **N$_3$** and **F** appear in Figure 4.8. For the most highly distorted cubane **OBz**, five shells were needed to describe the core: two shells of O (1.9 Å and 2.2 Å) and three shells of Mn (2.8 Å, 3.2 Å, and 3.4 Å). Again, the differences in distances are above the resolution limit, allowing us to distinguish the three Mn shells. The fit error is reduced by 40% when the fifth shell is included. The heterogeneity in the longer Mn–Mn distance allows the peak III to be separated from peak II. In general, peak II (and III for **OBz**) consists of two sets of Mn–Mn distances: a short one ($N = 1.5$) at 2.79 - 2.83 Å and a longer one ($N = 1.5$) at 3.12 - 3.37 Å. The model compounds with

Table 4.2 Least-Squares Best Fits Of Filtered Peak I-II-(III) from Mn Cubanes.

Compound	Fit #	Atom	R (Å)	N	σ^2 •10^3	ΔE_0 (eV)	Φ •10^3	ε^2 •10^5	XRD R(Å)	XRD N
$\mathrm{Mn_4O_3(\mathbf{OBz})(OBz)_3(dbm)_3}$	1	O	1.91	4.75	3	-7	0.41	0.43	1.93	4.75
		Mn	2.82	1.5	2				2.79	1.5
		Mn	3.16	0.5	2				3.18	0.5
		Mn	3.38	1.0	2				3.37	1.0
"	2	O	1.91	4.75	3	-7	0.24	0.30	1.93	4.75
		O	2.20	1.25	2				2.20	1.25
		Mn	2.81	1.5	2				2.79	1.5
		Mn	3.17	0.5	2				3.18	0.5
		Mn	3.39	1.0	3				3.37	1.0
$\mathrm{Mn_4O_3(\mathbf{OAc})(OAc)_3(dbm)_3}$	3	O	1.90	4.5	2	-13	0.26	0.25	1.92	4.5
		O	2.24	1.5	5				2.23	1.5
		Mn	2.81	1.5	2				2.80	1.5
		Mn	3.17	1.5	2				3.20	1.5
$\mathrm{Mn_4O_3(\mathbf{OMe})(OAc)_3(dbm)_3}$	4	O	1.90	4.5	2	-13	0.25	0.25	1.92	4.5
		O	2.20	1.5	4				2.19	1.5
		Mn	2.80	1.5	2				2.80	1.5
		Mn	3.12	1.5	2				3.13	1.5
$\mathrm{Mn_4O_3(\mathbf{OH})(OAc)_3(dbm)_3}$	5	O	1.90	4.5	3	-13	0.22	0.20	1.91	4.5
		O	2.19	1.5	2				2.21	1.5
		Mn	2.80	1.5	2				2.79	1.5
		Mn	3.08	1.5	2				3.12	1.5
$\mathrm{Mn_4O_3(\mathbf{N_3})(OAc)_3(dbm)_3}$	6	O	1.90	4.5	2	-13	0.19	0.17	1.91	4.5
		O(N)	2.23	1.5	7				2.24	1.5
		Mn	2.81	1.5	2				2.80	1.5
		Mn	3.16	1.5	3				3.19	1.5
$\mathrm{Mn_4O_3\mathbf{F}(OAc)_3(dbm)_3}$	7	O	1.90	4.5	2	-13	0.20	0.19	1.91	4.5
		O(F)	2.19	1.5	5				2.20	1.5
		Mn	2.79	1.5	2				2.79	1.5
		Mn	3.12	1.5	4				3.15	1.5
$\mathrm{Mn_4O_3\mathbf{Cl}(OAc)_3(dbm)_3}$	8	O	1.91	4.5	4	-8	0.31	0.39	1.91	4.5
		O	2.15	0.75	2				2.17	0.75
		Cl	2.61	0.75	2				2.65	0.75
		Mn	2.81	1.5	4				2.80	1.5
		Mn	3.24	1.5	5				3.25	1.5
$\mathrm{Mn_4O_3\mathbf{Cl_4}(OAc)_3(py)_3}$	9	O	1.87	3.0	10	-15	0.38	0.41	1.93	3.0
		Cl	2.22	0.75	6				2.24	0.75
		Cl	2.58	0.75	2				2.63	0.75
		Mn	2.77	1.5	4				2.82	1.5
		Mn	3.24	1.5	4				3.27	1.5
$\mathrm{[Hpy]_3Mn_4O_3\mathbf{Cl_7}(OAc)_3}$	10	O	1.92	3.0	7	-11	0.17	0.18	1.93	3
		Cl	2.28	1.5	3				2.27	1.5
		Cl	2.62	0.75	2				2.63	0.75
		Mn	2.82	1.5	3				2.83	1.5
		Mn	3.28	1.5	6				3.30	1.5
$\mathrm{Mn_4O_3\mathbf{Br}(OAc)_3(dbm)_3}$	11	O	1.91	4.5	3	-10	0.17	0.21	1.91	4.5
		O	2.20	0.75	3				2.16	0.75
		Br	2.70	0.75	3				2.80	0.75
		Mn	2.86	1.5	2				2.79	1.5
		Mn	3.27	1.5	5				3.28	1.5

Compound	Fit #	Atom	R (Å)	N	σ^2 $\bullet 10^3$	ΔE_0 (eV)	Φ $\bullet 10^3$	ε^2 $\bullet 10^5$	XRD R(Å)	XRD N
PS II (S_1 state)	12	O	1.86	2.5	6	-14	0.35	0.25		
		Mn	2.73	1.0	2					
		Mn	3.31	0.5	4					

For the model compounds EXAFS results are compared to interatomic distances reported from x-ray diffraction data (XRD; See References in Table 4.1). *N* is fixed to known values from XRD data. Fit parameters are as defined in the text, with $S_0{}^2 = 0.85$ in all fits.

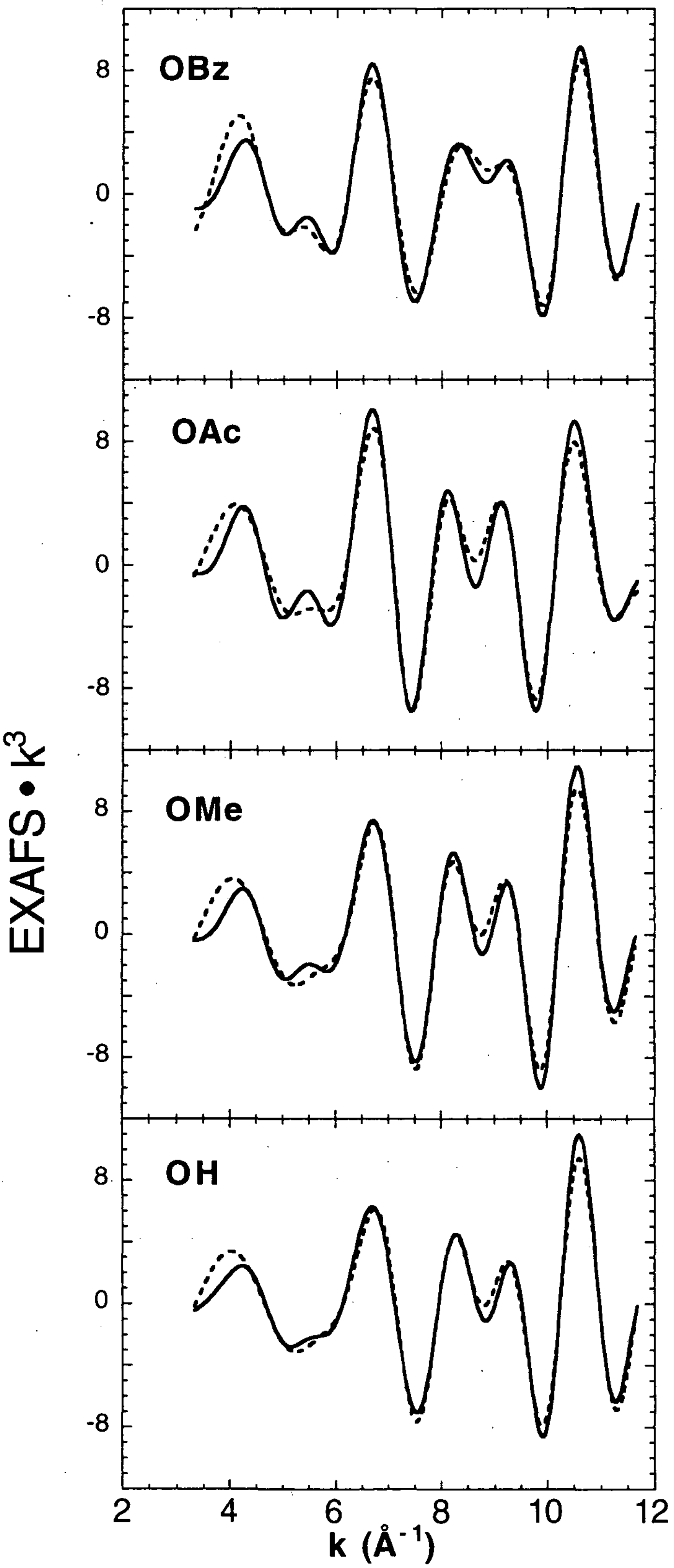
OBz
OAc
OMe
OH
EXAFS • k^3
8
0
-8
2
4
6
8
10
12
k (Å^{-1})

Figure 4.7 Simulation (---) of Fourier transform peaks I, II and III plotted over the Fourier-filtered *k*-space EXAFS (—) of **OBz**, **OAc**, **OMe**, and **OH**. Fits were generated as described in the text and Table 4.2 (Fit Labels 2, 3, 4, and 5, respectively).

smaller differences between these two vectors, such as **OMe** (0.31 Å), **OAc** (0.35 Å), **OH** (0.28 Å), $\mathbf{N_3}$ (0.35 Å), **Br** (0.39 Å) and **F** (0.30 Å) show only a shoulder on the right side of peak II (Fig. 4.6). However, the cubanes with larger differences, such as **Cl** (0.45 Å), $\mathbf{Cl_4}$ (0.46 Å) and $\mathbf{Cl_7}$ (0.45 Å), peak II begins to be resolved. The cubane with the largest difference between the Mn–Mn vectors, **OBz** (0.56 Å), has the most clearly resolved peak III (Fig. 4.6A).

For the halide cubanes **Cl**, **Br**, $\mathbf{Cl_4}$ and $\mathbf{Cl_7}$, there are distinct halide shells, which were detected by EXAFS: terminal Cl at 2.2 - 2.3 Å, and bridging Cl^- (or Br^-) at 2.6 - 2.7 Å (Table 4.2 and Figure 4.9). Except for the Mn–Br vector, these distances were determined to within ± 0.05 Å of the known values (Table 4.2). We found that for $\mathbf{Cl_4}$ and $\mathbf{Cl_7}$, five shells could adequately describe the EXAFS spectra; the sixth shell of longer Mn–O (2.2 Å) either did not improve the ε^2 error or gave unrealistic distances. For comparison, the fit to the filtered data for PS II, using results derived previously[25] is shown in Fig. 4.8. In this simplistic three-shell fit, the distances for the O shell (1.85 Å) and the 2.7 Å Mn–Mn shell are shorter than those found in the Mn cubanes. The derived coordination numbers for PS II are smaller than their counterparts in the Mn cubanes, accounting partly for the reduced amplitude in the EXAFS and FT.

To assess the accuracy of the method in determining coordination numbers for the crucial metal–metal vectors, we isolated the Fourier peak II (with peak III, when applicable) and simulated with short (~ 2.8 Å) and long (~ 3.2 Å) Mn–Mn distances. In the previous whole-spectrum fits (Table 4.2), the coordination numbers were fixed to known values to avoid underdetermined fits and reduce complexity. For the isolated peak II fits, though, *N* is allowed to vary and the cubanes are treated as "unknown" structures in a similar manner as PS II. These unrestrained fits allow us to

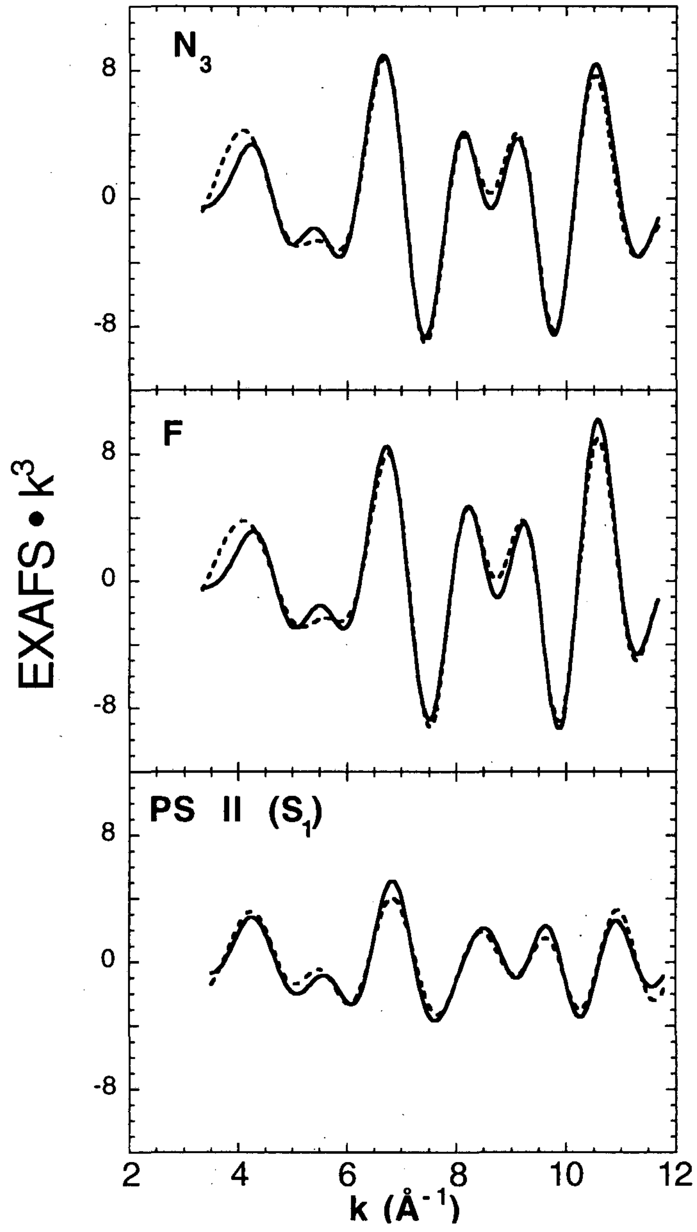

Figure 4.8 Simulation (---) of Fourier transform peaks I, II and III plotted over the Fourier-filtered *k*-space EXAFS (—) of N_3, **F** and PS II. Fits were generated as described in the text and Table 4.2 (Fit Labels 6, 7, and 12, respectively).

compare directly the *N* from the PS II and the cubanes, and gauge the uncertainty associated with this parameter for the crucial Mn–Mn vectors. The fitting results are presented in Table 4.3. Except for **OBz**, only two shells (long and short Mn–Mn) are used to reduce the complexity and avoid underdetermined fits resulting from too many floating parameters. Also, only the six "O" cubanes were simulated to avoid interference and complications (more shells) introduced by the Mn–halide vector in the Mn "halide" cubanes (**Cl**, **Br**, **Cl_4**, and **Cl_7**). These "O" cubanes are compared directly with a similar unrestrained *N* fit for PS II in Table 4.3, and similar trends can be expected for the halide cubanes.

Table 4.3 shows that the unrestrained *N* for the Mn–Mn 2.8 Å vector differs from the known values by an average of 13%, up to a maximum deviation of about 30%. Likewise, the *N* for the longer Mn–Mn (~ 3.2 Å) vector deviates from the true *N* by an average of 18%, also with maximum error of 30%. These uncertainties for the coordination numbers agree with previously discussed limitation of the EXAFS technique.[25,62] In comparing these unconstrained *N* fits of the Mn "O" cubanes with PS II, we find the *N* for the Mn–Mn 2.8 Å vector are almost always larger than that from PS II, while the $N_{3.2Å}$ are always greater than the corresponding PS II vector. Even allowing for the maximum possible error in *N*, the discrepancy in the coordination numbers for the Mn–Mn distances between the Mn cubanes and PS II remain significant and sizable. Accordingly, the ratio between the long and short Mn–Mn vectors for PS II is twice that of the cubanes.

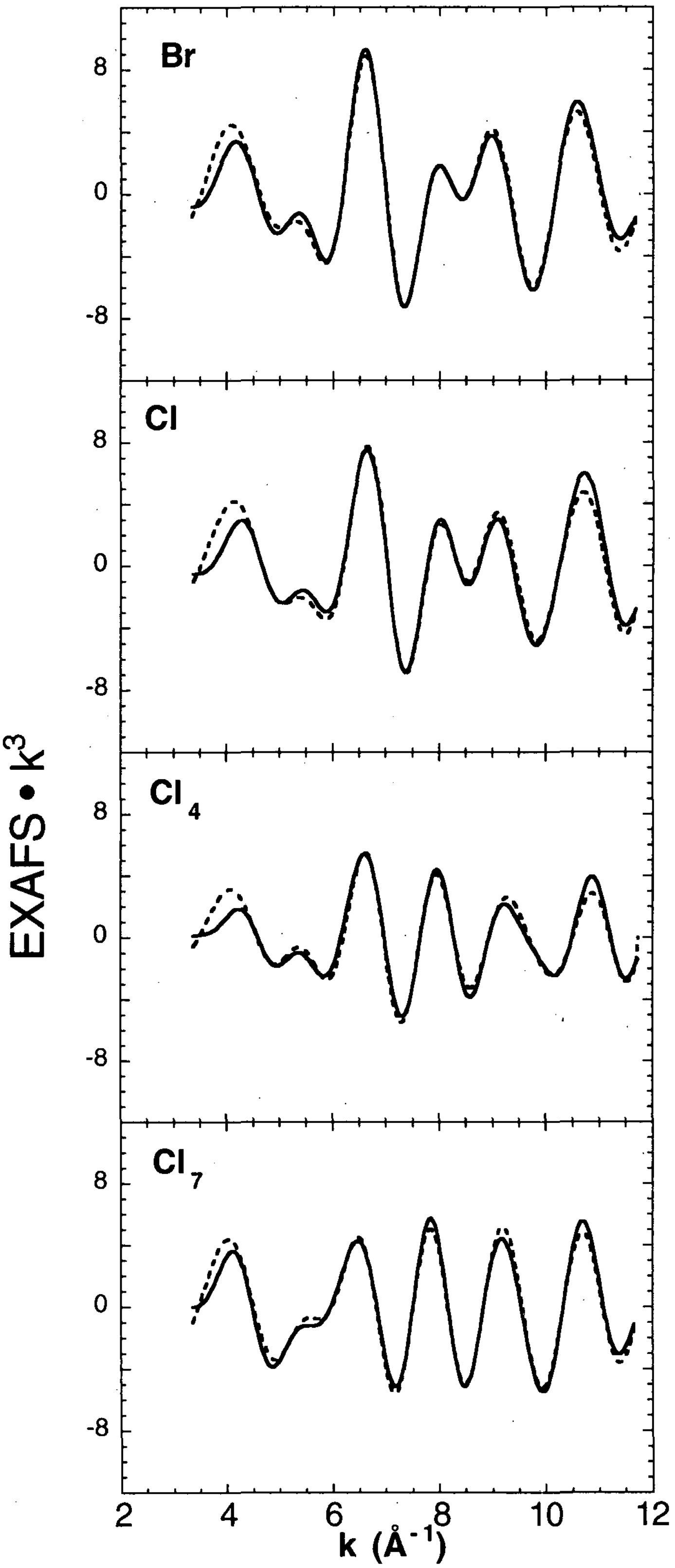
Br
Cl
Cl 4
Cl 7
8
0
-8
8
0
-8
8
0
-8
8
0
-8
EXAFS • k3
2
4
6
8
10
12
k (Å-1)

Figure 4.9 Simulation (---) of Fourier transform peak I, II and III plotted over the Fourier-filtered *k*-space EXAFS (—) of **Br**, **Cl**, **Cl_4**, **Cl_7**. Fits were generated as described in the text and Table 4.2 (Fit Labels 11, 8, 9 and 10, respectively).

Discussion

Mn XANES Spectra

The O cubanes (**OH, OMe, OAc**, and **OBz**) along with **F** and **N_3** exhibit Mn K-edge spectra superficially similar to that of PS II (S_1 state, Fig. 4.3A), and the edge positions fall between those of the S_0 and S_1 states (Table 4.1). The qualitative similarity may be due in part to the absence of Mn^{II} and the nearly exclusive O ligation environment. This O ligation is a property that these cubanes share with PS II, although PS II has a histidine ligand.[177] The presence of aromatic N ligands (such as pyridine) adds more structure to the edge, altering the edge shape considerably to make it distinct from that of PS II (see Appendix 3). The qualitative similarity in the XANES is not present in the second derivative spectra (Fig. 4.4), which are all distinct from that of PS II and indicate strongly the presence of Mn^{III}.[19] This is not surprising, because the oxidation state distributions are different: PS II (S_1) has two Mn^{III} and two Mn^{IV} whereas the cubanes have three Mn^{III} and one Mn^{IV} present. The XANES from the halide cubanes look different from PS II, especially in the edge shift to lower energy (Table 4.2, Figs. 4.3B-C and 4.4B-C). The lower energy is indicative of halide ligation, because the presence of the electronegative halide reduces the x-ray energy required to ionize the K-shell (1*s*) electron. The presence of bridging Cl in the **Cl** cubane lowers the edge energy more than does the addition of terminal Cl ligands in **Cl_4** and **Cl_7** (Figs. 4.3C, 4.4C, Table 4.1), probably because the bridging Cl provides more covalency in the Mn–Cl bond than does the terminal Cl.[178]

Mn EXAFS and FT

Superficial similarities in the FTs between the cubanes and PS II mostly fade in light of the EXAFS and in subsequent curve-fitting. Upon comparing the k^3-weighted EXAFS from **OBz, OAc, OMe, OH, N$_3$** and **F** among themselves and to PS II (Fig. 4.5A), the differences are immediately apparent. Although the Mn cubanes simulate the oscillation pattern of PS II, because they contain both ~ 2.8 Å and ~ 3.2 Å vectors, the normalized amplitudes are larger and are phase-shifted at $k = 8 - 11$ Å^{-1}. The EXAFS from the O cubanes (Fig. 4.5A, except **OBz**) are very similar to one another and to **F** and **N$_3$**, while only the most distorted one (**OBz**) stands out, especially at $k = 8.5$ Å^{-1}. Among the halides, **Br** is distinguishable from **Cl** by the pattern at $k = 8 - 9$ Å^{-1} (Fig. 4.5B), while the **Cl$_4$** and **Cl$_7$** have oscillation patterns distinct from the rest of the Mn cubanes and from PS II (Fig. 4.5C). Thus from the EXAFS spectra, the three categories of cubanes now divide into four: 1) **OMe, OH, OAc, N$_3$, F**; 2) **OBz**; 3) **Cl, Br**; and 4) **Cl$_4$, Cl$_7$**. None of these categories reproduces the observed PS II EXAFS spectrum (S_1) in amplitude or phase.

In the analysis of the Mn EXAFS, we obtained reasonably good fits by using single-scattering, theoretical FEFF-generated phases and amplitudes, and focusing only on the core structure of the cubane. Once the coordination numbers were fixed to known values, we obtained highly accurate distances, to within ± 0.05 Å of the known values (except for **Br**). By using only four to five shells of scatterers, we could accurately describe the EXAFS spectra of the cubanes (Figs. 4.7 - 4.9). In particular we could resolve the three Mn–Mn vectors in **OBz**, where two such vectors are 0.56 Å apart, leading to a resolved peak III. EXAFS could also detect the Mn–Cl (Br) bridging interaction in **Cl$_4$**, **Cl$_7$**, **Cl** and **Br**, and the terminal Cl ligands in **Cl$_4$** and **Cl$_7$** at 2.22 Å (3 Cl) and 2.27 Å (6 Cl), respectively.

In the Fourier transforms (Fig. 4.6), only **OBz** shows a clearly resolved peak III comparable to that of PS II, but at longer distance. In the other model compounds, peak III appears mostly as a shoulder of peak II. The most obvious difference between the cubanes and PS II is the larger magnitude of peaks I and II; only **Cl_4** approaches PS II in FT magnitude (Fig. 4.6C), but its EXAFS is very different. Also, even though **OBz** has three peaks like PS II, its EXAFS amplitude and FT magnitude exceed that of PS II. In addition, the FTs for **Cl_4** and **Cl_7** (Fig. 4.6C) reveal the presence of a significant scattering contribution between peak I and II (a shoulder at 'R'' = 1.9 - 2.0 Å) arising from 3 or 6 terminal Cl ligands, respectively. For the distorted cubanes, peak I appears at a longer distance in the FT than the corresponding peak in PS II and indicates there must be more μ_2-oxo bridging in PS II. The μ_3-O bridges in the cubanes give relatively longer Mn–O distances. Peak I is also larger because of the greater number of Mn–O (short) distances in the cubanes (4.5 vs. 2.5, Table 4.2). The non-bridging Mn–O distances in the PS II may also be more disordered compared to the cubanes so that only the shorter μ-oxo bridges are detected, while in the cubane EXAFS, both the long and short Mn–O bonds contribute.

The ratio of first to second Fourier peaks (Fig. 4.6) cannot be used to assign either the arrangement of the Mn atoms or the number of Mn–Mn distances. The intensity of the first peak depends on the number and distribution of bridging and terminal ligand distances. Unlike the case of Fe–S clusters, where the ratio of first-to-second peaks suggests the ratio of Fe–S to Fe–Fe vectors,[179] such a first-to-second peak ratio does not necessarily predict the number of Mn–O to Mn–Mn vectors for either PS II or the cubanes. The number of Fe–S vs. Fe–Fe vectors correlate with the first-to-second peak ratios because of the very similar distances of bridging and terminal Fe–S bonds (within 0.1 Å).[180,181] In the case of the Mn clusters, however, the bridging and terminal Mn–O distances are distributed over a wider range (0.3 Å; see Table 4.2). This distribution of distances, summarized in the Debye-Waller factor in the EXAFS equation (Eq. 4.2), leads to destructive interference from these O ligands that attenuates and broadens the first Fourier peak. Hence, such relative similarity in Fourier peak ratios here is incidental and does not imply that PS II and the cubanes share similar numbers of Mn–O and Mn–Mn vectors. Only through curve-fitting of the *k*-space EXAFS (and not Fourier peak heights alone) can these Mn–O vs. Mn–Mn ratios and numbers be derived quantitatively (Table 4.2 and 4.3).

There is also a large difference in peak II intensity compared to PS II (Fig. 4.6). In the cubanes, there is a short Mn–Mn vector ($N_{\text{short}} = 1.5$) at 2.8 Å and a longer Mn–Mn ($N_{\text{long}} = 1.5$) at 3.2 - 3.3 Å. This pattern is different from the "dimer-of-dimers" model, which gives a 2.7 Å Mn–Mn vector ($N_{\text{short}} = 1.0$) and a longer one at 3.3 Å ($N_{\text{long}} = 0.5$). The disparity in the amplitudes of the Fourier transforms in Fig. 6 cannot simply be explained by invoking more disorder in the native OEC. Rather, the Fourier peak II amplitude is larger because $N_{2.8\text{Å}}$ is greater (1.5 > 1.0) and there is contribution from the nearby longer Mn–Mn distance: $N_{3.2\text{Å}} = 1.5$. Although the distances of Mn–Mn vectors are similar, the distribution of N dictates the arrangement of short and long Mn–Mn distances and serves to differentiate the possible models for PS II as depicted in Fig. 4.1. By comparing such N patterns, we can exclude the distorted cubane with C_{3v} symmetry as a structural analog to the native Mn cluster. This is consistent with the $S = 9/2$ ground states of these species which already showed structural non-congruence with the OEC.[158-160]

To focus on the crucial Mn–Mn vectors, we isolated Fourier peak II from the rest of the EXAFS and simulated it with long and short distances. By not constraining N to crystallographic values, we tested the accuracy of determining coordination numbers through EXAFS. A more balanced comparison between the cubanes and PS II was then made by treating both as "unknown" structures (regarding the Mn–Mn vectors). As Table 4.3 shows, even when N is allowed to float freely during the fits, the observed coordination numbers do not deviate much from the true values. Observed errors range from averages of 13% (N_{short}) and 18% (N_{long}) up to a maximum of 30%. These are within the limitations of the EXAFS technique as determined previously.[25,62] Despite these errors in N, the disparities in Mn–Mn vectors between the Mn cubanes and PS II remain significant. Except for **OBz**, in the "O" cubanes, the ratio of N_{short} to N_{long} approaches one whereas the PS II ratio is closer to two. In addition, the absolute values of N are almost always larger in the cubanes. This shows that the C_{3v} distorted cubanes are still too symmetric to resemble the OEC active site.

Even though this study has shown that the C_{3v} Mn cubanes cannot be a structural analog for the OEC, the cubanes do point to future synthetic approaches for modeling the OEC active site. Clearly, more distortion in the cubane framework is needed, as shown by the **OBz** cubane, whose EXAFS and FT come closest (out of the ten) to resembling those of PS II. Future synthetic biomimetic efforts should focus on adding even more distortion, to alter the ratio of long to short Mn–Mn distances. Also, the nearly exclusive oxygen ligation (except for **Cl_4** and **Cl_7**) present in these cubanes is a positive advance that should continue to be incorporated in subsequent models.

We have shown through a combination of *k*-space Mn EXAFS, Fourier transform, and curve-fitting analyses, that the distorted-cubane model of C_{3v} symmetry is excluded as a topological model for the Mn cluster in the OEC. Of the ten cubane complexes studied, only the most distorted (**OBz**) comes closest to resembling PS II, emphasizing the need for even more distortion of the cubane framework in order to approach the observed OEC data. Among the remaining topological possibilities, the "dimer-of-dimers" model continues to be favored, for reasons discussed previously.[25] We have shown the ability of EXAFS to verify the known core structure of these cubanes, by starting from theoretical phases and amplitudes and using only the simple core structure to simulate the experimental spectra. Mn EXAFS also is able to detect small changes in the cubane structure in going from the oxygen cubanes (**OAc, OMe, OH, F, $\mathbf{N_3}$**) to the halide cubanes (**Cl, Br**), to the multiple-halide cubanes (**$\mathbf{Cl_4}$, $\mathbf{Cl_7}$**) and finally to the most distorted **OBz**. Just as EXAFS has been employed to determine the degree of discrepancy between the C_{3v}-symmetry distorted cubane and the OEC, this tool can be used to test other synthetic bioinorganic complexes for their resemblance and relevance to the Mn cluster in PS II.

Table 4.3 Best Fits Of Filtered Peak II for the "O" Cubanes and PS II.

Compound	Fit #	Atom	*R* (Å)	*N*	σ^2 • 10^3	ΔE_0 (eV)	Φ • 10^3	ε^2 • 10^5	XRD *N*
Mn_4O_3(**OBz**)$(OBz)_3(dbm)_3$	13	Mn	2.84	1.9	1	-1	0.165	2000	1.5
		Mn	3.01	0.33	2				0.5
		Mn	3.41	1.1	6				1.0
"	14	Mn	2.83	1.7	1	-3	0.15	0.24	1.5
		Mn	3.41	1.3	7				1.5
Mn_4O_3(**OAc**)$(OAc)_3(dbm)_3$	15	Mn	2.82	1.8	1	-9	0.14	0.28	1.5
		Mn	3.19	1.4	2				1.5
Mn_4O_3(**OMe**)$(OAc)_3(dbm)_3$	16	Mn	2.83	1.8	1	-5	0.20	0.45	1.5
		Mn	3.14	1.0	2				1.5
Mn_4O_3(**OH**)$(OAc)_3(dbm)_3$	17	Mn	2.79	1.2	1	-20	0.22	0.36	1.5
		Mn	3.06	1.7	1				1.5
Mn_4O_3(**N_3**)$(OAc)_3(dbm)_3$	18	Mn	2.81	1.5	1	-11	0.15	0.20	1.5
		Mn	3.18	1.4	3				1.5
Mn_4O_3**F**$(OAc)_3(dbm)_3$	19	Mn	2.78	1.4	1	-20	0.19	0.36	1.5
		Mn	3.12	1.3	1				1.5
PS II (S_1 state)	20	Mn	2.74	1.3	3	-11	0.18	0.26	
		Mn	3.32	0.6	4				

For the "O" cubanes, Mn EXAFS results are compared to coordination numbers reported from x-ray diffraction data (XRD *N*; See references in Table 4.1). *N* is allowed to float in these fits, and is not fixed as in Table 4.2. Fit parameters are defined in the text. $S_0^2 = 0.85$ in all fits. For **OBz**, the three-shell fit is technically underdetermined and not unique (large ε^2).

Chapter 5 — Sulfur K-edge X-ray Absorption Spectroscopy Examines the Redox State of Biologically Relevant Sulfur Compounds

Introduction

This chapter describes an application of sulfur K-edge X-ray absorption spectroscopy (XAS) to determine the ratio of thiol to disulfide in biological systems. Sulfur is an important element in biochemistry and often it is desirable to assay thiols and disulfide and their ratio in biological samples. Previously, there had been no spectroscopic techniques available that can distinguish between thiol- and disulfide-sulfur, or sulfur in higher formal oxidation states. This is not surprising, because there are no significant optical markers for sulfur. Also, only one sulfur isotope of < 1 % natural abundance has a nuclear magnetic moment; but this isotope possesses an unfavorable nuclear spin with a small magnetic moment and a large quadrupole moment, making NMR unattractive for sulfur analysis.

Sulfur K-edge XAS has been shown to exhibit a strong correlation between oxidation state and inflection point energy as well as rich x-ray absorption near edge structure (XANES) that is related to chemical structure[182-185] and can be used to distinguish between thiol- and disulfide-sulfur. The two sulfur-containing amino acids found in all cells are cysteine and methionine. Cysteine can be oxidized to the disulfide form cystine. Additionally there are "mixed" disulfides (cysteine bound to proteins by formation of a disulfide linkage). Methionine can be reversibly oxidized by $HO^{\bullet}$, $^{1}O_2$, or H_2O_2 to the sulfoxide or even further to the sulfone.[186]

The number and importance of enzymes and proteins, whose function has been found to be severely modified by the oxidation of their thiol-containing amino acids, is growing rapidly. The reversible oxidation-reduction of thiol groups is intimately linked to oxidative stress in a number of respects. In the case of cysteine and glutathione the formation of disulfide bonds as such can not be considered as damage, because it is a reversible process, but disulfide bridges in peptides and proteins may drastically alter biological functions. Alteration in the thiol/disulfide status, for example, has been found to lead to biological consequences, including changes in enzyme properties (K_m or v_{max} effects).[187] Thus the thiol redox status seems to serve as a metabolic signal. There are many enzymes and proteins whose activities are reported to be protein modulated by mixed disulfide formation or changes in GSH:GSSG ratio, such as liver phosphorylase phosphatase,[188] pineal indoleamine N-acetyltransferase,[189] glycogen synthase,[190,191] thiol proteinase inhibitor,[192] adenylate cyclase,[193,194] guanylate cyclase,[195] 3-hydroxy-3-methylglutaryl-CoA reductase,[196] carbonic anhydrase I[197] and phosphofructokinase.[198] Oxidation of methionine to methionine sulfoxide can be associated with the loss of function; a particularly striking example is that of antitrypsin.[199]

The most abundant molecule containing cysteinyl-thiol in animal cells is glutathione. Glutathione (GSH) is a tripeptide γ-L-glutamyl-L-cysteinyl-glycine with cellular concentrations in the range 0.1 - 10 mM. Glutathione is a component of a pathway that uses reduced nicotinamide-adenine dinucleotide phosphate (NADPH) to maintain the cellular redox state. It has an essential role in maintaining various components of cells in their reduced state. Furthermore it is involved in the reduction of ribonucleotides to deoxyribonucleotides (precursors of DNA) and is implicated in protecting the cell against oxidative damage, free radical damage and in detoxification via a conjugation mechanism.[200] In its "free" form it is present intracellularly, mainly in the thiol-reduced form (GSH). The ratio between the oxidized (GSSG) and the reduced (GSH) forms is kept at a low value, approximately 0.1, in normal cells.[201] Glutathione may exist in many forms as GSH, GSSG, glutathione mixed disulfides with low-molecular-weight compounds (e.g., cysteine) and with high-molecular-weight substances (e.g., peptides and proteins). The level of oxidized to reduced glutathione can change significantly upon oxidative stress and provides useful information about the redox and detoxification status of cells and tissues.[202-205]

Several procedures for the determination of GSH and GSSG from different biological sources have been reported in the literature, but all require extraction procedures for the determination of glutathione in biological materials. An *in situ* determination is not possible with chemical[206] and enzymatic[207-209] methods, high-performance liquid chromatography,[210-219] flow cytometry[220-222] and, more recently, capillary electrophoresis (CE)[223,224]. GSH and GSSG can be detected using spectrophotometric,[225,226] spectrofluorimetric[227-231] and electrochemical methods[211,215,218,232-236] with levels of sensitivity ranging from nmol[214,216] to pmol.[212,213] For spectrophotometric detection glutathione extracts are treated with iodoacetate to block free thiol groups and then with Sanger's reagent (as one example) to produce a N-dinitrophenyl derivative that is analyzable. Neither GSH nor GSSG, as such, have significant intrinsic fluorescence.[237] Some complexes and some covalent or other derivatives of GSH and GSSG, however, have fluorescent properties, and the fluorescence and fluorescence quenching of these derivatives can be used for determination of GSH and GSSG levels. However, a difficult problem in determining glutathione levels is the sample and standard preparation. Sample preparation, protein precipitating agents, and sample treatment must be carefully considered, because the oxidation of glutathione to glutathione disulfide, including protein mixed disulfides, must be minimized; otherwise erroneously low values of glutathione and high values of glutathione disulfide and mixed disulfides will be obtained.[238-240] The difficulties associated with existing procedures, especially for use *in vivo*, led us to investigate a method to measure thiol and disulfide levels in cells without any prior chemical treatment. An optimal sample preparation procedure for measuring the RSH and RSSR levels in erythrocytes, plasma and blood would be fast freezing of freshly taken samples. We show that sulfur K-edge XAS, on such samples, allows a determination of thiol, disulfide (GSSG and GSSR), sulfoxide and sulfone sulfur *in vivo*.

In whole blood, plasma and red blood cells the two major thiol and disulfide components are glutathione and cyst(e)ine. The major sulfur-containing constituents of whole blood are glutathione (~34 mg / 100 ml), cysteine (~0.9 mg / 100 ml), methionine (~0.5 mg / 100 ml) which are there in free form as well as part of proteins. Additionally there is sulfate (~1.0 mg / 100 ml).[241] Whole blood is mostly a mixture of red blood cells (erythrocytes) and blood plasma. In red blood cells the level of cyst(e)ine is at least one order of magnitude lower than the glutathione concentration.[242,243] This cyst(e)ine/glutathione ratio is reversed in blood plasma.[244,245]

Sulfur K-edge XAS spectra have been collected and the redox state of sulfur in whole blood, as well as separated plasma and red blood cells has been determined. The sulfur K-edge spectra of reduced/oxidized forms of the amino acids cysteine/cystine and methionine/methionine sulfoxide as well as reduced/oxidized glutathione are also reported.

Experimental Section

Sample Preparation

Cysteine, cystine, methionine, methionine sulfoxide, reduced glutathione and oxidized glutathione were of reagent grade, purchased from Sigma and used as received. A small amount (mg) of each compound was ground into a fine powder and dispersed as thinly as possible (over about 1 cm^2) on Mylar tape. The compounds were run at successively lower concentrations until a reproducible spectrum was obtained, to avoid spectral distortion and loss of resolution due to self-absorption in the sample.

Whole human blood was collected in heparin-coated syringes and centrifuged for 5 min at 2500*g* by Dr. Diane L. Tribble and Lillie Taat (directed by Dr. Ronald M. Krauss, Life Sciences Division, LBNL). Whole blood, erythrocytes or blood plasma samples were placed in sample holders (Lucite frames with inner dimensions 18 × 2.5 × 0.8 mm, backed with Mylar tape), and frozen in liquid nitrogen immediately after collection.

Sulfur XANES Data Collection

Sulfur K-edge XANES spectra were recorded at SSRL using the 54-pole wiggler beamline VI-2, with a Pt-coated focusing mirror and a Si[111] double crystal monochromator. Details of the setup have been described earlier.[182-185,246,247] All sulfur K-edge spectra were run with sample between 130 – 140 K in a home-built liquid He flow cryostat designed by Matthew Latimer, using Aerogel insulation and polypropylene windows (ChemPlex Industries). The data were collected as fluorescence excitation spectra with a N_2-filled Lytle detector.[168,248] Scans were run from 2420 to 2740 eV, with a step size of 0.08 eV from 2465 to 2495 eV to obtain high resolution (~0.5 eV) in the pre-edge and edge region and a step size of 1.0 eV in the other regions. For each compound two to four scans were collected. The energy was calibrated from the sulfur K-edge spectra of $Na_2S_2O_3{\cdot}5H_2O$ (Sigma), run after every two sample scans. The maximum of the first pre-edge feature in this spectrum occurs at 2472.02 eV.[246] Reproducibility of the sulfur K-edge energies with the above conditions have been found to be ± 0.1 eV.[246]

A pre-edge background was removed from all spectra by fitting a straight line to the pre-edge region and subtracting this straight line from the entire spectrum. Normalization of the spectra was achieved by extrapolating into the edge region a quadratic fit to the data in the far post-edge region. Each spectrum was then multiplied by a factor so that the value of the extrapolated line was unity at the energy of the first absorption peak. The position of the main edge was defined by the first inflection-point energy (IPE) of the steeply rising absorption edge, determined from the zero-crossing of the second derivative of the spectrum. Analytical differentiation of a third-order polynomial fit to the data over an interval of 2.0 eV on each side of a data point produced the derivative spectra.

For erythrocytes, plasma and whole blood, simulations were compared with the original data in the region from 2471 to 2475 eV by following a least squares method. A limited range of energy around the IPE was used in the simulation to reduce the effects of scattering from more distant atoms, EXAFS and multiple-scattering effects that contribute at higher energies. Percentages of the two constituent spectra (GSH and GSSG) were combined to form a simulated spectrum. The sum of the squares of the residuals between the original data and the simulation was designated the error and referred to as the residuals in the figures. The method of combination of edges in a least squares method to determine respective amounts of a component has been used previously.[249] The linear combination, in percentages of GSH and GSSG, found to give the minimum error (least squares) was judged to be the best fit of the data. The uncertainty is estimated to be ± 5%. The plots of residuals are shown as insets in the figures.

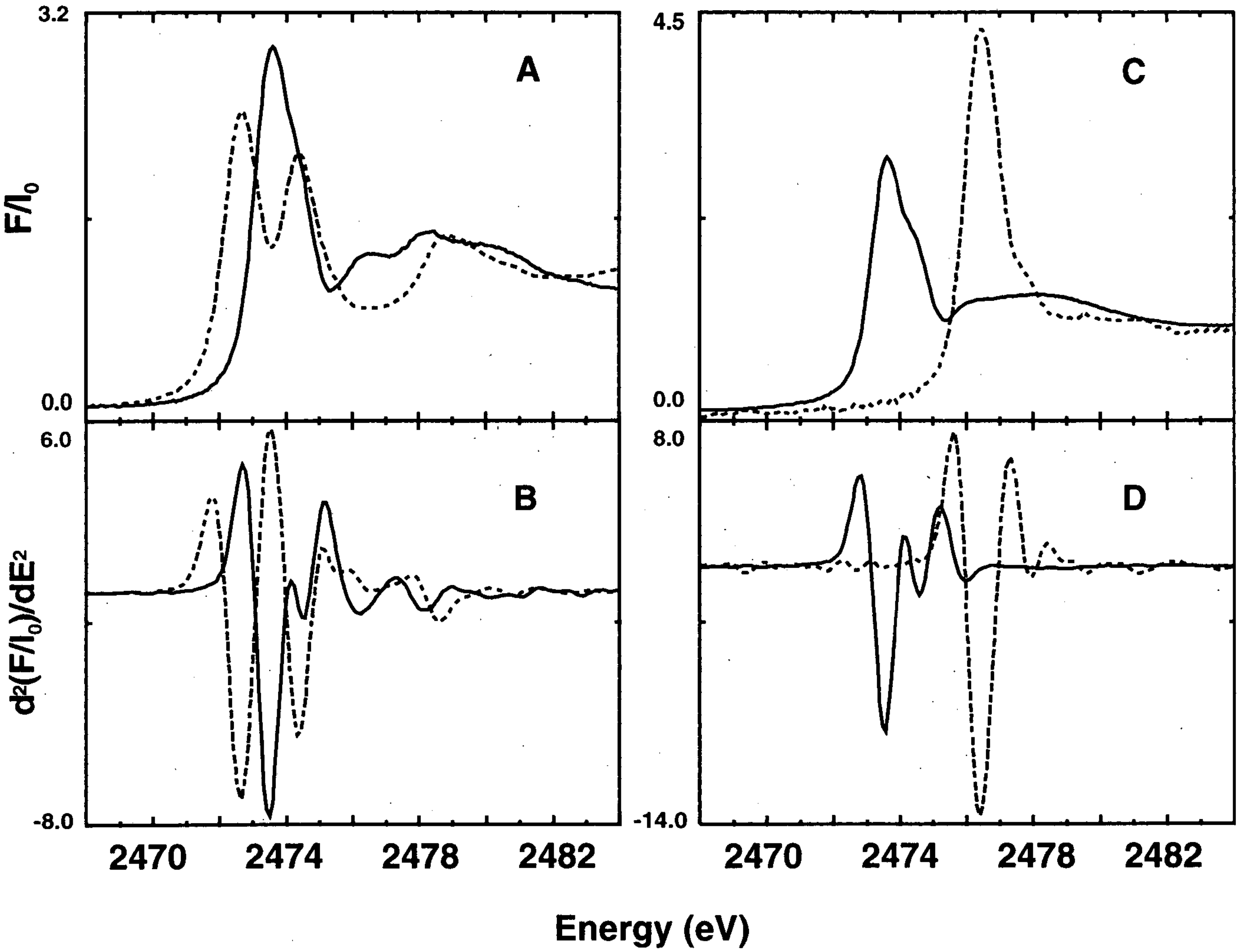
3.2
A
F/I$_0$
0.0
4.5
C
0.0
6.0
B
d^2(F/I$_0$)/dE^2
-8.0
8.0
D
-14.0
2470
2474
2478
2482
2470
2474
2478
2482
Energy (eV)

Figure 5.1 Sulfur XANES from amino acids.

(**A**) Normalized S K-edge X-ray absorption spectra of cysteine (—) and cystine (---).

(**B**) Second derivatives of cysteine (—) and cystine (---).

(**C**) Normalized S K-edge X-ray absorption spectra of methionine (—) and methionine sulfoxide (---).

(**D**) Second derivatives of methionine (—) and methionine sulfoxide (---).

All sample materials were in the form of solids.

Results

Sulfur-containing Amino Acids

The sulfur K-edge X-ray absorption near-edge spectra of the thiol cysteine and thioether methionine are shown in Figure 5.1. The IPE for cysteine and methionine, 2473.1 eV, are the same (Table 5.1). The oxidized form of cysteine is cystine, a disulfide. The IPE changes to 2472.1 eV for cystine. The S XANES spectra of cysteine and cystine are clearly different (Fig. 5.1A). For cystine the intense white line absorption maximum is split into two features with almost equal intensity. Additionally the region 5 to 10 eV beyond the white line shows less structure compared to cysteine. Methionine sulfoxide (Fig. 5.1C dashed line), the oxidized form of methionine (IPE 2473.1 eV, see Fig. 5.1C solid line), shows a shift in inflection point energy of more than 2 eV (IPE: 2475.9 eV), whereas the shape of the edge stays about the same. The second derivatives of the spectra shown in Fig. 5.1B and D accentuate the changes in spectral position and shape. The significant changes seen in the second derivatives demonstrate the sensitivity of the XAS method for distinguishing between the different kinds of S-containing molecules.

The S XANES spectrum of glutathione in its reduced (Figure 5.2A) and oxidized form are shown in Fig. 5.2C. Plotting these spectra over the corresponding cysteine and cystine spectra reveals major similarities, as expected. This is also reflected in similar inflection point energies for GSH and cysteine, and for GSSG and cystine and also in the similarity of the second derivatives of the spectra (Fig. 5.2B and D) at energies near the IPE. Differences become obvious more than 10 eV beyond the IPE, where more distant atoms and multiple scattering effects begin to contribute to the spectral features. The

Table 5.1 Sulfur K-edge inflection point energies.

Compound	Edge inflection point energy * [eV]
cysteine (Cys-SH)	2473.1
cystine (Cys-S–S-Cys)	2472.1
methionine	2473.1
methionine sulfoxide	2475.9
glutathione reduced (GSH)	2473.0
glutathione oxidized (GSSG)	2472.2
blood	2472.4
erythrocytes	2473.0
plasma	2472.3

* The precision of the inflection point energy is ±0.1 eV; the inflection point reported is determined from the zero-crossing of the second derivative of the spectrum.

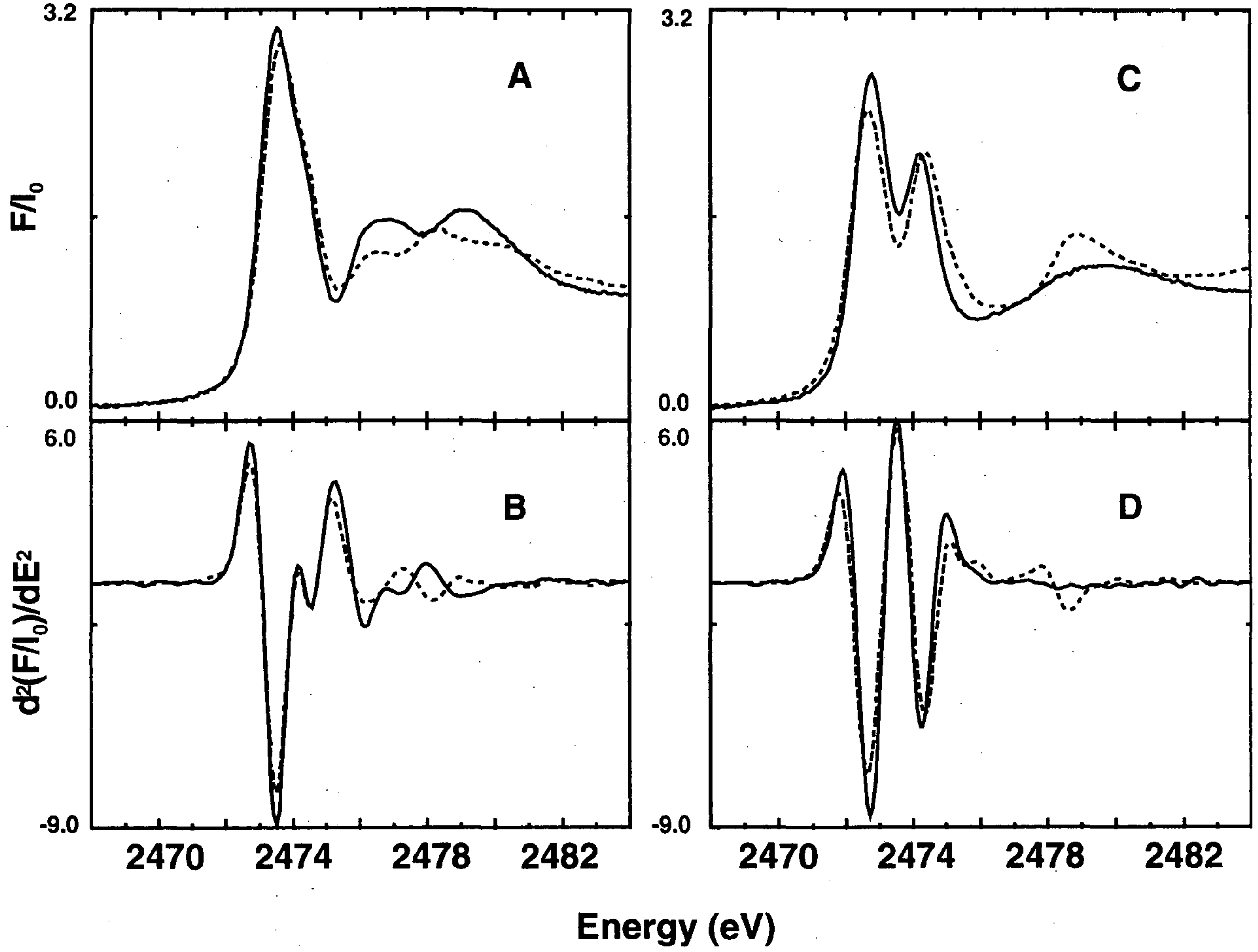
3.2
0.0
F/I$_0$
A
C
6.0
-9.0
d^2(F/I$_0$)/dE^2
B
D
2470
2474
2478
2482
Energy (eV)

Figure 5.2 Sulfur XANES from glutatathione and amino acids.

(**A**) Normalized S K-edge X-ray absorption spectra of reduced glutathione (—) and cysteine (---).

(**B**) second derivatives of reduced glutathione (—) and cysteine (---).

(**C**) Normalized S K-edge X-ray absorption spectra of oxidized glutathione (—) and cystine (---).

(**D**) second derivatives of oxidized glutathione (—) and cystine (---).

All sample materials were in the form of solids.

sulfur K-edge spectra of whole blood, plasma and erythrocytes were collected to determine the ratio of thiol- to disulfide-sulfur in these biological samples.

Erythrocytes

Figure 5.3 shows the sulfur K-edge XANES spectrum from erythrocytes (solid line). Comparison with the reduced glutathione spectrum (dashed line) shows near identity in the rising edge region and indicates that glutathione is present predominantly in its reduced form. The post-edge region shows some difference, again because the scattering of more distant atoms and multiple scattering effects begin to contribute. It is appropriate to simulate the erythrocyte spectrum only with glutathione and without any non-glutathione derived cysteine contributions since it is known that the level of cysteine and cystine is at least one order of magnitude lower than the glutathione concentration in red blood cells.[242,243] The similarities of the sulfur XAS spectra of reduced glutathione and cysteine do not allow a differentiation between these two moieties. This is not required since the focus of this study is the determination of the ratio of thiol to disulfide sulfur and not the absolute amounts of all individual thiol and/or disulfide-components. There is good agreement between the thiol (GSH) concentrations obtained here by sulfur K-edge spectroscopy and those determined spectrophotometrically and by HPCE analysis.[250] Spectrophotometric investigations of human red blood cells have shown that the level of GSH to GSSG is about 245:1. By HPCE analysis no GSSG was detectable. Another study that analyzed GSH and GSSG levels of normal human red blood cells by HPLC and electrochemical detection reported a ratio of 297:1.[211] The uncertainty of the least squares fitting methodology is ~ 5% and hence the detectability of GSSG in excess GSH using XAS is 5:100.

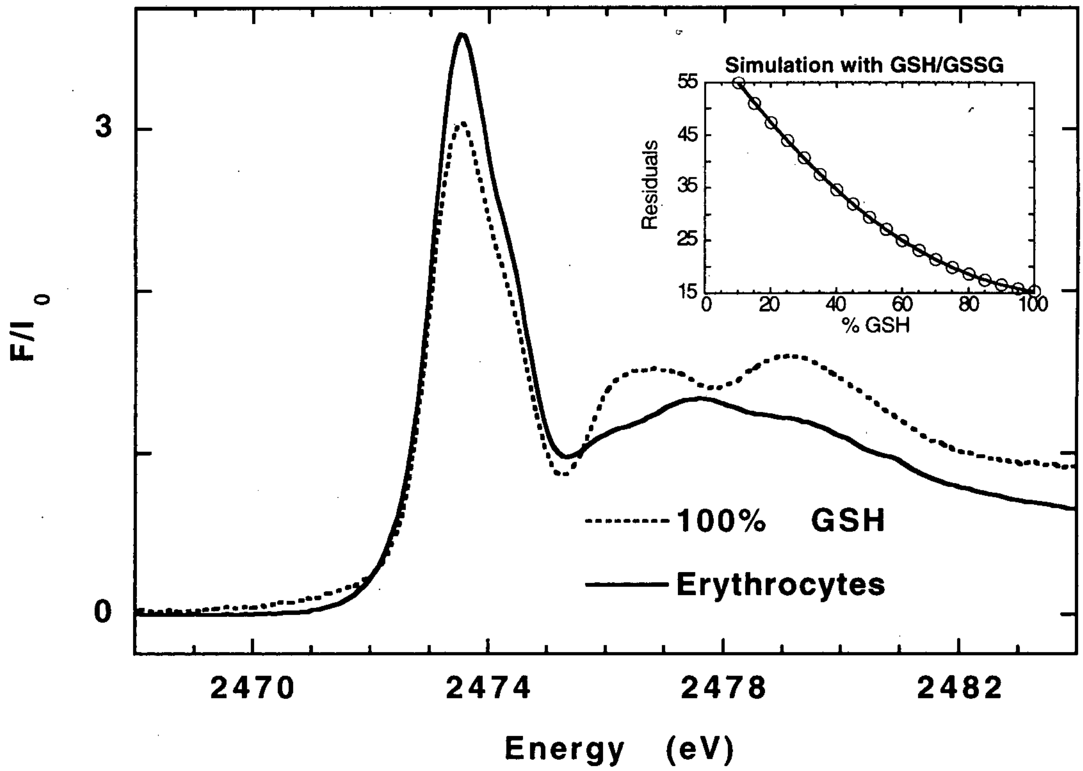

Figure 5.3 Normalized S K-edge X-ray absorption spectra of erythrocytes (solid line) and 100% reduced glutathione (dashed line). Inset shows the plot of residuals (error sum) for the GSH/GSSG simulation in the range 2471 – 2475 eV.

Plasma

The concentration of GSH and GSSG in extracellular media like plasma is orders of magnitude lower than the intracellular content. In plasma the total cyst(e)ine (cysteine and cystine) concentration is ~20 times greater than the total glutathione concentration.[244,245] It has been reported by Malloy *et al.*[251] that in blood plasma up to 50% of cysteine is found to be "mixed" cysteine. The blood plasma spectrum (Figure 5.4, solid line) can be simulated with GSH (or cysteine) and GSSG (or cystine) (Fig. 5.4, dashed line). Best results were obtained by using 68% GSSG and 32% GSH, indicating that 32% are in the thiol form and 68% are disulfides and mixed disulfides. The thiol/disulfide values reported in the literature differ due to the use of different processing methods.[252] A small peak is seen at 2482.5 eV, which corresponds to the K-edge inflection point of S in SO_4^{2-} that is known to be present in plasma.

Whole blood

Sulfur K-edge spectrum of whole blood is shown in Figure 5.5. An excellent simulation of the whole blood spectrum (Fig. 5.5) is obtained by a combination of 54% GSH and 46% GSSG. The inflection point of the whole blood spectrum is satisfactorily simulated, although there are some small differences in amplitudes between the simulation and the spectrum of blood. This might be because of small differences in self absorption of the blood samples, which were frozen glasses compared to GSH and GSSG samples which were solid powders. The shape of the S K-edge spectrum of whole blood is also satisfactorily simulated (Fig. 5.6) by the addition of the spectrum of erythrocytes (25%) with the spectrum from plasma (75%) indicating that the separation protocol does not alter the composition and the redox status of the erythrocytes and plasma.

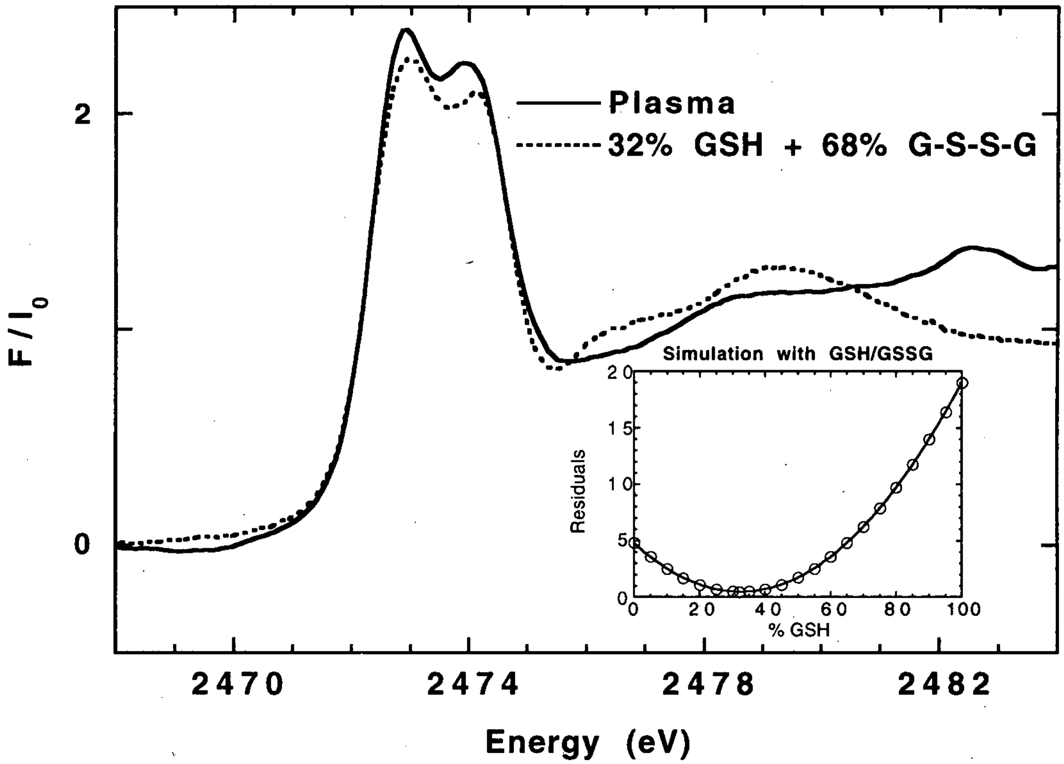

Figure 5.4 Normalized S K-edge X-ray absorption spectra of blood plasma (solid line) and a simulation of 32% GSH and 68% GSSG (dashed line). Inset shows the plot of residuals (error sum) for the GSH/GSSG simulation in the range 2471 – 2475 eV.

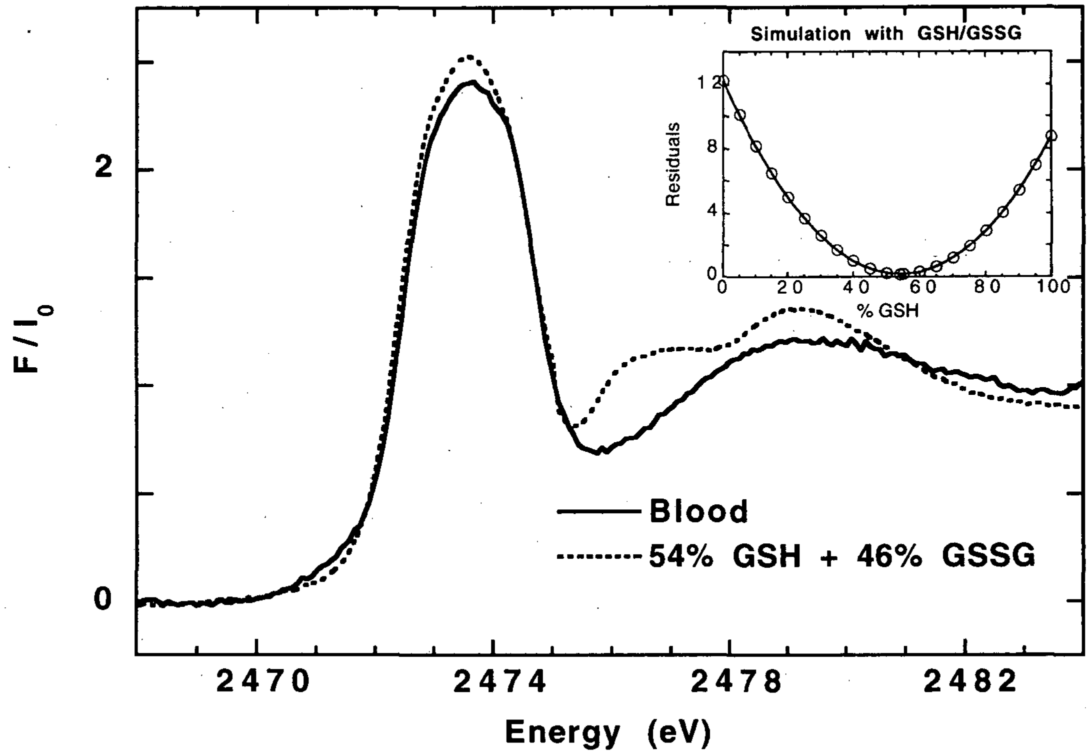

Figure 5.5 Normalized S K-edge X-ray absorption spectra of whole blood (solid line) and a simulation of 54% GSH and 46% GSSG (dashed line). Inset shows the plot of residuals (error sum) for the GSH/GSSG simulation in the range 2471 – 2475 eV.

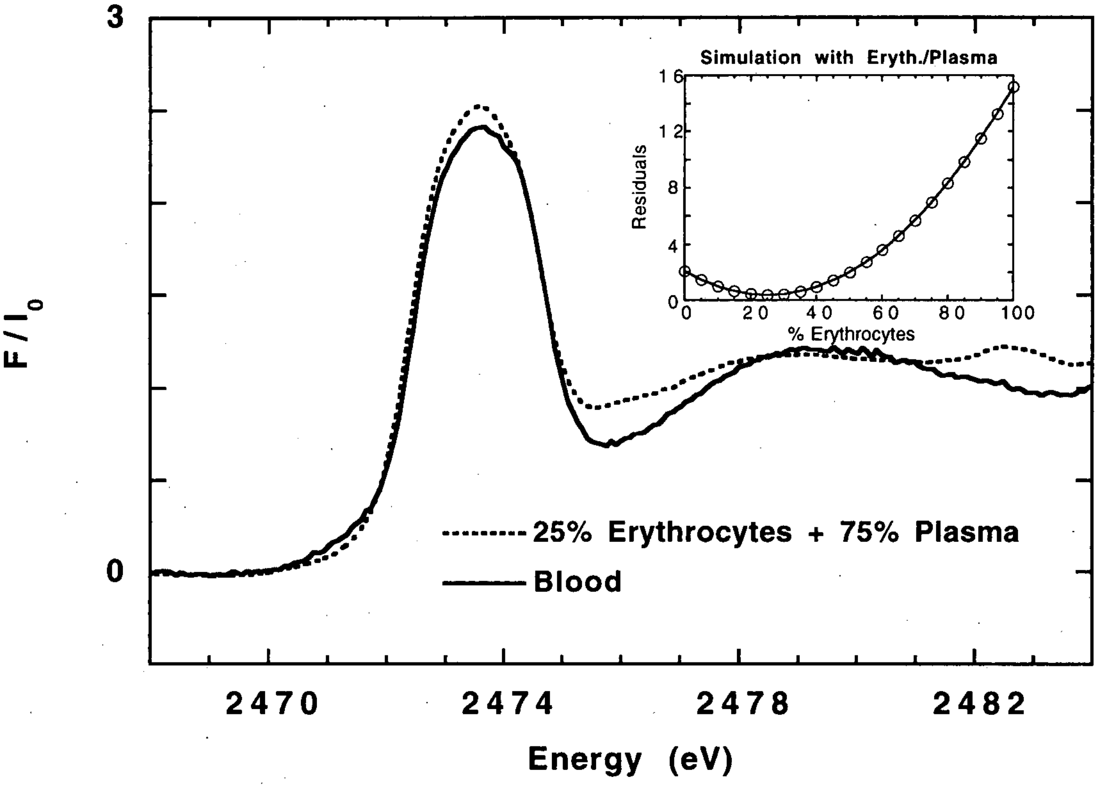

Figure 5.6 Normalized S K-edge X-ray absorption spectra of whole blood (solid line) and a simulation with 25% erythrocytes and 75% plasma (dashed line). Inset shows the plot of residuals (error sum) for the erythrocytes/plasma simulation in the range 2471 – 2475 eV.

Discussion

Conflicting literature values for erythrocyte, plasma and whole blood thiol and disulfide (cysteine, GSH and cystine, GSSG) values have resulted from the use of different analytical methods.[252] Also, a remaining question is whether all thiol and disulfide forms in a blood sample have been quantitatively measured using standard analytical methods. Moreover, the stability of GSH and its possible oxidation to GSSG during the period between collection and analytical determination have been questioned.[253]

To resolve these matters it is desirable to have an analytical tool that measures the thiol to disulfide ratio in biological samples without chemical treatment prior to determination. Sulfur K-edge spectroscopy provides such a tool. We have recorded spectra of whole biological cells, where the sulfur concentration is in the millimolar range. This sulfur concentration in the biological tissues was high enough that the spectra of the samples could be measured without any prior concentration and at the same time did not lead to problems of self absorption. A sulfur K-edge scan takes around 20 min and usually one scan has a signal-to-noise ratio high enough that the IPE can be determined and the shape of the edge analyzed. Sulfur K-edge spectroscopy detects changes of ~5% in the thiol to disulfide ratio. Thus this tool does not have the absolute sensitivity of other analytical methods. Additionally sulfur K-edge spectroscopy does not distinguish between glutathione and cyst(e)ine, nor between GSSG and GSSR. However, we have shown that this method is an excellent tool to determine the thiol redox status in whole cells and to within an accuracy of 5%. The reported numbers vary over a much wider range.

In the future we expect to detect changes in the redox state of other biological tissues using this method and that some of the most interesting and hitherto unavailable information will be obtained by observing the thiol redox status as the cells traverse their structural and metabolic states. Furthermore, with this non-invasive spectroscopic determination of the oxidation states of intracellular thiol groups it becomes possible to measure the changes induced by drugs and to explore the idea that radiation damage to cells may be determined by the state of sulfur.

Chapter 6 — Conclusions and Future Directions

The preceding chapters have shown the successful application of x-ray absorption spectroscopy to three important elements in biology: strontium (in place of calcium), manganese and sulfur. Chapters 2 and 3 have proved the proximity of the calcium cofactor to the manganese cluster of photosynthesis, through the use of Sr EXAFS methods. We had substituted strontium for calcium and thus indirectly probed the binding site of the crucial cofactor in oxygen evolution. A distance of about 3.5 Å was established between Ca and Mn. The use of polarized Sr EXAFS in Chapter 3 obtained angular information about the position of this cofactor, and placed constraints on the possible location of Ca in relation to the Mn cluster. The refined working model of the OEC active site is displayed in Figure 3.9.

Other refinements to the OEC model were made by excluding certain structures as possible topologies of the Mn cluster. This was achieved in Chapter 4, where the C_{3v} distorted cubane was shown not to resemble the native catalytic cluster, after comparison between a set of synthesized Mn model complexes, and Photosystem II. Again, x-ray absorption spectroscopy was used to compare and contrast the two systems. Major differences in the XANES and EXAFS from the two cases showed the need for more distortion of the C_{3v} cubane framework to resemble the observed EXAFS spectra of the OEC active site.

Chapter 5 proved that XAS is a useful tool to probe the redox state of sulfur in biological systems. Specifically, we were able to distinguish between the thiol- and disulfide forms present in amino acids and glutathione. Approximate ratios of thiol- to disulfide sulfur were found by comparison of the sulfur XANES of blood with those from known model compounds mentioned earlier. After this work was completed, another similar study endorsed the suitability of sulfur XAS in finding the chemical speciation of S in biological systems.[254] Despite these gains, several related avenues remain for further research and investigation.

The Case of the Missing Sr-altered Multiline Signal

As mentioned in Chapter 2, Sr-substitution (for Ca) induces an altered EPR multiline signal (MLS) in the S_2-state, achieved by continuous illumination at 200 K.[30,38,46] The altered MLS served as a useful diagnostic (along with oxygen activity assays and metals quantitation) to indicate Sr substitution for calcium. However, after the Chelex treatment,[42,72] the Sr-altered MLS reverts to the normal signal, which resembles that of Ca-containing PS II (Figure 6.1). Because the oxygen activity (40%) and metals analysis (showing ~ 0.8 Sr per 4 Mn) still indicate replacement, the lack of this diagnostic signal did not prevent us from proceeding with the Sr EXAFS experiments, and drawing the conclusions reached in Chapter 3.

Nevertheless, concerns have been raised that the absence of the perturbed MLS could indicate the Sr^{2+} did not access the relevant binding site. The cause for the disappearance of the Sr-altered MLS remains unknown. One possible explanation is that the presence of excess Sr (before Chelex treatment) induces a conformational change of the around protein the Mn cluster, affecting the its environment and the magnetic coupling between the Mn atoms. After Chelex treatment, Sr presumably remains in the functional cofactor binding site, but this alone may not be sufficient to perturb the Mn cluster significantly.

A systematic experiment to test this notion is to add back excess Sr^{2+} into Chelex-treated PS II and monitor the S_2-state EPR signal. We can determine whether disappearance of the Sr-altered MLS is reversible, and verify whether the excess Sr^{2+} causes that signal. This test could then show that the altered MLS is not needed for Sr substitution into the functional Ca binding site.

Improved Mosaic Spread Determination

The importance of accurate mosaic spread values merits a reiteration of its inclusion in future work. Our current estimates achieved from relating mosaic spread to Signal II ratio (shown in Figure 6.2, reproduced from an earlier dissertation[126]) can definitely be improved, both by increasing the number of data points at ratios of 3.5 – 4.5, and by extension into the high end (beyond 5.0). The goal is not necessarily to reduce mosaic spread, but instead to deal accurately with all samples, including those with very low mosaic spread and are outside the data range of Fig. 6.2. As mentioned in Chapter 3, a promising new method is to simulate the cyt b_{559} EPR spectrum of oriented PS II using g-anisotropy, hyperfine interactions and relaxation effects. The references cited[134-136] deal with simulating the Y_D^{ox} EPR signal, but the calculations are also applicable to cyt b_{559}. The calculations involves a disorder parameter equivalent to the mosaic spread. One experimental EPR spectrum (for one sample) can be calculated, and its best-fit disorder parameter extracted, without the need to examine many angles for the orientation dependence of the cyt b_{559} signal, was widely done previously.

The disorder parameter can be correlated with Signal II ratios to construct a calibration line similar to Fig. 6.2. Because only one spectrum per sample is technically necessary to extract the disorder, many samples can be simulated, and related to their observed Signal II ratios. The increased number of data points provide for a more rigorous calibration line. Such methods should yield more accurate values for the mosaic spread, which are applicable not only to the polarized Sr EXAFS studies in Chapter 3, but also to the ongoing polarized Mn EXAFS studies on oriented PS II poised in the S_3 state.[148]

Improvements to Sulfur XAS

To achieve better simulations of sulfur in biological systems (Chapter 5), we will acquire the reference sulfur XANES spectra from solutions of known sulfur compounds (such as cysteine, methionine and glutathione). The spectra from the known sulfur models in Chapter 5 were measured on powdered, solid samples. Solution XANES spectra will more closely approximate the environment of biological sulfur. In the future, these more suitable models can be used to simulate S XANES from other biological systems, to detect the redox state of sulfur as structural or metabolic changes occur.

Ca EXAFS Experiments to Probe the Cofactor Directly

The lower energy of the S K-edge (2.5 keV) presented practical difficulties in obtaining XANES spectra. However, the achievements described in Chapter 5 revealed lessons that enabled us to consider the feasibility of directly probing the cofactor in OEC by calcium EXAFS (Ca K-edge at 4.0 keV). Dealing with the problems encountered in sulfur XANES proved to be valuable preparation for the challenges posed in Ca EXAFS. A detailed program of future experiments on this subject follows.

Background

Based on atomic absorption measurements on PS II membrane fragments, most higher plants have two Ca^{2+} bound to Photosystem II.[32,40-42] One of these Ca^{2+} seems to be tightly associated with the light harvesting complex (LHC II),[44,255] while another, loosely bound calcium is important for functional oxygen evolution.[39] In contrast, PS II particles from the thermophilic cyanobacterium *Synechoccocus* sp., which do not contain LHC II, contain one Ca^{2+} per reaction center (RC).[72] To remove non-specifically bound Ca from these samples before atomic absorption analyses, mild chelators such as Chelex 100 resin have been used effectively.[256] Methods to remove the functional Ca involve a short, low pH incubation with citrate[32] or high NaCl concentrations with chelators and light.[40,257] Both methods inactivate oxygen evolution, which can be restored by the addition of Ca^{2+}. This effect is rather specific for Ca because the only other metal cation capable of partially restoring function is Sr^{2+}.[30] It is this functional Ca that will be targeted by EXAFS studies to determine its proximity to the Mn cluster and its role in water oxidation.

Proposed Experiments

To probe the functional Ca binding site, we will perform Ca K-edge EXAFS studies on PS II samples having ≤ 2 Ca associated per reaction center. The technique of Ca EXAFS is element-specific and would directly probe the environment of the cofactor binding site in fully functional, native systems, requiring no harsh treatments or divalent cation depletion or substitution. Another benefit from Ca EXAFS is the larger *k*-range obtainable compared to Mn EXAFS (limited by the Fe K-edge at 7.1 keV, from Fe in PS II), allowing for better resolution of multiple components.

X-ray absorption studies on biological Ca samples have been reported,[258] including applications to milk Ca phosphate,[259] the Ca-binding protein troponin[260] and even preliminary (but inconclusive) work on Photosystem II samples.[261] It does, however, involve experimental difficulties not associated with conventional Mn EXAFS. Chief among these is the problem of obtaining an adequate signal-to-noise ratio, for the following reasons: 1) for spinach PS II, there are 2 Ca/RC, of which only one is functional for oxygen evolution; 2) the x-ray fluorescence yield of Ca is lower than that of Mn; and 3) the flux of synchrotron radiation at the Ca K-edge energy (4.0 keV) is lower than at the Mn K-edge (6.5 keV), due to attenuation by air and window materials. For biochemical sample preparation, the main problem is adventitious Ca contamination. Extreme care must be taken to remove such Ca from glassware, solutions and PS II samples, because the nonspecifically bound Ca would also contribute to the EXAFS, diluting the signals coming from those associated with the OEC. While these drawbacks are real, they can be addressed by taking certain precautions: 1) maximizing flux by minimizing the air path to the sample, 2) working on a high-intensity wiggler beamline, such as the Beamline VI-2, and 3) removing Ca contamination with Chelex 100 chelator. These steps will allow us to focus on only the Ca present in PS II, and show unambiguously and directly that Mn is present 3.5 Å from it (as indirectly shown from Mn and Sr EXAFS[46,119]).

Spinach PS II Membranes. The biological system most readily available for Ca EXAFS is PS II from spinach.[66] While it contains two Ca per reaction center (RC), the most studied system for Ca^{2+} effects on oxygen evolution is spinach-derived PS II, making it a logical candidate for examination by Ca EXAFS. Given sufficient signal-to-noise ratio for the EXAFS spectra, we should be able to focus on the functional Ca necessary for activity.

Cyanobacterial PS II preparations. The ideal PS II sample for Ca K-edge experiments is that from *Synechoccocus* sp.,[146,262] because it contains only one Ca per PS II reaction center, and remains active without Ca in the assay buffer. These systems have been used in Mn K-edge XAS studies in our research group before[146] and so would be suitable for complementary Ca XAS experiments. Facilities for growing these cyanobacteria and isolating PS II particles are available in our group. As mentioned before, adventitious Ca will be removed from the spinach and cyanobacterial PS II samples by washing with Chelex 100 chelator resin. The success of this procedure will be checked by atomic absorption measurements of Ca and Mn content relative to PS II, by oxygen evolution rates before and after treatment, and by the presence of normal S_2 state EPR multiline signal after 200 K illumination. Ca XAS measurements will be taken on dark-adapted (S_1) samples that satisfy the above assays and PS II samples will be checked by EPR again for possible radiation damage.

PS II Samples poised in Intermediate S-States. Providing these preliminary experiments on dark-adapted (S_1) samples are successful, the Ca EXAFS can be extended to spinach and cyanobacterial PS II samples poised in the S_0, S_2 or S_3 states by flash illumination.[19] By monitoring any changes in the structure of the calcium site as the complex cycles through the various intermediate S-states, we will reveal the actual role of Ca in water oxidation (such as controlling substrate water binding to the catalytic site, as speculated[27]). Ca-depletion blocks any advance beyond the S_3-state, which is detectable by the appearance of a "split" EPR signal around g=2. Our studies could show how Ca allows the Mn cluster to proceed through S_3, cycle and evolve oxygen, and thus contribute to developing a working mechanism of this important reaction.

Ca-depleted PS II Membranes. The proper control for spinach PS II samples that have only two Ca per RC is the inactive, Ca-depleted PS II, which presumably has only one Ca remaining in the tightly bound site (near LHC II) that is not necessary for oxygen evolution and requires harsher treatments to remove. Given sufficiently high signal-to-noise ratio, subtracting the Ca-depleted (1 Ca/PS II) EXAFS data from the corresponding 2 Ca/PS II data would yield the net spectrum for only the functional Ca cofactor essential for oxygen evolution.

Compared to the Sr EXAFS approach described in Chapters 2 and 3, the planned Ca EXAFS experiments would not be superfluous, but instead are complementary to this current approach. While practical difficulties exist as outlined above, the proposed method will be simpler, more direct and most closely resemble the native systems, because it will bypass the Ca depletion and Sr substitution steps and risks associated with them. Obtaining corroborating structural data from Sr and Ca EXAFS should provide a more convincing resolution to the issue of whether the cofactor binds close enough to the catalytic cluster to affect water oxidation directly. In conclusion, x-ray absorption spectroscopy on Sr, Ca, Mn and S demonstrates the versatility of synchrotron radiation as an element-specific probe of metalloproteins, especially for metals with limited spectroscopic handles.

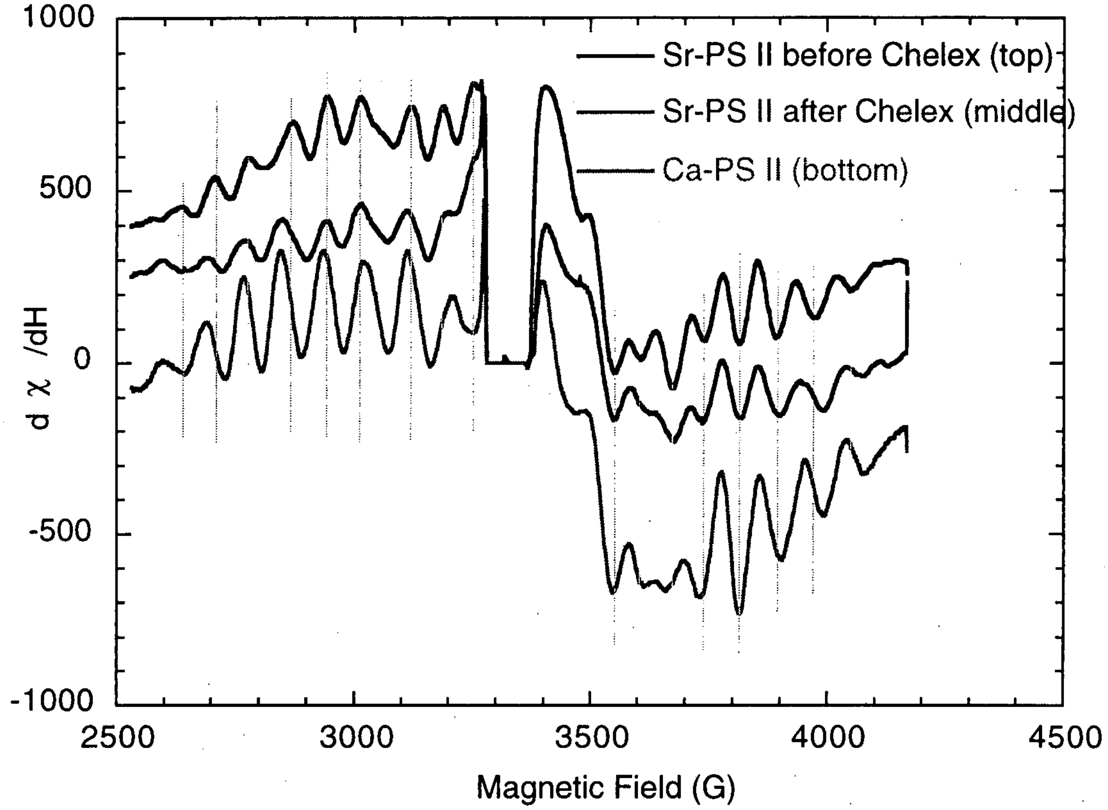

Figure 6.1 EPR Multiline signal (MLS) for Sr-reactivated PS II before and after Chelex treatment. Addition of Sr to Ca-depleted PS II includes an altered multiline, compared to the normal MLS in Ca-containing PS II. Differences in spacing and the pattern of lines are apparent between the Sr- (top trace) and Ca- (bottom trace) PS II samples (see guide lines). After removal of excess Sr, though, the signal reverts to a form similar to the normal MLS (observe how most lines coincide between middle and bottom curves). The only exception is the ~ 3673 G region where the two Sr-PS II samples remain different from Ca-PS II. This reversion to normal multiline is always observed after Chelex treatment. Metals quantitation did not indicate complete removal of Sr, and oxygen activity (40%) was virtually identical to that before Chelex treatment. Therefore, these samples (with reverted, not altered MLS) were used for Sr EXAFS studies. Sample preparation and EPR spectrometer settings were as noted in Figure 2.1 and Chapter 2.

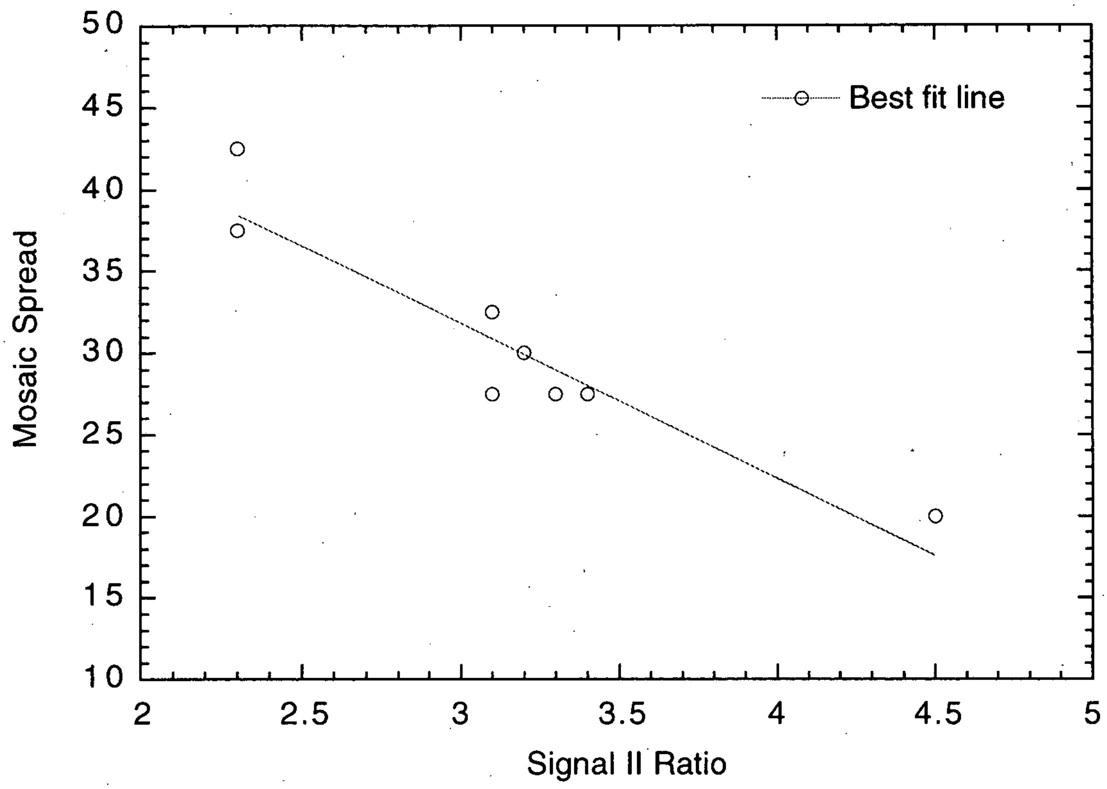

Figure 6.2 Calibration line relating mosaic spread to EPR Signal II ratio. Estimates for mosaic spread of the oriented PS II samples in Chapter 3 were derived from this line, reproduced using data from an earlier dissertation.[126] The least-squares fit yields a slope of -9.478 and y-intercept 60.235.

References

1. Hughes, M. N. *The Inorganic Chemistry of Biological Processes;* 2nd ed.; John Wiley & Sons: London, 1981.
2. Butler, I. S.; Harrod, J. F. *Inorganic Chemistry;* Benamin/Cummings Publishing: Redwood City, 1989.
3. Debus, R. J. *Biochim. Biophys. Acta* **1992**, *1102*, 269-352.
4. Livorness, J.; Smith, T. D. *Struct. Bond.* **1982**, *48*, 1-44.
5. *Iron-Sulfur Proteins;* Spiro, T. G., Ed. John Wiley & Sons, Inc.: New York, 1982 Vol. 4 in series.
6. Scott, R. A. *Methods Enzymol.* **1985**, *117*, 414-459.
7. Cramer, S. P. In *X-ray Absorption: Principles, Applications and Techniques of EXAFS, SEXAFS, and XANES;* Koningsberger, D. C. and Prins, R., Eds.; Wiley-Interscience: New York, 1988; pp 257-320.
8. Bertagnolli, H.; Ertel, T. S. *Angew. Chem. Int. Ed. Engl.* **1994**, *33*, 45-66.
9. Yocum, C. F. *Biochim. Biophys. Acta* **1991**, *1059*, 1-15.
10. Homann, P. H. *Biochim. Biophys. Acta* **1988**, *934*, 1-13.
11. Yachandra, V. K.; Sauer, K.; Klein, M. P. *Chem. Rev.* **1996**, *96*, 2927-2950.
12. Britt, R. D. In *Oxygenic Photosynthesis: The Light Reactions;* Ort, D. R. and Yocum, C. F., Eds.; Kluwer Academic Publishers: Dordrecht, 1996; pp 137-164.
13. Renger, G. *Physiol. Plant.* **1997**, *100*, 828-841.
14. Kok, B.; Forbush, B.; McGloin, M. *Photochem. Photobiol.* **1970**, *11*, 457-476.
15. Joliot, P.; Kok, B. In *Bioenergetics of Photosynthesis;* Govindjee, Ed. Academic Press: New York, NY, 1975; pp 387-412.

16. Yachandra, V. K.; DeRose, V. J.; Latimer, M. J.; Mukerji, I.; Sauer, K.; Klein, M. P. *Jpn. J. Appl. Phys.* **1993**, *32*, 523-526.

17. Wieghardt, K. *Angew. Chem. Int. Ed. Engl.* **1994**, *33*, 725-728.

18. Sauer, K.; Yachandra, V. K.; Britt, R. D.; Klein, M. P. In *Manganese Redox Enzymes*; Pecoraro, V. L., Ed. VCH Publishers: New York, 1992; pp 141-175.

19. Roelofs, T. A.; Liang, W.; Latimer, M. J.; Cinco, R. M.; Rompel, A.; Andrews, J. C.; Sauer, K.; Yachandra, V. K.; Klein, M. P. *Proc. Natl. Acad. Sci. USA* **1996**, *93*, 3335-3340.

20. Ono, T.-A.; Noguchi, T.; Inoue, Y.; Kusunoki, M.; Matsushita, T.; Oyanagi, H. *Science* **1992**, *258*, 1335-1337.

21. Dau, H.; Andrews, J. C.; Roelofs, T. A.; Latimer, M. J.; Liang, W.; Yachandra, V. K.; Sauer, K.; Klein, M. P. *Biochemistry* **1995**, *34*, 5274-5287.

22. Mukerji, I.; Andrews, J. C.; DeRose, V. J.; Latimer, M. J.; Yachandra, V. K.; Sauer, K.; Klein, M. P. *Biochemistry* **1994**, *33*, 9712-9721.

23. Riggs, P. J.; Mei, R.; Yocum, C. F.; Penner-Hahn, J. E. *J. Am. Chem. Soc.* **1992**, *114*, 10650-10651.

24. George, G. N.; Prince, R. C.; Cramer, S. P. *Science* **1989**, *243*, 789-791.

25. DeRose, V. J.; Mukerji, I.; Latimer, M. J.; Yachandra, V. K.; Sauer, K.; Klein, M. P. *J. Am. Chem. Soc.* **1994**, *116*, 5239-5249.

26. MacLachlan, D. J.; Nugent, J. H. A.; Bratt, P. J.; Evans, M. C. W. *Biochim. Biophys. Acta* **1994**, *1186*, 186-200.

27. Boussac, A.; Rutherford, A. W. *Biochem. Soc. Trans.* **1994**, *22*, 352-358.

28. Boussac, A.; Rutherford, A. W. *Photosynth. Res.* **1992**, *32*, 207-209.

29. Ghanotakis, D. F.; Babcock, G. T.; Yocum, C. F. *FEBS Lett.* **1984**, *167*, 127-130.

30. Boussac, A.; Rutherford, A. W. *Biochemistry* **1988**, *27*, 3476-3483.
31. Lockett, C. J.; Demetriou, C.; Bowden, S. J.; Nugent, J. H. A. *Biochim. Biophys. Acta* **1990**, *1016*, 213-218.
32. Ono, T.-A.; Inoue, Y. *FEBS Lett.* **1988**, *227*, 147-152.
33. Ghanotakis, D. F.; Babcock, G. T.; Yocum, C. F. *Biochim. Biophys. Acta* **1985**, *809*, 173-180.
34. Ono, T.-A.; Inoue, Y. *Arch. Biochem. Biophys.* **1989**, *275*, 440-448.
35. Boussac, A.; Rutherford, A. W. *Chem. Script.* **1988**, *28A*, 123-126.
36. Boussac, A.; Zimmermann, J.-L.; Rutherford, A. W. *Biochemistry* **1989**, *28*, 8984-8989.
37. Sivaraja, M.; Tso, J.; Dismukes, G. C. *Biochemistry* **1989**, *28*, 9459-9464.
38. Tso, J.; Sivaraja, M.; Dismukes, G. C. *Biochemistry* **1991**, *30*, 4734-4739.
39. Ädelroth, P.; Lindberg, K.; Andréasson, L.-E. *Biochemistry* **1995**, *34*, 9021-9027.
40. Cammarata, K. V.; Cheniae, G. M. *Plant Physiol.* **1987**, *84*, 587-595.
41. Shen, J.-R.; Satoh, K.; Katoh, S. *Biochim. Biophys. Acta* **1988**, *933*, 358-364.
42. Katoh, S.; Satoh, K.; Ohno, T.; Chen, J.-R.; Kashino, Y. In *Progress in Photosynthesis Research*; Biggins, J., Ed. Martinus Nijhoff Publishers: Dordrecht, 1987; Vol. I.; pp I.5.625-628.
43. Davis, D. J.; Gross, E. L. *Biochim. Biophys. Acta* **1975**, *387*, 557-567.
44. Han, K.-C.; Katoh, S. *Plant Cell Physiol.* **1993**, *34*, 585-593.
45. Chen, C.; Kazimir, J.; Cheniae, G. M. *Biochemistry* **1995**, *34*, 13511-13526.
46. Latimer, M. J.; DeRose, V. J.; Mukerji, I.; Yachandra, V. K.; Sauer, K.; Klein, M. P. *Biochemistry* **1995**, *34*, 10898-10909.

47. Noguchi, T.; Ono, T.-A.; Inoue, Y. In *Photosynthesis: from Light to Biosphere*; Mathis, P., Ed. Kluwer Academic Publishers: Dordrecht, The Netherlands, 1995; Vol. II; pp 235-240.

48. Noguchi, T.; Ono, T.-A.; Inoue, Y. *Biochim. Biophys. Acta* **1995**, *1228*, 189-200.

49. MacLachlan, D. J.; Hallahan, B. J.; Ruffle, S. V.; Nugent, J. H. A.; Evans, M. C. W.; Strange, R. W.; Hasnain, S. S. *Biochem. J.* **1992**, *285*, 569-576.

50. Seidler, A. *Biochim. Biophys. Acta* **1996**, *1277*, 35-60.

51. Riggs-Gelasco, P. J.; Mei, R.; Ghanotakis, D. F.; Yocum, C. F.; Penner-Hahn, J. E. *J. Am. Chem. Soc.* **1996**, *118*, 2400-2410.

52. Hatch, C.; Grush, M.; Bradley, R.; LoBrutto, R.; Cramer, S.; Frasch, W. In *Photosynthesis: from Light to Biosphere*; Mathis, P., Ed. Kluwer Academic Publishers: Dordrecht, The Netherlands, 1995; Vol. II; pp 425-429.

53. Booth, P. J.; Rutherford, A. W.; Boussac, A. *Biochim. Biophys. Acta* **1996**, *1277*, 127-134.

54. Fischer, M.; Bonello, B.; Itie, J. P.; Polian, A.; Dartyge, E.; Fontaine, A.; Tolentino, H. *Phys. Rev. B* **1990**, *42*, 8494-8498.

55. Kohn, S. C.; Charnock, J. M.; Henderson, C. M. B.; Greaves, G. N. *Contrib. Mineral. Petrol.* **1990**, *105*, 359-368.

56. Papelis, C.; Chen, C.-C.; Hayes, K. F. In *SSRL 1995 Activity Report*; Cantwell, K. and Dunn, L., Eds.; Stanford Synchrotron Radiation Laboratory: Stanford, 1996; pp 206-209.

57. Hayes, K. F.; Traina, S. J.; Papelis, C.; Katz, L. E. In *SSRL 1996 Activity Report*; Dunn, L., Ed. Stanford Synchrotron Radiation Laboratory: Stanford, 1997; pp A-322-329.

58. Greegor, R. B.; Pingitore, N. E., Jr.; Lytle, F. W. *Science* **1997,** *275,* 1452-1454.

59. Yachandra, V. K. *Methods Enzymol.* **1995,** *246,* 638-675.

60. Jaklevic, J.; Kirby, J. A.; Klein, M. P.; Robertson, A. S.; Brown, G.; Eisenberger, P. *Solid State Commun.* **1977,** *23,* 679-682.

61. Yachandra, V. K.; Klein, M. P. In *Biophysical Techniques in Photosynthesis;* Amesz, J. and Hoff, A. J., Eds.; Kluwer Academic Publishers: Dordrecht, Netherlands, 1996; Vol. 3; pp 337-354.

62. Riggs-Gelasco, P. J.; Stemmler, T. L.; Penner-Hahn, J. E. *Coord. Chem. Rev.* **1995,** *144,* 245-286.

63. Tamura, N.; Cheniae, G. *Biochim. Biophys. Acta* **1985,** *809,* 245-259.

64. Miller, A.-F.; Brudvig, G. W. *Biochemistry* **1989,** *28,* 8181-8190.

65. Miyao, M.; Inoue, Y. *Biochim. Biophys. Acta* **1991,** *1056,* 47-56.

66. Berthold, D. A.; Babcock, G. T.; Yocum, C. F. *FEBS Lett.* **1981,** *134,* 231-234.

67. Dunahay, T. G.; Staehelin, L. A.; Seibert, M.; Ogilvie, P. D.; Berg, S. P. *Biochim. Biophys. Acta* **1984,** *764,* 179-193.

68. Ono, T.-A.; Izawa, S.; Inoue, Y. *Biochemistry* **1992,** *31,* 7648-7655.

69. Kodera, Y.; Hara, H.; Astashkin, A. V.; Kawamori, A.; Ono, T.-A. *Biochim. Biophys. Acta* **1995,** *1232,* 43-51.

70. Shen, J.-R.; Katoh, S. *Plant Cell Physiol.* **1991,** *32,* 439-446.

71. Zimmermann, J.-L.; Rutherford, A. W. *Biochemistry* **1986,** *25,* 4609-4615.

72. Kashino, Y.; Satoh, K.; Katoh, S. *FEBS Lett.* **1986,** *205,* 150-154.

73. Arnon, D. I. *Plant Physiol.* **1949,** *24,* 1-15.

74. Porra, R. J.; Thompson, W. A.; Kriedemann, P. E. *Biochim. Biophys. Acta* **1989,** *975,* 384-394.

75. Boussac, A.; Zimmermann, J.-L.; Rutherford, A. W. *FEBS Lett.* **1990**, *227*, 69-74.

76. Astashkin, A. V.; Mino, H.; Kawamori, A.; Ono, T.-A. *Chem. Phys. Lett.* **1997**, *272*, 506-516.

77. Grove, G. N.; Brudvig, G. W. *Biochemistry* **1998**, *37*, 1532-1539.

78. Teo, B. K. *EXAFS: Basic Principles and Data Analysis*; Springer-Verlag: Berlin, 1986.

79. *Center for X-Ray Optics X-Ray Data Booklet*; Vaughan, D., Ed. Lawrence Berkeley Laboratory: Berkeley, 1986; Vol. PUB-490 Rev.

80. O'Day, P. A.; Rehr, J. J.; Zabinsky, S. I.; Brown, G. E., Jr. *J. Am. Chem. Soc.* **1994**, *116*, 2938-2949.

81. Lin, S.-L.; Stern, E. A.; Kalb (Gilboa), A. J.; Zhang, Y. *Biochemistry* **1991**, *30*, 2323-2332.

82. Rehr, J. J.; Mustre de Leon, J.; Zabinsky, S. I.; Albers, R. C. *J. Am. Chem. Soc.* **1991**, *113*, 5135-5140.

83. Rehr, J. J.; Albers, R. C.; Zabinsky, S. I. *Phys. Rev. Lett.* **1992**, *69*, 3397-3400.

84. Schmidbaur, H.; Bach, I.; Wilkinson, D. L.; Müller, G. *Chem. Ber.* **1989**, *122*, 1433-1438.

85. Schmidbaur, H.; Mikulcik, P.; Müller, G. *Chem. Ber.* **1990**, *123*, 1599-1602.

86. Binsted, N.; Strange, R. W.; Hasnain, S. S. *Biochemistry* **1992**, *31*, 12117-12125.

87. Ono, T.-A.; Inoue, Y. *Biochim. Biophys. Acta* **1989**, *973*, 443-449.

88. Miller, A.-F.; Brudvig, G. W. *Biochemistry* **1990**, *29*, 1385-1392.

89. Ananyev, G. M.; Dismukes, G. C. *Biochemistry* **1996**, *35*, 4102-4109.

90. Ohno, T.; Satoh, K.; Katoh, S. *Biochim. Biophys. Acta* **1986**, *852*, 1-8.

91. Shen, J.-R.; Inoue, Y. *Plant Cell Physiol.* **1991,** *32*, 453-457.

92. Rees, W. S., Jr. In *Encyclopedia of Inorganic Chemistry*; King, R. B., Ed. John Wiley & Sons: Chichester, 1994; Vol. 1; pp 67-87.

93. Dittmer, J.; Dau, H. *Ber. Bunsenges. Phys. Chem.* **1996,** *100*, 1993-1998.

94. Riggs-Gelasco, P. J.; Mei, R.; Yocum, C. F.; Penner-Hahn, J. E. *J. Am. Chem. Soc.* **1996,** *118*, 2387-2399.

95. Kretsinger, R. H.; Nelson, D. J. *Coord. Chem. Rev.* **1976,** *18*, 29-124.

96. Bahl, A. M.; Krishnaswamy, S.; Massand, N. G.; Burkey, D. J.; Hanusa, T. P. *Inorg. Chem.* **1997,** *36*, 5413-5415.

97. Pecoraro, V. L. In *Manganese Redox Enzymes*; Pecoraro, V. L., Ed. VCH Publishers: New York, 1992; pp 197-231.

98. Reynolds, R. A., III; Coucouvanis, D. *J. Am. Chem. Soc.* **1998,** *120*, 209-210.

99. Bonadies, J. A.; Kirk, M. L.; Lah, M. S.; Kessissoglou, D. P.; Hatfield, W. E.; Pecoraro, V. L. *Inorg. Chem.* **1989,** *28*, 2037-2044.

100. Mair, F. S.; Snaith, R. In *Encyclopedia of Inorganic Chemistry*; King, R. B., Ed. John Wiley & Sons: Chichester, 1994; Vol. 1; pp 35-54.

101. George, G. N.; Cramer, S. P.; Frey, T. G.; Prince, R. C. *Biochim. Biophys. Acta* **1993,** *1142*, 240-252.

102. George, G. N.; Prince, R. C.; Frey, T. G.; Cramer, S. P. *Physica B* **1989,** *158*, 81-83.

103. Ananyev, G. M.; Dismukes, G. C. *Biochemistry* **1997,** *36*, 11342-11350.

104. Babcock, G. T.; Espe, M.; Hoganson, C. W.; Lydakis-Simantiris, N.; McCracken, J.; Shi, W.; Styring, S.; Tommos, C.; Warncke, K. *Acta Chem. Scand.* **1997,** *51*, 533-540.

105. Hoganson, C. W.; Babcock, G. T. *Science* **1997,** *277*, 1953-1956.

106. Tommos, C.; Babcock, G. T. *Acc. Chem. Res.* **1998,** *31*, 18-25.

107. Yachandra, V. K.; DeRose, V. J.; Latimer, M. J.; Mukerji, I.; Sauer, K.; Klein, M. P. *Science* **1993**, *260*, 675-679.

108. Penner-Hahn, J. E. *Struct. Bond.* **1998**, *90*, 1-36.

109. Yocum, C. F.; Pecoraro, V. L. *Curr. Opin. Chem. Biol.* **1999**, *3*, 182-187.

110. Rhee, K.-H.; Morris, E. P.; Barber, J.; Kuehlbrandt, W. *Nature* **1998**, *396*, 283-286.

111. Hankamer, B.; Morris, E. P.; Barber, J. *Nature Struct. Biol.* **1999**, *6*, 560-564.

112. Miller, A.-F.; Brudvig, G. W. *Biochim. Biophys. Acta* **1991**, *1056*, 1-18.

113. Dismukes, G. C.; Siderer, Y. *Proc. Natl. Acad. Sci. USA* **1981**, *78*, 274-278.

114. Messinger, J.; Nugent, J. H. A.; Evans, M. C. W. *Biochemistry* **1997**, *36*, 11055-11060.

115. Iuzzolino, L.; Dittmer, J.; Dörner, W.; Meyer-Klaucke, W.; Dau, H. *Biochemistry* **1998**, *37*, 17112-17119.

116. Boussac, A.; Maison-Peteri, B.; Vernotte, C.; Etienne, A.-L. *Biochim. Biophys. Acta* **1985**, *808*, 225-230.

117. Boussac, A.; Maison-Peteri, B.; Etienne, A.-L.; Vernotte, C. *Biochim. Biophys. Acta* **1985**, *808*, 231-234.

118. Noguchi, T.; Ono, T.-A.; Inoue, Y. *Biochim. Biophys. Acta* **1995**, *1232*, 59-66.

119. Cinco, R. M.; Robblee, J. H.; Rompel, A.; Fernandez, C.; Yachandra, V. K.; Sauer, K.; Klein, M. P. *J. Phys. Chem. B* **1998**, *102*, 8248-8256.

120. Cinco, R. M.; Robblee, J. H.; Rompel, A.; Fernandez, C.; Yachandra, V. K.; Sauer, K.; Klein, M. P. *J. Synchrotron Rad.* **1999**, *6*, 419-420.

121. Dittmer, J.; Dau, H. *J. Phys. Chem. B* **1998**, *102*, 8196-8200.

122. Schiller, H.; Dittmer, J.; Iuzzolino, L.; Dörner, W.; Meyer-Klaucke, W.; Solé, V. A.; Nolting, H.-F.; Dau, H. *Biochemistry* **1998**, *37*, 7340-7350.

123. Blum, H.; Harmon, H. J.; Leigh, J. S.; Salerno, J. C.; Chance, B. *Biochim. Biophys. Acta* **1978**, *502*, 1-10.

124. Blum, H.; Salerno, J. C.; Leigh, J. S., Jr. *J. Mag. Res.* **1978**, *30*, 385-391.

125. Rutherford, A. W. *Biochim. Biophys. Acta* **1985**, *807*, 189-201.

126. Andrews, J. C. Ph. D. Thesis, University of California, Berkeley, 1995.

127. Lakshmi, K. V.; Eaton, S. S.; Eaton, G. R.; Brudvig, G. W. *Biochemistry* **1999**, *38*, 12758-12767.

128. Hasegawa, K.; Kusunoki, M.; Inoue, Y.; Ono, T.-A. *Biochemistry* **1998**, *37*, 9457-9465.

129. Wolfram, S. *The Mathematica Book*; 3rd ed.; Wolfram Media/Cambridge University Press: New York, 1996.

130. Cinco, R. M.; Fernandez, C.; Messinger, J.; Robblee, J. H.; Visser, H.; McFarlane, K. L.; Bergmann, U.; Glatzel, P.; Cramer, S. P.; Sauer, K.; Klein, M. P.; Yachandra, V. K. In *Photosynthesis: Mechanisms and Effects*; Garab, G., Ed. Kluwer Academic Publishers: Dordrecht, 1998; pp 1273-1278.

131. Cinco, R. M.; Rompel, A.; Visser, H.; Aromí, G.; Christou, G.; Sauer, K.; Yachandra, V. K.; Klein, M. P. *Inorg. Chem.* (in press).

132. Hecht, H. G. *Mathematics in chemistry: an introduction to modern methods*; Prentice-Hall: Englewood Cliffs, 1990.

133. WaveMetrics Inc. *Igor Pro User's Guide*; WaveMetrics: Lake Oswego, OR, 1998; Vol. II.

134. Un, S.; Brunel, L.-C.; Brill, T. M.; Zimmermann, J.-L.; Rutherford, A. W. *Proc. Natl. Acad. Sci. USA* **1994**, *91*, 5262-5266.

135. Un, S.; Atta, M.; Fontecave, M.; Rutherford, A. W. *J. Am. Chem. Soc.* **1995**, *117*, 10713-10719.

136. Un, S.; Tang, X.-S.; Diner, B. A. *Biochemistry* **1996**, *35*, 679-684.

137. MacMillan, F.; Hanley, J.; van der Weerd, L.; Knüpling, M.; Un, S.; Rutherford, A. W. *Biochemistry* **1997**, *36*, 9297-9303.

138. Rutherford, A. W.; Zimmermann, J.-L.; Boussac, A. In *The Photosystems: Structure, Function, and Molecular Biology*; Barber, J., Ed. Elsevier B. V.: Amsterdam, 1992; pp 179-229.

139. Renger, G. In *Bioenergetics*; Gräber, P. and Milazzo, G., Eds.; Birkhäuser Verlag: Basel, Switzerland, 1997; pp 310-358.

140. Penner-Hahn, J. E.; Fronko, R. M.; Pecoraro, V. L.; Yocum, C. F.; Betts, S. D.; Bowlby, N. R. *J. Am. Chem. Soc.* **1990**, *112*, 2549-2557.

141. Ono, T.-A.; Kusunoki, M.; Matsushita, T.; Oyanagi, H.; Inoue, Y. *Biochemistry* **1991**, *30*, 6836-6841.

142. Roelofs, T. A.; Liang, W.; Latimer, M. J.; Cinco, R. M.; Rompel, A.; Andrews, J. C.; Yachandra, V. K.; Sauer, K.; Klein, M. P. In *Photosynthesis: From Light to Biosphere*; Mathis, P., Ed. Kluwer: Dordrecht, 1995; Vol. II; pp 459-462.

143. Yocum, C. F. In *Manganese Redox Enzymes*; Pecoraro, V. L., Ed. VCH Publishers: New York, 1992; pp 71-84.

144. Coleman, W. J. *Photosynth. Res.* **1990**, *23*, 1-27.

145. Lindberg, K.; Andréasson, L.-E. *Biochemistry* **1996**, *35*, 14259-14267.

146. McDermott, A. E.; Yachandra, V. K.; Guiles, R. D.; Cole, J. L.; Dexheimer, S. L.; Britt, R. D.; Sauer, K.; Klein, M. P. *Biochemistry* **1988**, *27*, 4021-4031.

147. Yachandra, V. K.; Guiles, R. D.; McDermott, A. E.; Cole, J. L.; Britt, R. D.; Dexheimer, S. L.; Sauer, K.; Klein, M. P. *Biochemistry* **1987**, *26*, 5974-5981.

148. Fernandez, C.; Cinco, R. M.; Robblee, J. H.; Messinger, J.; Pizarro, S. A.; Sauer, K.; Yachandra, V. K.; Klein, M. P. In *Photosynthesis:*

Mechanisms and Effects; Garab, G., Ed. Kluwer Academic Publishers: Dordrecht, 1998; pp 1399-1402.

149. DeRose, V. J.; Latimer, M. J.; Zimmermann, J.-L.; Mukerji, I.; Yachandra, V. K.; Sauer, K.; Klein, M. P. *Chem. Phys.* **1995**, *194*, 443-459.
150. Rüttinger, W.; Dismukes, G. C. *Chem. Rev.* **1997**, *97*, 1-24.
151. Andréasson, L.-E.; Vänngård, T. In *Encyclopedia of Inorganic Chemistry*; King, R. B., Ed. John Wiley & Sons: Chichester, 1994; Vol. 4; pp 2101-2118.
152. Larson, E. J.; Pecoraro, V. L. In *Manganese Redox Enzymes*; Pecoraro, V. L., Ed. VCH Publishers: New York, 1992; pp 1-28.
153. Stemmler, T. L.; Sossong Jr., T. M.; Goldstein, J. I.; Ash, D. E.; Elgren, T. E.; Kurtz Jr., D. M.; Penner-Hahn, J. E. *Biochemistry* **1997**, *36*, 9847-9858.
154. Brudvig, G. W.; Crabtree, R. H. *Proc. Natl. Acad. Sci. USA* **1986**, *83*, 4586-4588.
155. Vincent, J. B.; Christmas, C.; Huffman, J. C.; Christou, G.; Chang, H.-R.; Hendrickson, D. N. *J. Chem. Soc., Chem. Commun.* **1987**, 236-238.
156. Guiles, R. D.; Zimmermann, J.-L.; McDermott, A. E.; Yachandra, V. K.; Cole, J. L.; Dexheimer, S. L.; Britt, R. D.; Wieghardt, K.; Bossek, U.; Sauer, K.; Klein, M. P. *Biochemistry* **1990**, *29*, 471-485.
157. Guiles, R. D.; Yachandra, V. K.; McDermott, A. E.; Cole, J. L.; Dexheimer, S. L.; Britt, R. D.; Sauer, K.; Klein, M. P. *Biochemistry* **1990**, *29*, 486-496.
158. Wang, S.; Tsai, H.-L.; Libby, E.; Folting, K.; Streib, W. E.; Hendrickson, D. N.; Christou, G. *Inorg. Chem.* **1996**, *35*, 7578-7589.
159. Wemple, M. W.; Adams, D. M.; Folting, K.; Hendrickson, D. N.; Christou, G. *J. Am. Chem. Soc.* **1995**, *117*, 7275-7276.

160. Aromí, G.; Wemple, M. W.; Aubin, S. J.; Folting, K.; Hendrickson, D. N.; Christou, G. *J. Am. Chem. Soc.* **1998**, *120*, 5850-5851.

161. Wemple, M. W.; Tsai, H.-L.; Folting, K.; Hendrickson, D. N.; Christou, G. *Inorg. Chem.* **1993**, *32*, 2025-2031.

162. Wemple, M. W.; Adams, D. M.; Hagen, K. S.; Folting, K.; Hendrickson, D. N.; Christou, G. *J. Chem. Soc., Chem. Commun.* **1995**, 1591-1593.

163. Wang, S.; Folting, K.; Streib, W. E.; Schmitt, E. A.; McCusker, J. K.; Hendrickson, D. N.; Christou, G. *Angew. Chem. Int. Ed. Engl.* **1991**, *30*, 305-306.

164. Wang, S.; Tsai, H.-L.; Hagen, K. S.; Hendrickson, D. N.; Christou, G. *J. Am. Chem. Soc.* **1994**, *116*, 8376-8377.

165. Hendrickson, D. N.; Christou, G.; Schmitt, E. A.; Libby, E.; Bashkin, J. S.; Wang, S.; Tsai, H.-L.; Vincent, J. B.; Boyd, P. D. W.; Huffman, J. C.; Folting, K.; Li, Q.; Streib, W. E. *J. Am. Chem. Soc.* **1992**, *114*, 2455-2471.

166. Latimer, M. J.; Rompel, A.; Underwood, J. H.; Yachandra, V. K.; Klein, M. P. *Rev. Sci. Instrum.* **1995**, *66*, 1843-1845.

167. Stern, E. A.; Heald, S. M. *Rev. Sci. Instrum.* **1979**, *50*, 1579.

168. Lytle, F. W.; Greegor, R. B.; Sandstrom, D. R.; Marques, E. C.; Wong, J.; Spiro, C. L.; Huffman, G. P.; Huggins, P. E. *Nucl. Instrum. Meth.* **1984**, *226*, 542-548.

169. Cramer, S. P.; Tench, O.; Yocum, M.; George, G. N. *Nucl. Instrum. Methods Phys. Res.* **1988**, *A266*, 586-591.

170. Zhang, K.; Stern, E. A.; Ellis, F.; Sanders-Loehr, J.; Shiemke, A. K. *Biochemistry* **1988**, *27*, 7470-7479.

171. Bunker, G. A.; Hasnain, S. S.; Sayers, D. E. In *X-ray Absorption Fine Structure*; Hasnain, S. S., Ed. Ellis Horwood: New York, 1991; pp 751-770.

172. Palenik, G. J. *Inorg. Chem.* **1997,** *36*, 4888-4890.

173. Palenik, G. J. *Inorg. Chem.* **1997,** *36*, 3394-3397.

174. Palenik, G. J. *Inorg. Chem.* **1997,** *36*, 122.

175. Liu, W.; Thorp, H. H. *Inorg. Chem.* **1993,** *32*, 4102-4105.

176. Clark-Baldwin, K.; Tierney, D. L.; Govindaswamy, N.; Gruff, E. S.; Kim, C.; Berg, J.; Koch, S. A.; Penner-Hahn, J. E. *J. Am. Chem. Soc.* **1998,** *120*, 8401-8409.

177. DeRose, V. J.; Yachandra, V. K.; McDermott, A. E.; Britt, R. D.; Sauer, K.; Klein, M. P. *Biochemistry* **1991,** *30*, 1335-1134.

178. Rompel, A.; Andrews, J. C.; Cinco, R. M.; Wemple, M. W.; Christou, G.; Pecoraro, V. L.; Sauer, K.; Yachandra, V. K.; Klein, M. P. *J. Am. Chem. Soc.* **1997,** *119*, 4465-4470.

179. Teo, B.-K.; Shulman, R. G. In *Iron-Sulfur Proteins*; Spiro, T. G., Ed. John Wiley & Sons, Inc.: New York, 1982; pp 343-366.

180. Berg, J. M.; Holm, R. H. In *Iron-Sulfur Proteins*; Spiro, T. G., Ed. John Wiley & Sons, Inc.: New York, 1982; pp 1-66.

181. Stout, C. D. In *Iron-Sulfur Proteins*; Spiro, T. G., Ed. John Wiley & Sons, Inc.: New York, 1982; pp 97-146.

182. Hedman, B.; Frank, P.; Penner-Hahn, J. E.; Roe, A. L.; Hodgson, K. O.; Carlson, R. M. K.; Brown, G.; Cerino, J.; Hettel, R.; Troxel, T.; Winick, H.; Yang, J. *Nucl. Instrum. Methods Phys. Res., Sect. A* **1986,** *246*, 797-800.

183. Frank, P.; Hedman, B.; Carlson, R. M. K.; Tyson, T. A.; Roe, A. L.; Hodgson, K. O. *Biochemistry* **1987,** *26*, 4975-4979.

184. Frank, P.; Kustin, K.; Robinson, W. E.; Linebaugh, L.; Hodgson, K. O. *Inorg. Chem.* **1995,** *34*, 5942-5949.

185. Frank, P.; Hedman, B.; Carlson, R. M. K.; Hodgson, K. O. *Inorg. Chem.* **1994**, *33*, 3794-3803.

186. Brot, N.; Weissbach, H. *Arch. Biochem. Biophys.* **1983**, *223*, 271-281.

187. Kosower, E. M.; Kosower, N. S. *Int. Rev. Cytology* **1978**, *54*, 109-160.

188. Usami, M.; Matsushita, H.; Shimayu, T. *J. Biol. Chem.* **1980**, *255*, 1928-1931.

189. Namboodiri, M. A. A.; Weller, J. L.; Klein, D. C. *J. Biol. Chem.* **1980**, *255*, 6032-6035.

190. Ernest, M. J.; Kim, K.-H. *J. Biol. Chem.* **1973**, *248*, 1550-1555.

191. Lau, K.-H. W.; Thomas, J. A. *J. Biol. Chem.* **1983**, *258*, 2321-2326.

192. Wakamatsu, K.; Kominami, E.; Takio, K.; Katunuma, N. *J. Biol. Chem.* **1984**, *259*, 13832-13838.

193. Mukherjee, S. P.; Lynn, W. S. *Biochim. Biophys. Acta* **1979**, *568*, 224-233.

194. Mukherjee, S. P.; Mukherjee, C. *Biochim. Biophys. Acta* **1981**, *677*, 339-349.

195. Tsai, S.-C.; Adamik, R.; Manganiello, V. C.; Vaughan, M. *Biochem. Biophys. Res. Commun.* **1981**, *100*, 637-643.

196. Dotan, I.; Shechter, I. *Biochim. Biophys. Acta* **1982**, *713*, 427-434.

197. Kondo, T.; Taniguchi, N.; Hirano, T.; Kawakami, Y. *J. Biol. Chem.* **1984**, *259*, 15517-11522.

198. Gilbert, H. F. *J. Biol. Chem.* **1982**, *257*, 12086-12091.

199. Beatty, K.; Bieth, J.; Travis, J. *J. Biol. Chem.* **1980**, *255*, 3931-3934.

200. Meister, A. *Pharmacol. Ther.* **1991**, *51*, 1-194.

201. Meister, A. In *Glutathione. Chemical Biochemical and Medical Aspects*; Dolphin, D.; Avramovic, O. and Poulson, R., Eds.; J. Wiley & Sons: New York, 1989; pp 1-48.

202. Sies, H. *Angew. Chem. Int. Ed. Engl.* **1986**, *25*, 1058-1071.

203. Reddy, V. N. *Exp. Eye Res.* **1990**, *50*, 771-778.

204. Ziegler, D. M. *Ann. Rev. Biochem.* **1985**, *54*, 305-329.

205. Hughes, H.; Jaeschke, H.; Mitchell, J. R. *Methods Enzymol.* **1991**, *186*, 681-685.

206. Hissin, P. J.; Hilf, R. *Anal. Biochem.* **1976**, *74*, 214-226.

207. Racker, E. *J. Biol. Chem.* **1951**, *190*, 685-696.

208. Brehe, E.; Burck, H. B. *Anal. Biochem.* **1976**, *74*, 189-197.

209. Akerboom, T. P.; Sies, H. *Methods Enzymol.* **1981**, *77*, 373-382.

210. Anderson, M. E. *Methods Enzymol.* **1985**, *113*, 548-555.

211. Kuninori, T.; Nishiyama, J. *Anal. Biochem.* **1991**, *197*, 19-24.

212. Neuschwander-Tetri, B. A.; Roll, F. J. *Anal. Biochem.* **1989**, *179*, 236-241.

213. Svardal, A. M.; Mansoor, M. A.; Ueland, P. M. *Anal. Biochem.* **1990**, *184*, 338-346.

214. Reed, D. J.; Babson, J. R.; Beatty, P. W.; Brodie, A. E.; Ellis, W. W.; Potter, D. W. *Anal. Biochem.* **1980**, *106*, 55-62.

215. Morier-Teissier, E.; Mestdagh, N.; Bernier, J.-L.; Henichart, J.-P. *J. Liq. Chromatogr.* **1993**, *16*, 573-596.

216. Nischiyama, J.; Kuninori, T. *Anal. Biochem.* **1984**, *138*, 95-98.

217. Richie, J. P., Jr.; Lang, C. A. *Anal. Biochem.* **1987**, *172*, 479-483.

218. Awasthi, S.; Ahmad, F.; Sharma, P.; Ahmad, H. *J. Chromatogr. Biomed. Appl.* **1992**, *584*, 167-173.

219. Crawhall, J. C.; Kalant, D. *Anal. Biochem.* **1988**, *172*, 479-483.

220. Cook, J. A.; Pass, H. I.; Russo, A.; Iype, S.; Mitchell, J. B. *Int. J. Radiat. Oncol. Biol. Phys.* **1989**, *16*, 1321-1324.

221. Rice, G. C.; Bump, E. A.; Shrieve, D. C.; Lee, W.; Kovacs, M. *Cancer Res.* **1986**, *46*, 6105-6110.

222. Ublacker, G. A.; Johnson, J. A.; Siegel, F. L.; Mulcahy, R. T. *Cancer Res.* **1991**, *51*, 1783-1788.

223. Cappiello, M.; Del Corso, A.; Camici, M.; Mura, U. *J. Biochem. Biophys. Methods* **1993**, *26*, 335-341.

224. Pascual, P.; Martinezlara, E.; Barcena, J. A.; Lopez-Barea, J.; Toridio, F. *J. Chromatogr.* **1992**, *581*, 49-56.

225. Beales, D.; Finch, R.; Mc Lean, A. E.; Smith, M.; Wilson, I. D. *J. Chromatogr.* **1981**, *226*, 498-503.

226. Alpert, A. J.; Gilbert, H. F. *Anal. Biochem.* **1985**, *144*, 553-562.

227. Nakamura, H.; Tamura, Z. *Anal. Biochem.* **1981**, *53*, 2190-2193.

228. Keller, D. A.; Menzel, D. B. *Anal. Biochem.* **1985**, *151*, 418-423.

229. Morineau, G.; Azoulay, M.; Frappier, F. *J. Chromatogr.* **1989**, *467*, 209-216.

230. Burton, N. K.; Aherne, G. W. *J. Chromatogr.* **1986**, *382*, 253-257.

231. Velury, S.; Howell, S. B. *J. Chromatogr.* **1988**, *424*, 1416-1146.

232. Stein, A. F.; Dills, R. L.; Klaassen, C. D. *J. Chromatogr.* **1986**, *381*, 259-270.

233. Dupuy, D.; Szabo, S. *J. Liq. Chromatogr.* **1987**, *10*, 107-119.

234. Buchberger, W.; Winsauer, K. *Anal. Chim. Acta* **1987**, *196*, 251-254.

235. Iriyama, K.; Iwamoto, T.; Yoshiura, M. *J. Liq. Chromatogr.* **1986**, *9*, 955-969.

236. Carro-Ciampi, G.; Hunt, P. G.; Turner, C. J.; Wells, P. G. *J. Pharmacol. Methods* **1988**, *19*, 75-83.

237. Megaw, J. M.; Lee, J.; Lerman, S. *Lens Res.* **1985**, *2*, 351-368.

238. Sacchetta, P.; DiCola, D.; Federici, G. *Anal. Biochem.* **1986**, *154*, 205-208.

239. Eyer, P.; Podhradsky, D. *Anal. Biochem.* **1986**, *153*, 57-66.

240. Beutler, E.; Srivastava, S. K.; West, C. *Biochem. Biophys. Res. Commun.* **1970**, *38*, 341-347.

241. *Handbook of Biological Data*; Spector, W. S., Ed. Saunders: Philadelphia, 1956.

242. Johnson, C. A.; Bergeim, O. *J. Biol. Chem.* **1951**, *188*, 833-838.

243. Levy, H. L.; Barkin, E. *J. Lab. Clin. Med.* **1971**, *78*, 517-523.

244. Liu, A.; Li, T.; Wang, E. *Anal. Sci.* **1995**, *11*, 597-603.

245. Jacobean, S. H.; Molds, P. *Clin.Nephrol.* **1994**, *42*, 189-192.

246. Shadle, S. E.; Hedman, B.; Hodgson, K. O.; Solomon, E. I. *J. Am. Chem. Soc.* **1995**, *117*, 2259-2272.

247. Waldo, G. S.; Carlson, R. M. K.; Modowan, J. M.; Peters, K. E.; Penner-Hahn, J. E. *Geochim. Acta* **1991**, *55*, 801-814.

248. Stern, E.; Heald, S. *Rev. Sci. Instr.* **1979**, *50*, 1579-1582.

249. Powers, L.; Blumberg, W. E.; Chance, B.; Barlow, C. H.; Leigh, J. S., Jr.; Smith, J.; Yonetani, T.; Vik, S.; Peisach, J. *Biochim. Biophys. Acta* **1979**, *546*, 520-538.

250. Piccoli, G.; Fiorani, M.; Biagiarelli, B.; Palma, F.; Potenza, L.; Amicucci, A.; Stocchi, V. *J. Chromatogr. A* **1994**, *676*, 239-246.

251. Malloy, M. H.; Rassin, D. K.; Gaull, G. E. *Anal. Biochem.* **1981**, *113*, 407-415.

252. Mills, B. J.; Richie, J. P., Jr.; Lang, C. A. *Anal. Biochem.* **1990**, *184*, 263-267.

253. Fahey, R. C. In *Glutathione. Chemical, Biochemical and Medical Aspects*; Dolphin, D.; Avramovic, O. and Poulson, R., Eds.; J. Wiley & Sons: New York, 1989; pp 304-337.

254. Pickering, I. J.; Prince, R. C.; Divers, T.; George, G. N. *FEBS Lett.* **1998**, *441*, 11-14.

255. Chen, C.; Cheniae, G. M. In *Photosynthesis: from Light to Biosphere*; Mathis, P., Ed. Kluwer Academic Publishers: Dordrecht, The Netherlands, 1995; Vol. II; pp 329-332.

256. Han, K.-C.; Katoh, S. In *Research in Photosynthesis*; Murata, N., Ed. Kluwer Academic Publishers: Netherlands, 1992; Vol. II; pp II.6.365-II.366.368.

257. Boussac, A.; Setif, P.; Rutherford, A. W. *Biochemistry* **1992**, *31*, 1224-1234.

258. Powers, L. *Biochim. Biophys. Acta* **1982**, *683*, 1-38.

259. Holt, C.; Hasnain, S. S.; Hukins, D. W. L. *Biochim. Biophys. Acta* **1982**, *719*, 299-303.

260. Bianconi, A.; Giovannelli, A.; Gastellani, L.; Alema, S.; Fasella, P.; Oesch, B.; Mobilio, S. *J. Mol. Biol.* **1983**, *165*, 125-138.

261. Grush, M. M. Ph.D. Thesis, University of California, Davis, 1996.

262. Dekker, J. P.; Boekema, E. J.; Witt, H. T.; Rögner, M. *Biochim. Biophys. Acta* **1988**, *936*, 307-318.

263. Philouze, C.; Blondin, G.; Girerd, J.-J.; Guilhem, J.; Pascard, C.; Lexa, D. *J. Am. Chem. Soc.* **1994**, *116*, 8557-8565.

Appendices

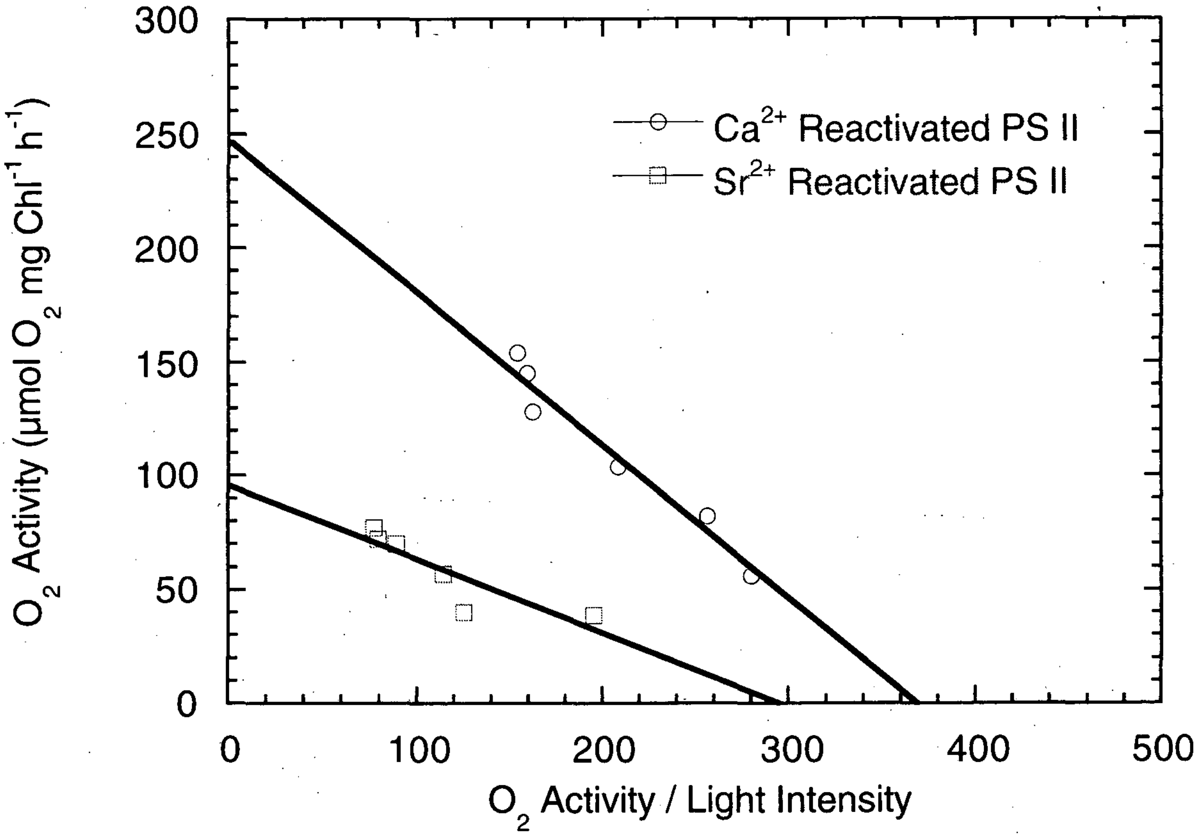

Appendix 1 Light intensity dependence of oxygen activity for Sr^{2+}- and Ca^{2+}-reactivated PS II. The metals reconstitution of Ca-depleted PS II were done as described in Chapter 2. Light levels were varied from 100% to 20% using neutral density filters (100, 91, 79, 50, 32, 20%). The best-fit lines are drawn through these six points. At saturating light intensity (extrapolated y-intercept), the activity with Sr is only 38% compared to that of Ca, but at limiting light levels (x-intercept), the percentage is higher (81%). Even though Sr^{2+} has replenished the PS II centers almost as effectively as Ca^{2+} (81%), the rate-limiting step in O_2 evolution is slower for Sr-reactivated membranes. This is evident in the lower (40%) activity at normal, saturating light conditions. The study was patterned after a previous experiment.[35]

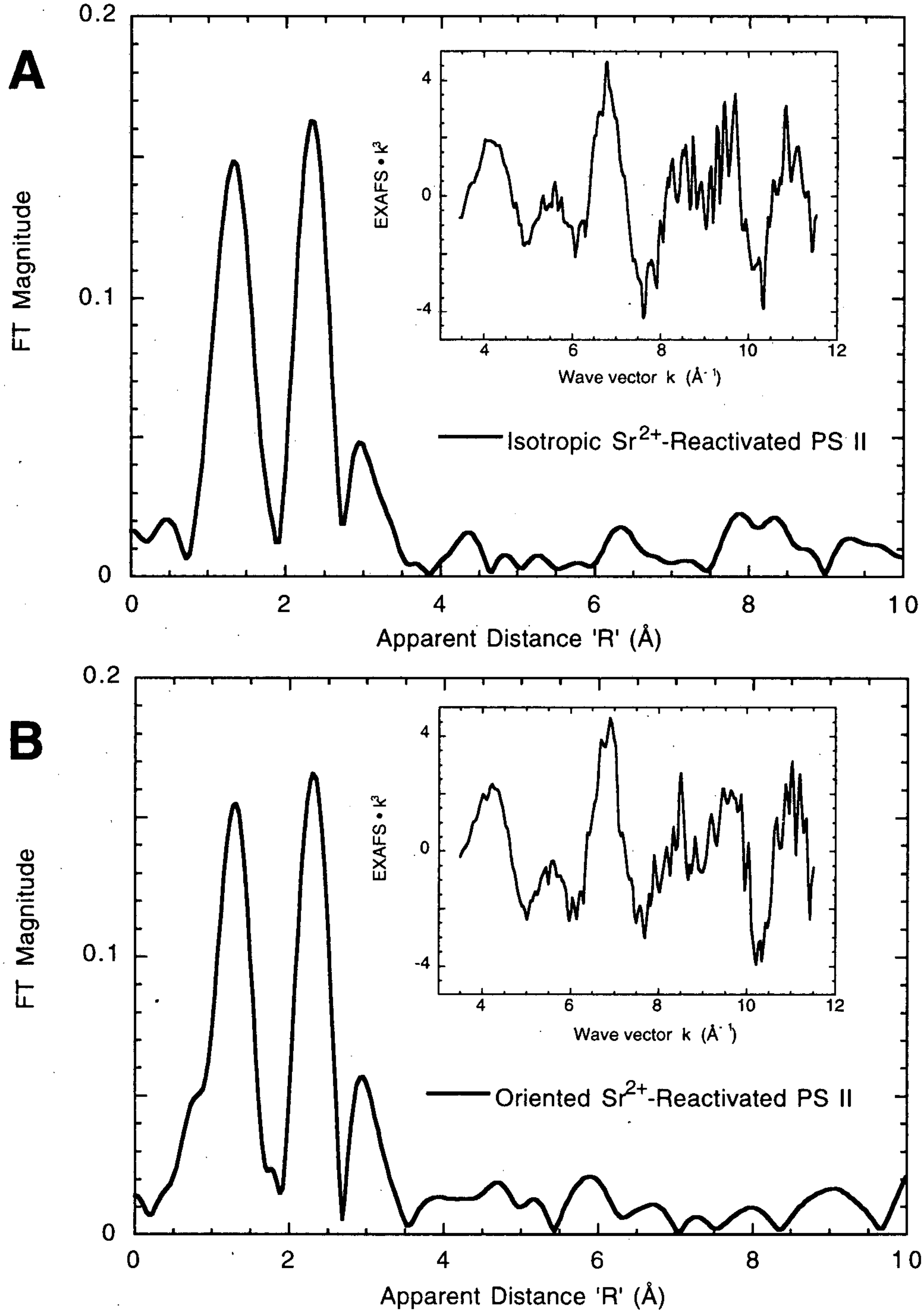
A
FT Magnitude
0.2
0.1
0
0
2
4
6
8
10
Apparent Distance 'R' (Å)
EXAFS • k³
4
0
-4
4
6
8
10
12
Wave vector k (Å⁻¹)
Isotropic Sr²⁺-Reactivated PS II
B
FT Magnitude
0.2
0.1
0
0
2
4
6
8
10
Apparent Distance 'R' (Å)
EXAFS • k³
4
0
-4
4
6
8
10
12
Wave vector k (Å⁻¹)
Oriented Sr²⁺-Reactivated PS II

Appendix 2 Mn EXAFS of Isotropic (**A**) and Oriented (**B**) Sr-reconstituted PS II. Sample preparation methods for the pelleted and layered Sr-PS II were described in Chapter 2 and 3, respectively. The oriented Sr-PS II sample was measured at the magic angle ($\theta \sim 55°$). Data collection and analysis were also mentioned previously. Peaks at 'R' < 1 Å are due to residual background. The inset shows the k^3-weighted Mn EXAFS (a five-domain spline was removed as background correction). These EXAFS spectra reflect the environment of the Mn cluster in the OEC at the dark-adapted S_1 state. Compared to other Mn EXAFS studies,[22,25,46] these spectra are normal and do not indicate significant damage to the Mn centers resulting from the various treatments. The two spectra are nearly indistinguishable and show that the Mn cluster is nearly identical for both types of Sr-reconstituted PS II.

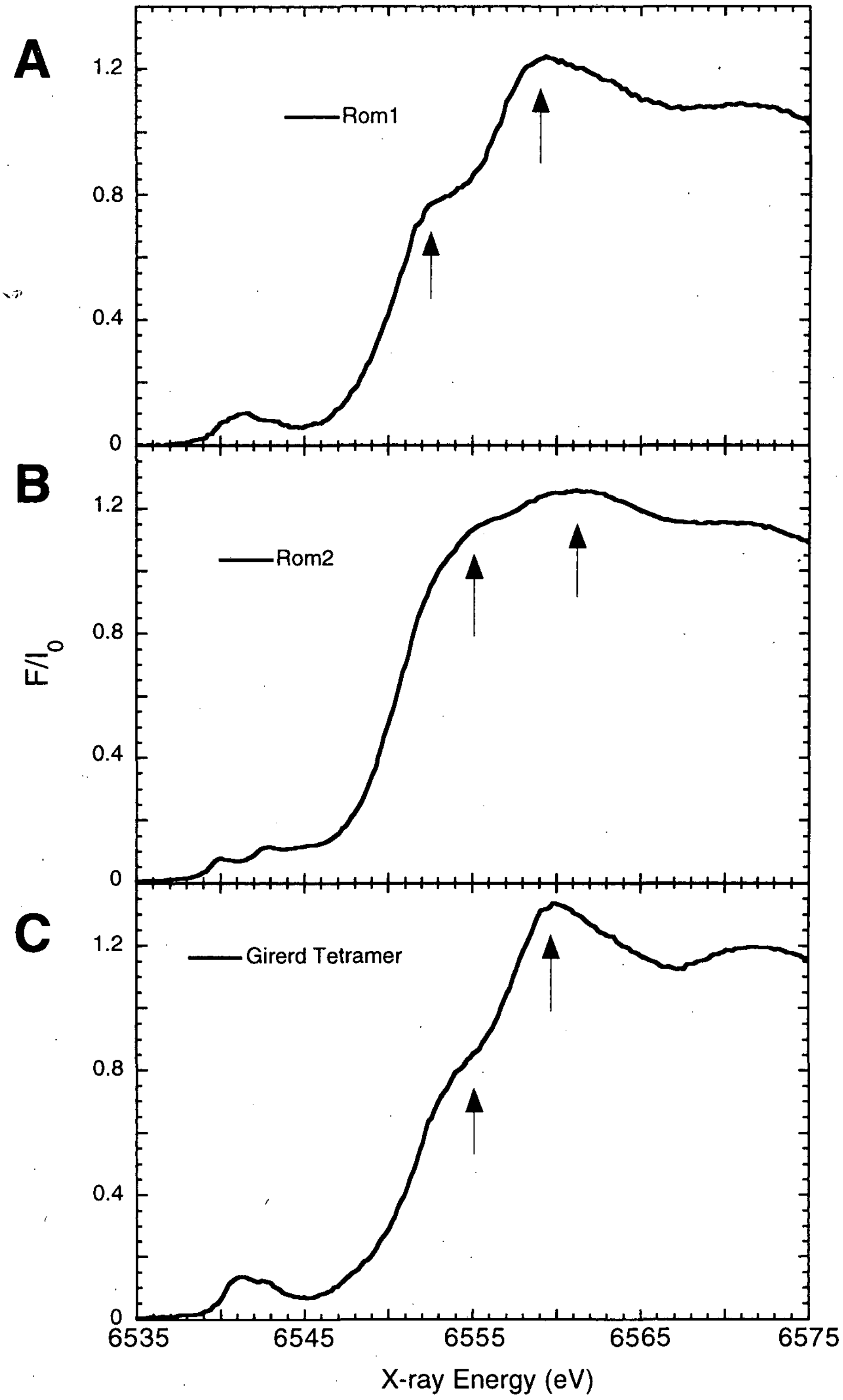
A
B
C
Rom1
Rom2
Girerd Tetramer
F/I$_0$
0
0.4
0.8
1.2
6535
6545
6555
6565
6575
X-ray Energy (eV)

Appendix 3 Normalized Mn K-edge XANES from three tetranuclear Mn model compounds with bipyridine (bpy) ligands.

(**A**) Rom1	$[Mn_4O_6(bpy)_6][Cr_2O_7]_2$
(**B**) Rom2	$[Mn_4O_5(OAc)_2(H_2O)_2(bpy)_4][Cr_2O_7]_2$
(**C**) Girerd Tetramer	$[Mn_4O_6(bpy)_6][ClO_4]_4(H_2O)$

The first two $[Mn^{III}_2Mn^{IV}_2]$ compounds were synthesized in the group of Dr. Roman Czernuszewicz (Dept. of Chemistry, Univ. of Houston, Texas), and the third $[Mn^{IV}_4O_6]$, called the "Girerd tetramer", came from Dr. Jean-Jacques Girerd (Laboratory of Inorganic Chemistry, Univ. of Paris-South, Orsay, France)[263] Samples were prepared and XANES data collected as described in Chapter 4, except that $SrCO_3$ was used as the diluent.

Although their respective topologies may be different, compared to the non-Cl Mn cubanes in Figure 4.3, there is clearly more structure in these example XANES spectra (indicated by the arrows). The O-ligated cubanes in Fig. 4.3 show mostly "round," featureless edges while shoulders and peaks are visible in the three pyridine-ligated compounds shown here. Although XANES theory is underdeveloped for transition metals like Mn, these K-edge features are thought to arise from the pyridine ligands (here, bipyridine), which have π^* (antibonding) orbitals that can mix with the Mn orbitals, and influence the $1s \rightarrow 4p$ transitions. As an example, after removal of two bpy ligands and replacement with two OAc, Rom2 begins to assume a more "rounded" appearance in the K-edge compared to (A) or (C), and more similar to the O-ligated cubanes of Fig. 4.3.

ERNEST ORLANDO LAWRENCE BERKELEY NATIONAL LABORATORY
ONE CYCLOTRON ROAD | BERKELEY, CALIFORNIA 94720

Prepared for the U.S. Department of Energy under Contract No. DE-AC03-76SF00098